X-RAY SCATTERING STUDIES OF STRONGLY CORRELATED MATERIALS: ORBITAL ORDERING IN $KCuF_3$ AND STRIPE-LIKE DOMAIN STRUCTURES IN $BiFeO_3$ EPITAXIAL THIN FILMS

BY

JAMES LEE

DISSERTATION

Submitted in partial fulfillment of the requirements
for the degree of Doctor of Philosophy in Physics
in the Graduate College of the
University of Illinois at Urbana-Champaign, 2013

Urbana, Illinois

Doctoral Committee:

Professor Lance Cooper, Chair
Associate Professor Peter Abbamonte, Director of Research
Professor Philip Phillips
Assistant Professor Liang Yang

Abstract

The results of x-ray scattering experiments on orbitally ordered $KCuF_3$ and periodic arrays of stripe-like ferroelectric domains in epitaxial thin films of multiferroic $BiFeO_3$ are presented in this dissertation. Both resonant soft x-ray elastic scattering and non-resonant hard x-ray elastic scattering probes were used.

Our experiments on $KCuF_3$ have revealed a previously unidentified structural phase transition at T = 50K, involving $GdFeO_3$ like rotations of the CuF_6 octahedra. These rotations are quasi-ordered and exhibit glassy hysteresis, but serve to stabilize the Néel state at T = 39K. Based on these observations, we have formulated an orbital ordering model based on the archetypical Kugel-Khomskii model. Our modified Kugel-Khomskii model takes into account direct orbital exchange interactions due to a combination of electron-electron interactions and charge transfer effects. The effect of this term is to create a near degeneracy that dynamically frustrates the spin order that is lifted at low temperature by subdominant orbital-lattice interactions. A strong optical effect seen in the Cu L_3 resonant scattering is also discussed.

We also describe on-going studies of $BiFeO_3$ epitaxial thin films. Based on non-resonant diffraction data, we have created simple charge density models that describe the structure of stripe-like ferroelectric domains with majority 109° and majority 71° domain walls. Resonant soft x-ray scattering near the Fe L_3 transition edge has revealed a spatial modulation of predominantly Fe 3d valence states with a period equal to that of the ferroelectric domain structure. The possibility of a magnetic origin to the Fe L_3 edge resonant scattering is discussed. No O K edge resonant scattering was observed, indicating that O 2p states are not significantly influenced by the domain structure. The absence of O K edge resonant scattering is also discussed in terms of proposed mechanisms for the anomalously high electrical conductivity of 109° domain walls. We also briefly describe the observation of scattering near the substrate peak due to the thin film domain structure, which is causing a modulation of the substrate strain.

This work is dedicated to the memory of the National Synchrotron Light Source

Acknowledgments

First, to my fellow graduate students and personal friends: Paul Matthew Sutter, Jeremy Tan, Tomasz Olewicz, Danielle Chandler, and Tristan Rocheleau. Thank you for helping me get through my first few years here.

I would like to convey my thanks to the scientists and staff of the many light sources I have visited over the years.

Outside of Urbana, my formative experiences as a scientist have been at the National Synchrotron Light Source, located at the Brookhaven National Laboratory, Upton, NY. Serban Smadici, as a postdoc and, later, research scientist at UIUC guided me through the harrowing ordeal of learning how to use my first beam line: X1B. Many technical crises were resolved with the help of Mike Caruso, Gary Nitzel, Shuwei Leng, and Zhijian Yin. Steve Hulbert, Christie Nelson, and Cecilia Sanchez-Henke provided neighborly help and professional advice. Finally, Chi-Chang Kao (now at SSRL) was a friendly face during my week-long runs, dropping by occasionally to see what I was up to.

My non-synchrotron work was carried out in large part in the Fredrick Seitz Materials Research Laboratory Central Facilities, University of Illinois. The Center for Microanalysis of Materials allowed me to gather valuable data on the structures of our thin film samples, especially $BiFeO_3$. Mauro Sardela provided valuable technical assistance and some tutoring on x-ray diffraction early in my grad school career.

Critical work on $KCuF_3$ was done at the Advanced Photon Source, at Argonne National Laboratory, Lemont, IL. I wish to thank Yejun Feng and Tim Graber, who were very helpful during our experiment at Sector 4; as well as the staff who helped us conduct a crystallography experiment at Sector 12. I would also like to acknowledge Jessica McChesney at Sector 29, who was a friendly collaborator at X1B.

I also gained a lot of valuable research experience at CHESS. My gratitude goes to Ken Finkelstein at C-Line, for being very friendly and patient, and for sharing a portion of extensive knowledge of x-ray science with me. Bob Seeley also saved our bacon during runs at CHESS, helping us get the various closed cycle cryostats we used there up and running.

Some preliminary work was also done at the Advanced Light Source, at Lawrence Berkeley National Laboratory, Berkeley, CA. Yi-De Chuang was very helpful during our time there.

While on beam runs, many members of my group assisted in taking data

and helped to set up equipment. The contributions of Young-Il Joe, Yu Gan, Xiaoqian Chen, Anshul Kogar, Shuai Wang, Jeremy Morales, and James Reed are acknowledged here.

Thank you, Peter, for your steady mentorship and good humor. It's been an honor to have learned how to practice science from you.

Finally, my love and deepest gratitude goes to Brenna, whose long wait to have me back from the thesis is over.

My research at Urbana was funded by the US Department of Energy, Office of Basic Energy Sciences, under grant numbers DE-FG-06-ER 46285 and DE-FG-07-ER 46453. Use of the National Synchrotron Light Source, Brookhaven National Laboratory, was supported by the U.S. Department of Energy, Office of Science, Office of Basic Energy Sciences, under Contract No. DE-AC02-98CH10886. Use of the Advanced Photon Source, an Office of Science User Facility operated for the U.S. Department of Energy (DOE) Office of Science by Argonne National Laboratory, was supported by the U.S. DOE under Contract No. DE-AC02-06CH11357. This work is based upon research conducted at the Cornell High Energy Synchrotron Source (CHESS) which is supported by the National Science Foundation and the National Institutes of Health/National Institute of General Medical Sciences under NSF award DMR-0936384. The Advanced Light Source is supported by the Director, Office of Science, Office of Basic Energy Sciences, of the U.S. Department of Energy under Contract No. DE-AC02-05CH11231.

Table of Contents

1 Introduction

1.1 The Challenge of Strongly Correlated Materials

The universe is composed of matter and energy. Long before the concepts of matter and energy even existed in anybody's mind, people have sought to use matter and energy for their own ends, to meet the practical needs of life or to satisfy an innate curiosity. Knowledge about the nature of matter and energy, accumulated by many generations, now allows our society to create materials that have never before existed, with novel properties that are not only technologically relevant but also touch upon profound issues regarding the quantum mechanical nature of matter and energy.

There are many examples of such exotic materials. Colossal magnetoresistance (CMR) materials, such as manganese oxide perovskites, exhibit decreases in electrical resistance, by factors on order of $10^2 - 10^3$, when exposed to external magnetic fields. The magnetoresistive properties of many such manganites depend, in part, on the pattern in which the Mn 3d orbital states are occupied in the crystal, a phenomenon called orbital ordering. [1] The mechanisms of orbital ordering are not yet well understood, and are active topics of study. There are also multiferroic systems, so-called because the ferroelectric, ferromagnetic, and structural order parameters are coupled to each other. One prominent example is $BiFeO_3$ which, unlike many other ferroelectrics, exhibits very large electric polarizations at temperatures well above room temperature. It is not known why $BiFeO_3$ exhibits such robust ferroelectricity or how it is coupled to its magnetic and structural properties. [2]

What determines the properties of such materials? Being transition metal oxides, they are all similar in that they possess similar structure and chemistry. Yet, minor variations in these can cause the members of this material class to display a wide array of disparate and unexplained phenomena. The electrons in these systems also exhibit strong correlations with each other, so their dynamics cannot be treated using non-interacting electron models, which have worked so well in predicting the electrical and thermal properties of elemental metals. [3]

To understand the origin of such phenomena, we can study the electronic structure of these strongly correlated electron materials.

Long established theoretical tools, such as band theory and density func-

tional theory, that have done so well in describing the properties of simple metals and some semiconductors and insulators are not well suited to tackling strong correlation effects. The microscopics are calculated in these approaches using a model in which an electron interacts with a mean field created by surrounding electrons and ions, rather than taking into account the detailed positions of surrounding electrons. In strongly correlated electron materials, however, interactions with surrounding electrons cannot be averaged over. For example, in so-called Mott insulators, electron localization effects cause systems with half-filled energy bands to become insulators. The naive expectation is that such systems should be metallic: however, strong mutual repulsions with electrons on neighboring sites make it energetically unfavorable for electrons to delocalize from their atomic sites, thereby inhibiting electron transport. The exact details of the electron states on each atomic site matter, which makes solving the electronic structure problem extremely difficult. New theoretical tools have to be developed to treat strongly correlated electron systems. [4]

In order to identify the new and essential physical concepts, many researchers have resorted to using highly simplified Hamiltonians, like the Hubbard model, to describe the critical correlations between just the lowest energy electron states rather than every electron on every atom. Despite being highly idealized, the properties of such models resemble the behavior of real materials. A modified Hubbard model was used by Kugel and Khomskii [5], for example, to formulate a now widely used model for orbital order. The essential physics of this model will be discussed in some depth later in this dissertation. A weakness of such model Hamiltonians is that they are not first-principles calculations. Instead, they rely on the values of effective parameters fed into them. Some of these parameters can be determined using experimental probes of electronic structure.

The experimental determination of the electronic structure of two strongly correlated transition metal oxide systems will be the topics of this dissertation. We will first discuss $KCuF_3$, which is often referred to as the prototype of orbital ordering physics. The magnetism of this system is very sensitive to the orbital states occupied by its valence electrons, much like the magnetism of $LaMnO_3$, the prototype compound of the CMR manganites. While pre-existing models, like the popular Kugel-Khomskii model, work well to predict the symmetry of the magnetism due to orbital order, they cannot give correct quantitative descriptions of some important features of systems like $KCuF_3$. We will address what physics might be missing from such orbital ordering models. The second system we will study is $BiFeO_3$. In thin film form, this system can manifest electrically conductive domain walls, even though the bulk system is insulating. Futher, only certain species of domain wall are conducting while others are insulating. [53] We seek to understand why this is the case and what role the ferroic order parameters might play in this behavior.

The electronic structure of these systems have been studied using x-ray scattering and absorption techniques. These methods will be described in the next

chapter.

1.2 Common Physical Features of $KCuF_3$ and $BiFeO_3$

To facilitate later discussion, we will first examine some of the features shared by $KCuF_3$ and $BiFeO_3$.

The structures of $KCuF_3$ and $BiFeO_3$ are distorted versions of the ideal cubic perovskite structure, the ABX_3 aristotype. The ideal perovskite structure is illustrated in Figure 1.1, taking $SrTiO_3$ as an example. This structure is made of A cations, which are usually ions with large ionic radii like K or Bi, that reside on the center of the cubic unit cell; B cations that are often transition metals like Cu or Fe, located at the corners of the cell; and X anions, like O or F, that are at edge-centered positions and are octahedrally coordinated around the B site. [6]

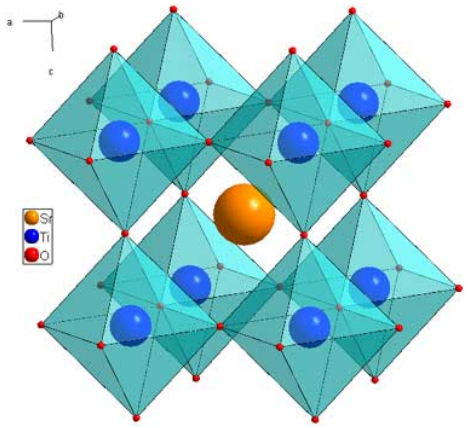

Figure 1.1: A cubic unit cell of $SrTiO_3$, which is also an example of the ABX_3 aristotype. The A cation (Sr) is located at the body center site of the cell; the B cation (Ti) on the corners of the cell; and the X anions (O) are octahedrally coordinated around the B sites. This image was retrieved from http://www.princeton.edu/ cavalab/tutorials/public/structures/perovskites.html

Most structures never realize the aristotype: B-X lengths can become unequal, distorting the BX_6 octahedral complex and reducing its symmetry, which happens in $KCuF_3$. Shifts of ionic sublattices away from ideal crystallographic positions can also occur: in $BiFeO_3$, the B and X sublattices shift with respect to the A sublattice. This is how the ferroelectric moment forms $BiFeO_3$. The octahedral complexes not only distort but they can also rotate and tilt, as illustrated in Figure 1.2 for the case of $GdFeO_3$. A heuristic reason for this octahedral tilting is that the ions (hard spheres in this picture) of the unit cell are too loosely or tightly packed, which either leaves the octahedra free to shift in the unit cell or forces the octahedra to buckle and rotate to compensate for

the lack of space. Based on ionic radii, it is possible to predict whether a structure will have tilted octahedra based on the value of the Goldschmidt tolerance factor: $t = (R_A + R_X)/(R_B + R_X)/\sqrt{2}$, which is less than unity for overpacked cells, greater than one for loosely backed cells, and unity for an ideally packed situation. For most cubic perovskite systems, $0.78 < t < 1.05$, so most such systems exhibit octahedral tilts. Using Shannon's tables of effective ionic radii, [8] it can be shown that in $KCuF_3$ $t = 0.975$ and for $BiFeO_3$ $t = 0.889$; by this measure, the structures of $KCuF_3$ and $BiFeO_3$ should be distorted. [7]

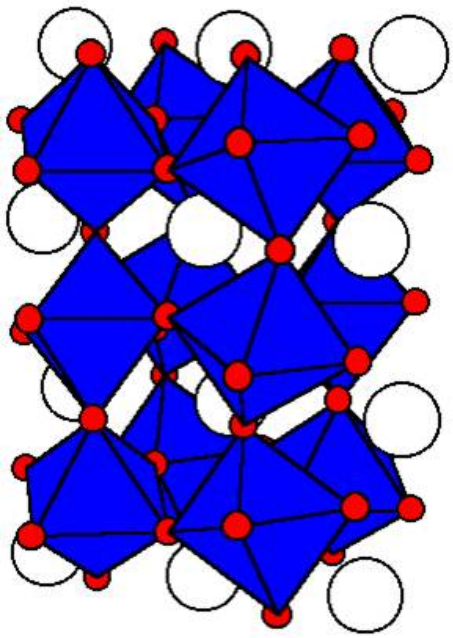

Figure 1.2: A type of distortion commonly found in perovskite systems are rotations and tilts of the transition metal-anion octahedral complexes, as illustrated in this figure. This image was retrieved from https://web.chemistry.ohio-state.edu/ woodward/ch754/struct/GdFeO3.html

Of course, the ions are not hard spheres but atoms that chemically bond with their neighbors. The underlying origin for the octahedral tilts, therefore, is that the electron orbital states of the A cations sometimes hybridize with those of the X anions, and bond lengths change to lower the global energy of the system. [7]

This brings us to the idea that the crystal structure, especially the symmetry of the octahedral complex, can strongly influence the electronic structure. The influence the structure has on the electronic states of transition metal B site ions, which are most relevant to us, can be qualitatively understood using the "crystal field" idea. [9] Conceptually, the X site ligand anions create a Coulomb potential that destroys the spherical symmetry of the environment of the transition metal ion. If the ligands are octahedral coordinated around the metal ion, the five-fold degeneracy of the d-orbital states splits into two-fold dengerate e_g and three-

fold degenerate t_{2g} orbital manifolds. The e_g manifold comprises $d_{3z^2-r^2}$ and $d_{x^2-y^2}$ orbitals, while the t_{2g} manifold comprises $d_{3z^2-r^2}$ and $d_{x^2-y^2}$ orbitals, as shown in Figure 1.3. The e_g states are of higher energy than the t_{2g} states. This can be understood by considering that the charge densities of the e_g states are oriented toward the ligands and the t_{2g} states are directed away from the ligands and toward the edges of the octahedron.

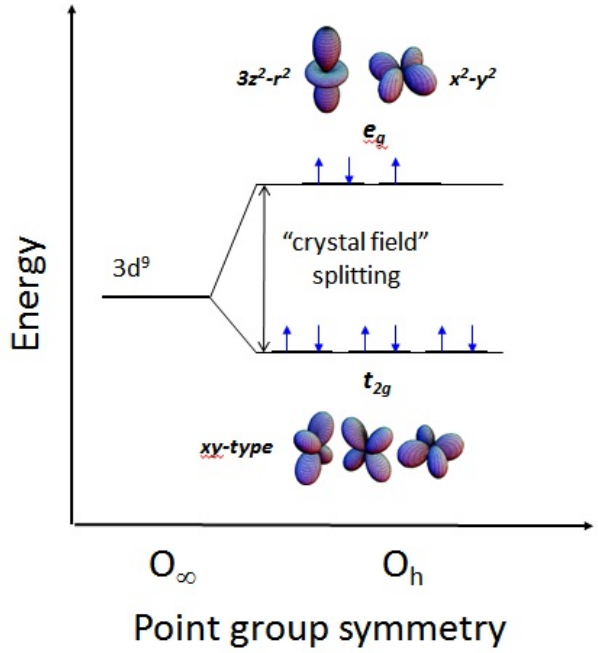

Figure 1.3: The degeneracy of the $3d^9$ electron orbital states of a Cu^{2+} ion is lifted when the symmetry of the surrounding environment is lowered from spherical symmetry to that of the octahedral point group O_h. As illustrated, "xy-type" 3d orbitals form the three dimensional t_{2g} orbital manifold and the $3z^2$-r^2 and x^2-y^2 orbitals form the two dimensional e_g orbital manifold. The energy difference between the e_g and t_{2g} energy levels is determined in part by the ions surrounding the Cu^{2+} ion, conceptually illustrated by the "crystal field".

For distorted structures, the symmetry of the metal ion environment is further lowered and the degeneracy of the orbital manifolds can be further lifted.

Since this situation is repeated throughout the entire crystal, the electron band states of the crystal will retain the flavor of the crystal field states.

The orbital character of the crystal field states, as well as the octahedral distortions mentioned earlier, have a profound influence on the magnetic properties of transition metal perovskite systems.

The most important effect to consider is the so-called superexchange coupling between unpaired electron spins on nearest neighbor transition metal sites. According to the semi-empirical Goodenough-Kanamori rules that describe superexchange, [10] the effective spin exchange between such electron spins is

antiferromagnetic if the electrons occupy orbitals with lobes that are directed toward each other and have a large overlap. If the two occupied orbitals do not overlap, or the overlap is zero by symmetry, the effective spin exchange is ferromagnetic but quite small in magnitude.

The reason why superexchange favors antiferromagnetic spin exchange lies in the hybridization of the metal and ligand wave functions. The hybridized states form exchange pathways for the electrons of neighboring metal ion sites, permitting them to delocalize and interact. Delocalization is energeticaly favorable if the unpaired electrons on the metal sites are antiferromagnetically aligned, since two spin up or spin down electrons cannot occupy the same state by the Pauli exclusion principle.

In Anderson's perturbation theory analysis, [11] superexchange arises as a second order effect, and the energy difference between ferromagnetic and antiferromagnetic spin states is $J = -2t^2/U$, where t is an orbital-state dependent transfer integral that parameterizes the delocalizing kinetic energy of the electron, and U is the repulsion between two electrons occupying the same metal site. The orbital overlaps control the magnitude of t: for small or zero overlap, the superexchange effect vanishes and the direct exchange process favors ferromagnetism. When the overlap is substantial, however, the magnitude of J is larger than the direct exchange contribution and always favors antiferromagnetism.

The superexchange effect explains why most insulating transition metal perovskites exhibit antiferromagnetic spin order, as $BiFeO_3$ and $KCuF_3$ do.

Often, the antiferromagnetic spin order is canted and the systems are weakly ferromagnetic as a result. To understand this, we finally consider the Dzyaloshinsky-Moriya effect, [12] which is an additional anti-symmetric exchange coupling between electron spins on neighboring metal ion sites. This is illustrated in Figure 1.4. This interaction gives a contribution to the total energy of the form $\Delta E = \vec{D} \cdot (\vec{S}_1 \times \vec{S}_2)$, which forces the net ferromagnetic moment from the spin canting to be perpendicular to the couping vector $\vec{D}$. This coupling vector is due to spin-orbit coupling and can only be non-zero in a low-symmetry environment, in which the ligand ion (e.g. the O or F ions in $BiFeO_3$ and $KCuF_3$) is displaced from its ideal crystallographic position: $\vec{D}$ vanishes if a local inversion center exists between the spin sites. The spin canting from the Dzyaloshinsky-Moriya interaction will be an important effect in both $BiFeO_3$ and $KCuF_3$.

With this background, we are now ready to address the physics of $KCuF_3$ and $BiFeO_3$.

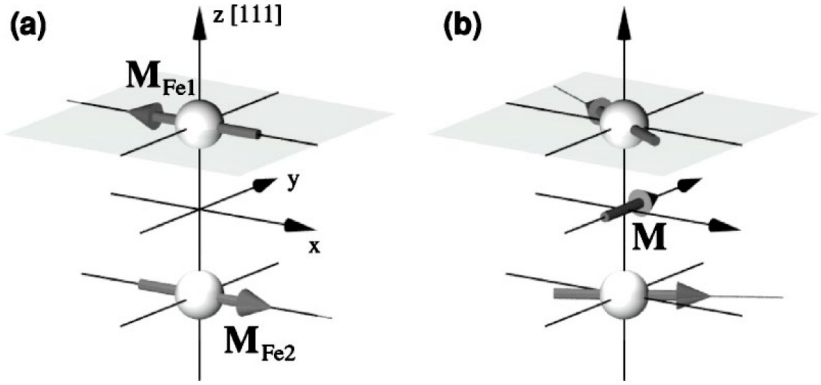

Figure 1.4: (a) The electron spins on two nearest neighbor Fe ions, Fe1 and Fe2, are antiferromagnetically aligned. (b) Spin canting due to the Dzyaloshinsky-Moriya effect causes the spins on the Fe sites located along the [111] axis to cant away from the ideal antiferromagnetic order. The lattice symmetry restricts the canting to the (111) plane and a net ferromagnetic moment **M** is formed perpendicular to [111]. Taken from Reference [56].

2 Methods: X-ray Scattering and Absorption

This chapter is devoted to the theory and techniques of elastic x-ray scattering and x-ray absorption by materials, particularly when the wavelength of light can be considered to be in the "soft x-ray" range. This range is customarily taken to be 250 eV to several keV, the range of energies in which atomic dipole transitions can occur in low and intermediate Z atoms. [13]

2.1 Theory

The classical basis of x-ray scattering is presented first, with emphasis placed on how the scattering relates to the susceptibility tensor. The susceptibility tensor is a quantum mechanical entity, so the microscopic basis of scattering is considered next and an expression for the susceptiblity is derived. The origin of resonant elastic x-ray scattering is also discussed. Finally, x-ray absorption processes are considered and the relationship between experimentally obtained absorption spectra and the susceptibility tensor is explained.

2.1.1 X-ray Scattering

We begin by studying the classical basis of x-ray scattering. The Maxwell equations serve as a starting point, which will be used to describe the propagation of electromagnetic fields in matter. This is a valid approach if nearly all the scattering is coherent, which is to say that there is no difference in frequency between the incident and scattered light. This can be safely assumed since, in the soft x-ray range, elastic scattering cross-sections of electrons in elements such as copper are many orders of magnitude greater than the inelastic scattering cross-sections. [14]

The scattering is dependent in microscopic properties of the system, which do not enter into the Maxwell equations except through the macroscopic quantities $\vec{P}$, the electric polarization, and $\vec{M}$, the magnetization. To truly understand these quantities, one must consider the microscopic physics of the material; however, by using x-ray scattering to characterize $\vec{P}$ and $\vec{M}$, constraints can be placed on subsequent microscopic calculations.

Considering the case in which there are no free currents and no free charges, and using the usual constitutive equations, [15] [16] the following wave equation

for the electric displacement field can be formulated:

$$(\nabla^2 + \omega^2\epsilon_0\mu_0)\vec{D} = -\nabla \times \nabla \times \vec{P} - i\omega\epsilon_0\mu_0\nabla \times \vec{M},$$

where ϵ_0 and μ_0 are, respectively, the permittivity and permeability of free space. In deriving the wave equation, it was assumed that the fields are harmonic.

$\vec{P}$ and $\vec{M}$ describe the response of the material to external fields. If the incident beam is not too intense, the response can be treated as linear:

$$\vec{P} = \overleftrightarrow{\chi}_e \cdot \vec{D}_0;$$

and

$$\vec{M} = \overleftrightarrow{\chi}_m \cdot \vec{H}_0 = \overleftrightarrow{\chi}_m \cdot (\hat{k}_0 \times \vec{D}_0)\frac{1}{\sqrt{\epsilon_0\mu_0}}.$$

In these expressions, $\vec{D}_0$ is the incident field, $\hat{k}_0$ is the direction of the incident wave vector, and it is assumed that the incident field is nearly monochromatic. $\overleftrightarrow{\chi}_e$ and $\overleftrightarrow{\chi}_m$ are spatially inhomogeneous, i.e. functions of position, which is the reason there is scattering to begin with. It should also be noted that the dependence on $\vec{D}_0$ amounts to the use of the first order Born approximation. [15]

The wave equation resembles the Helmholtz equation, so the solution for $\vec{D}$ readily presents itself as

$$\vec{D} = \vec{D}_0 + \frac{1}{4\pi}\int \frac{e^{-k|\vec{r}-\vec{r'}|}}{|\vec{r}-\vec{r'}|}(\nabla' \times \nabla' \times \overleftrightarrow{\chi}_e \cdot \vec{D}_0 + i\omega\epsilon_0\mu_0\nabla' \times \overleftrightarrow{\chi}_m \cdot (\hat{k}_0 \times \vec{D}_0))d\vec{r'}.$$

In the far field limit, the above expression can be integrated by parts to find the portion of the scattered field at the detector with polarization $\hat{\epsilon}$:

$$\hat{\epsilon}^* \cdot \vec{D}_{sc} = D_0\frac{k^2}{4\pi}\frac{e^{-kr}}{r}\int e^{i\vec{q}\cdot\vec{r'}}(\hat{\epsilon}^* \cdot \overleftrightarrow{\chi}_e \cdot \hat{\epsilon}_0 + (\hat{k'} \times \hat{\epsilon}^*) \cdot \overleftrightarrow{\chi}_m \cdot (\hat{k}_0 \times \hat{\epsilon}_0))d\vec{r'},$$

where $\vec{q} = \vec{k}_0 - \vec{k'}$ is the momentum transfer; and $\hat{\epsilon}_0$ and $\hat{\epsilon}$ are the incident and scattered polarization vectors. The first term in the far field solution is attributed to "charge scattering" and the second term with "magnetic scattering".

While such a formal separation can be made and the scattering can be expressed as a function of two separate tensors, a single effective susceptibility tensor that accounts for the effects of both the polarization and magnetization can be created. [17] The far field scattering solution then looks like

$$\hat{\epsilon}^* \cdot \vec{D}_{sc} = D_0\frac{k^2}{4\pi}\frac{e^{-kr}}{r}\int e^{i\vec{q}\cdot\vec{r'}}\hat{\epsilon}^* \cdot \overleftrightarrow{\chi}_{sc} \cdot \hat{\epsilon}_0 d\vec{r'},$$

from which it is possible to isolate the classical scattering amplitude:

$$A_{sc,cl}(\vec{k},\hat{\epsilon}_0;\vec{k'},\hat{\epsilon}) = \frac{k^2}{4\pi}\int e^{i\vec{q}\cdot\vec{r'}}\hat{\epsilon}^* \cdot \overleftrightarrow{\chi}_{sc} \cdot \hat{\epsilon}_0 d\vec{r'} \tag{2.1}$$

The scattering of light from a material is, then, dependent on the properties of the generalized susceptibility, as well as the polarization of the incident x-rays.

Note that the effective susceptibility can be decomposed into a scalar component, traceless symmetric component, and an anti-symmetric component, as any second rank tensor can. The scalar and symmetric contributions express properties that are even under a time reversal operation; we can thus properly attribute scattering arising from these tensor terms to charge scattering. The anti-symmetric contribution expresses properties that are odd under time-reversal and can thus be said to describe magnetic scattering processes.

Since the susceptibility describes the properties of a crystal system, the tensor possesses its periodicities. [18] Therefore, the susceptibility tensor can be decomposed into a Fourier series

$$\overleftrightarrow{\chi}_{sc}(\vec{r}) = \sum_{\{H\}} \overleftrightarrow{\chi}_{sc,H} e^{-i\vec{k}_H\cdot\vec{r}}$$

where $\{H\}$ is the set of all reciprocal lattice vectors, as expressed in Miller indices H; $\vec{k}_H$ is the reciprocal space vector associated with H. If the Fourier sum is substituted for χ_{sc} in the integral of Equation 2.1,

$$\int e^{i\vec{q}\cdot\vec{r'}}\hat{\epsilon}^* \cdot \overleftrightarrow{\chi}_{sc} \cdot \hat{\epsilon}_0 d\vec{r'} = \sum_{\{H\}} \hat{\epsilon}^* \cdot \overleftrightarrow{\chi}_{sc,H} \cdot \hat{\epsilon_0} \int e^{i(\vec{q}-\vec{k}_H)\cdot\vec{r}'} d\vec{r}',$$

one finds that the integral on the right hand side of the equation is a delta function; therefore, reflections occur only when $\vec{q} \approx \vec{k}_H$, i.e. the Bragg condition. The scattering amplitude is determined by $\hat{\epsilon}^* \cdot \overleftrightarrow{\chi}_{sc,H} \cdot \hat{\epsilon_0}$, so the resulting scattering intensity will depend on the specific properties of the H Fourier component of the susceptibility. Which Fourier components will be non-zero depends on the properties of the atoms in the unit cell and their arrangement in the unit cell. This information is contained in the structure factor:

$$\hat{\epsilon}_b^* \cdot \overleftrightarrow{\chi}_{sc,H} \cdot \hat{\epsilon}_a = -\frac{r_0\lambda^2}{\pi V_{cell}} \sum_i^{<cell>} f_i^{ab}(\vec{q}_H,\omega) e^{i\vec{q}_H\cdot\vec{r}_i}, \tag{2.2}$$

where, r_0 is the classical electron radius; λ is the wavelength of light; and $f_i^{ab}(\vec{q}_H,\omega)$ is the atomic scattering amplitude of the i^{th} atom in the unit cell. [18] Since the atoms are not necessarily spherically symmetric, the atomic scattering amplitudes are tensor quantities [3]. The ab superscripts in f_i^{ab} denote the incident and scattered polarization states, on which the atomic scattering amplitude is dependent.

Equations 2.1 and 2.2 explictly show how the susceptibility and the scatter-

ing amplitude depends on the electronic properties of the atoms through the atomic scattering amplitudes. These contain information about the electronic structure of the atoms and their interactions with neighboring ions.

In the soft x-ray range, the maximum magnitude of the momentum transfer q is much smaller than the q that characterizes the structure of atomic electrons. Therefore, we can use the forward scattering values of the atomic scattering amplitudes: $f_i^{ab}(\vec{q}_{\{H\}},\omega) \approx f_i^{ab}(0,\omega)$. This simplification will prove important once we consider x-ray absorption.

It is now time to address the scattering process from a quantum mechanical perspective. Relating classical quantities to quantum quantities is made easier by the fact that the classical elastic scattering results are analogous to the quantum mechanical results for coherent scattering. [18]

A natural place to begin this discussion is with the Hamiltonian of the system. In the non-relativistic limit, $H = \sum_i \frac{(\vec{p}_i + e\vec{A}(\vec{x}_i))^2}{2m} + H_{nuc} + H_{rad}$, where m is the rest mass of the electron, $\vec{A}$ is the magnetic vector potential of the radiation field and e is the magnitude of the electron charge. The sum in the first term runs over all electrons bound to the atom. H_{nuc} accounts for the interaction of the electrons with the nuclear potential of the atom; and the final term accounts for the energy stored in the radiation field. Expanding the first term, and working in the Coulomb gauge, $H_{int,i} = \frac{e}{m}\vec{A}(\vec{x}_i)\cdot\vec{p}_i + \frac{e^2}{2m}\vec{A}(\vec{x}_i)^2$, and these terms are treated as perturbations to the atomic system. [19]

To proceed, the form of the magnetic vector potential must be known. By classical correspondence with the Fourier decomposition of $\vec{A}$, the magnetic vector potential in the Hamiltonian takes the following form: [20]

$$\vec{A} = \sum_u \sum_{\vec{k}} \hat{\epsilon}_u \sqrt{\frac{\hbar}{2\epsilon_0 V \omega_{\vec{k}}}} (a_{u,\vec{k}} e^{i(\vec{k}\cdot\vec{r}-\omega t)} + a^{\dagger}_{u,\vec{k}} e^{-i(\vec{k}\cdot\vec{r}-\omega t)}),$$

in which $a_{u,\vec{k}}$ is the photon annihilation operator, for the state with polarization u and wavevector $\vec{k}$; and V is the box normalization volume.

Using Fermi's Golden Rule, [21] including terms up to second order in the magnetic vector potential and using the dipole approximation ($e^{i\vec{k}\cdot\vec{r}} \approx 1$), the scattering amplitude for elastic scattering is

$$A_{sc,q}(\vec{k},\hat{\epsilon}_0;\vec{k}',\hat{\epsilon}) = \\ -r_0 \sum_i^{<cell>} \sum_{a_i} (\hat{\epsilon}^*\cdot\hat{\epsilon}_0 \langle a_i|e^{i\vec{q}\cdot\vec{r}_i}|a_i\rangle - \sum_I \frac{1}{m} \frac{\langle a_i|\hat{\epsilon}^*\cdot\vec{p}_i|I\rangle\langle I|\hat{\epsilon}_0\cdot\vec{p}_i|a_i\rangle}{E_I - E_{a_i} - \hbar\omega - i\gamma_I}). \quad (2.3)$$

In Equation 2.3, the labels a_i are the ground states of all the electrons of the i^{th} atom in the unit cell; $|I\rangle$ are the intermediate states over which the second order perturbation terms are summed; E_{a_i} and E_I are energies of the electron ground states and intermediate states; and γ_I is the inverse lifetime of the intermediate state, typically hundreds of meV. The first term describes Thomson scattering

while the second term describes the resonant scattering of x-rays and is a tensor quantity dependent on the incident and scattered polarization states.

Comparing the the classical and quantum scattering amplitudes we can, with some easy algebraic manipulation, find an explicit relation between the atomic scattering amplitudes of Equation 2.1 and the Thomson and resonant scattering terms in Equation 2.3:

$$\frac{1}{V_{cell}} f_i^{ab}(\omega) e^{i\vec{q}_H \cdot \vec{r}_i} = \sum_{a_i} (\hat{\epsilon}^* \cdot \hat{\epsilon}_0 \langle a_i | e^{i\vec{q}\cdot\vec{r}_i} | a_i \rangle - \sum_I \frac{1}{m} \frac{\langle a_i | \hat{\epsilon}^* \cdot \vec{p}_i | I \rangle \langle I | \hat{\epsilon}_0 \cdot \vec{p}_i | a_i \rangle}{E_I - E_{a_i} - \hbar\omega - i\gamma_I}). \quad (2.4)$$

Comparing the two sides of the equation, it becomes clear why the atomic scattering amplitude is often written in the form: $f_i^{ab}(\omega) = Z + f_{1,i}^{ab}(\omega) - i f_{2,i}^{ab}(\omega)$, where Z is the atomic number; $f_{1,i}^{ab}$, which is the real part of the resonant term; and $f_{2,i}^{ab}$, which is the imaginary part. [20]

Let us consider the physics associated with the above expressions. First, the resonant scattering term in Equation 2.3 is a product of two transition matrix elements that depend linearly on $\vec{A}$ and $\vec{p}$. This combination of matrix elements is required to describe an elastic scattering process, since pairs of photon creation and destruction operators are needed to return the system to its initial state.

Unlike Thomson scattering, the resonant scattering is a purely quantum mechanical effect. The states in the sum over a_i that are most important to the resonant scattering process are the inner-shell (core) states of the atoms, e.g. 1s or 2p states. When the incident x-ray beam energy $\hbar\omega$ is tuned to the core electron binding energies, $E_I - E_{a_i}$, virtual transitions of electrons from the core level to unoccpied states in the valence band (the intermediate states I) can be excited. Due to the limited lifetime of such an excited state, after $\tau \sim 1/\gamma_I$, an electron from the valence band state drops into the vacant core state. The x-ray emitted by the de-exciting electron is detected and the momentum transfer associated with this process can be observed. In this way, the energy-dependence and momenta of the unoccupied valence states can be mapped.

When this resonant dipole-dipole transition process is excited, the resonant term greatly increases in amplitude and, in principle, the resonant scattering can be on the same order of magnitude as the Thomson scattering. [22] Such massive enhancements in the cross-sections of the valence states is what makes this method feasible.

The matrix elements of the resonant scattering process linearly depend on the momentum operator, which is odd under parity. Therefore, the resonant scattering process described here can only occur between states with orbital momentum numbers that differ by $\Delta l = \pm 1$. [20]

Such data can reveal a great deal about the electronic states of the system. Mapping the momenta of the valence states can help determine which electron

states are participating in the ordered states of the system, such as antiferromagnetic spin ordering or charge density waves. This can be done by comparing the momenta at which resonant scattering occurs and comparing them to periodicities associated with the ordered states. The energy dependence of the resonant scattering can also be used to discern which electronic states of the various ions in the compound are interacting to create the ordered state or how those electronic states are altered by a symmetry lowering process in the material (e.g. structural phase transition).

Finally, like the classical susceptibility, the resonant scattering term can be decomposed into scalar, traceless symmetric, and anti-symmetric terms that possess the same properties under time reversal as the analogous components of the classical susceptibility. [21] Thus, resonant scattering can have its origins from both charge and magnetic processes.

2.1.2 X-ray Absorption

An important complementary probe of the electronic structure is x-ray absorption spectroscopy (XAS) and the reason why was briefly touched upon in the last section: the forward scattering values of the atomic scattering amplitudes can be used to describe the susceptibility tensor. XAS is directly related to the forward scattering amplitudes.

Let us briefly examine the underlying physics of XAS to understand why this is the case. The absorption process is related to the resonant scattering in that is mediated by the $\vec{A} \cdot \vec{p}$ term. However, only the term in the magnetic vector potential with a photon destruction operator plays any part. The interaction Hamiltonian is, then: $H_{int} = \frac{e}{m}\vec{A}_{abs} \cdot \vec{p}$.

By Fermi's Golden rule and the dipole approximation, [14] the XAS cross-section for the unit cell is:

$$\sigma_{abs} = \sum_{i}^{\langle cell \rangle} \sum_{a_i} \sum_{f} \frac{\frac{2\pi}{\hbar}|\langle f_i|\frac{e}{m}\vec{A}_{abs} \cdot \vec{p}_{a_i}|a_i\rangle|^2 \delta(E_{f_i} - E_{a_i} - \hbar\omega)}{n_{u,\vec{k}} c/V}$$

$$= \sum_{i}^{\langle cell \rangle} \frac{4\pi}{k} Im[\sum_{a_i} \sum_{f_i} (\frac{r_0}{m} \frac{|\langle f_i|\hat{\epsilon}_u \cdot \vec{p}_{a_i}|a_i\rangle|^2}{E_{f_i} - E_{a_i} - \hbar\omega - i\gamma})] = \frac{4\pi}{k} r_0 f^{uu}_{2,i}(\omega), \qquad (2.5)$$

where the relation $\pi\delta(E_{f_i} - E_{a_i} - \hbar\omega) = Im[(E_{f_i} - E_{a_i} - \hbar\omega - i\gamma)^{-1}]$ was used to go from the first line to the second line in Equation 2.5; $E_{f_i(a_i)}$ is the energy of the final (initial) scattered state and $f^{uu}_{2,i}(\omega)$ is the imaginary part of the atomic forward scattering amplitude for which the incident and scattered x-ray polarization states are the same. This equation states that the absorption cross section is proportional to the imaginary part of the resonant forward scattering amplitude. An experiment that measures the x-ray absorption, therefore, permits one to also calculate the real part of the resonant forward scattering amplitude using Kramers-Kronig transforms. It is in this way that XAS can

provide valuable clues regarding the behavior of the scattering amplitude.

The usual experimental geometry for XAS is transmission of a direct beam through a sample in order to determine the the attenuation length of the x-rays as a function of beam energy. As will be discussed, this is not practical for soft x-rays most of the time, but the basic ideas for this kind of experiment are the same for any other variant of XAS.

There is a simple relationship between the attenuation coefficent and the susceptibility. To determine what the relationship is, consider the case of a transmission geometry x-ray absorption measurement of a flat slab of an isotropic material. The intensity of a beam travelling through such as slab varies as $I \sim |e^{inkz}|^2$, where n is the index of refraction, k is the wave vector, and z is the depth into the sample. For an absorptive material, n is a complex quantity. For isotropic media, $n = \sqrt{\epsilon/\epsilon_0} = \sqrt{1+\chi}$, where ϵ is the dielectric permittivity. For weak scattering, $n \sim 1 + \frac{1}{2}\chi = 1 + \frac{1}{2}(Re[\chi] + iIm[\chi])$. By comparison with Equation 2.2, in the forward scattering limit, and Equation 2.5, $I \sim e^{-Im[\chi]kz} = e^{-r_0 \frac{\lambda^2}{\pi V_{cell}} f_{2,i}^{uu} kz}$, from which we can read off the absorption coefficient:

$$\alpha = kIm[\chi] = 2r_0 \frac{\lambda}{V_{cell}} f_{2,i}^{uu}. \tag{2.6}$$

With simple algebra $f_{2,i}^{uu}$ can be obtained.

Transmission measurements of the absorption coefficient is relatively straight forward for high energy x-rays, but the penetration depth of soft x-rays near 1 keV is ~ 1000 Å[14]. This is often insufficent for transmission geometry XAS. However, we can measure XAS by other means. Absorption of x-rays creates excited electron states that, when they relax, causes the emission of fluorescence x-rays or Auger electrons. The rate at which emitted electrons and photons are produced due to core hole annihilation is proportional to the absorption cross-section [14]. Therefore, counting the fluorescent photons created by radiative relaxation processes, using a technique called fluorescence yield (FY), or counting the electrons emitted in non-radiative atomic relaxation processes by the electron yield (EY) technique, affords us a means of measuring XAS and calculating $f_2^{uu}(\omega)$.

Now that the principles of the measurement techniques are better understood, the manner in which data is taken can be described, as it is in the next section.

2.2 Techniques and Hardware

This section describes how x-ray scattering and absorption data is obtained from a sample.

Three things are required to perform an x-ray scattering experiment. First, a beam of monochromatic x-rays with a narrow spread of wavevectors is needed to probe a sample. An x-ray beam missing either of these characteristics will

spoil the momentum resolution of the experiment and wash out the scattering. A large beam energy bandwidth also washes out resonance features. The second requirement is a detector to count x-rays scattered from the sample. Lastly, there needs to be a way to reliably alter the orientation of the momentum transfer with respect to the sample, which is done with machines called diffractometers.

Most of the data shown in this dissertation were collected using two different types of light sources: synchrotrons, such as the National Synchrotron Light Source (NSLS); and x-ray tubes such as those at the Center for Microanalysis of Materials (CMM) here at the University of Illinois.

Since the design of x-ray detectors and diffractometers often depend on the type of light source used, this discussion has been divided into two parts: the equipment and techniques used at synchrotron sources for soft x-ray studies, like the NSLS; and those used for hard x-ray diffraction at facilities like the CMM.

2.2.1 Synchrotron X-ray Experiments

At synchrotrons, relativistic electrons in storage rings are accelerated along curved trajectories to produce radiation. A "searchlight" cone of radiation is emitted tangent to the trajectory, and the angular width of the cone is inversely proportional to the Lorentz contraction factor γ. Since $\gamma \sim E$, the energy of the electrons in the storage ring, high energy electrons make for narrow cones of synchrotron light, naturally resulting in low beam divergences.[13] Using the NSLS as an example, the storage ring there is formed by eight straight segments forming a ring with a circumference of 170.08 m. Electrons are injected into the ring using a linac and their energy is boosted to E = 2.801 GeV.

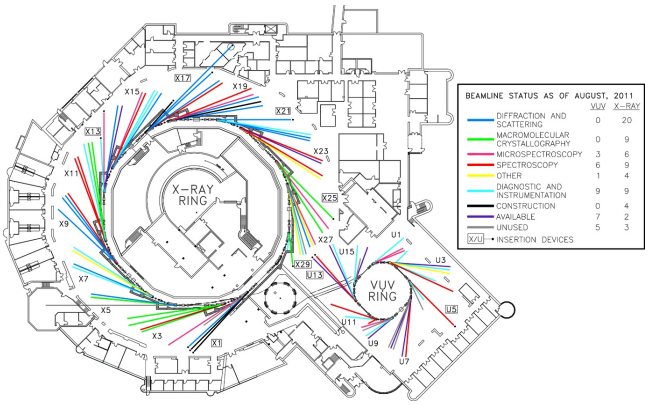

Figure 2.1: Schematic of the National Synchrotron Light Source. The colored lines radiating from the x-ray ring represent beam lines. Courtesy NSLS.

Insertion devices comprising arrays of regularly spaced magnets in the straight segments create periodic magnetic fields that alter the trajectory of the electron beam, concentrating the x-ray intensity into particular wavelengths. The X1B

insertion device is a 35 period planar undulator, typically run with a gap of 36 mm between the magnet arrays.

The "white" beam generated by the undulator is monochromatized for use in experiments. Generically, monochromators are systems of focusing mirrors and either high-quality single crystals—the Bragg peaks of which are used to pass specfic x-ray energies—or gratings that diffract the white beam. At X1B, the mirror/grating combination is used, in a design strongly influenced by C. T. Chen's "Dragon" monochromator. [24] Details of the X1B monochromator have been published in Reference [25] and its basic components are shown in Figure 2.2. The white beam first meets a set of Kirkpatrick-Baez mirrors that

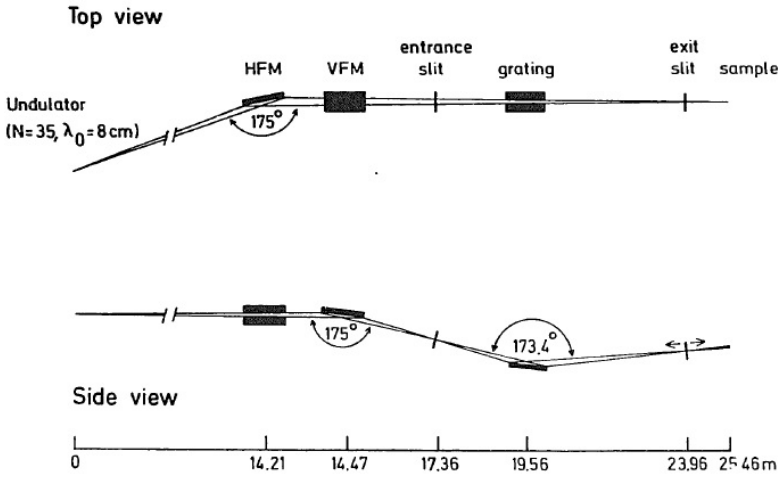

Figure 2.2: Schematic of the X1B monochromator. The white beam from the undulator (left side of figure, not shown) is directed at a pair of perpendicularly oriented focusing mirrors (HFM and VFM). HFM focuses the beam on to the sample position 11.25 m downstream (right side of the figure). VFM focuses the beam reflected from HFM onto the entrance slit 17.36 m away from the undulator. The grating diffracts the white beam and focuses the diffracted beam toward the exit slit. The position of the exit slit is variable, as the focus of the diffracted beam varies with beam energy. The size of the exit slit is also adjustable. Taken from Reference [25]

steer and focus the white beam downstream. The horizontal mirror (HFM in Figure 2.2) focuses the beam on the sample position far downstream. The vertical mirror (VFM in Figure 2.2) focuses the beam on the entrance slit, which can be narrowed to screen out aberrant light due to optical defects in the mirror. Passing through the entrance slit, the white beam is diffracted by a spherical grating. Uusually, a 1200 line/mm grating was used in the studies of this dissertation. The grating focuses the diffracted beam onto a translatable exit slit, which can be placed 6.14 - 7.84 m downstream of the grating. Since the position of the focus is wavelength dependent, the exit slit can be placed at that position if that x-ray wavelength is desired. The width of the exit slit controls the energy bandwidth, and the exit slit width varied from ≈ 1 μm to

≈ 200 μm in these studies. The nominal resolving power is $\Delta E/E \approx 3 \times 10^{-4}$; near Cu $L_{3,2}$ transition edges, ΔE $\sim$ 0.28 eV; and near Fe $L_{3,2}$ edges, ΔE $\sim$ 0.21 eV.

At the sample position, the nominal spot size is horizontally 2.0 mm wide and vertically 0.050 mm tall. This can be altered by adjusting a beam mask just upstream of the scattering chamber, which will be described shortly.

Being able to use this very bright and monochromatic x-ray beam comes at a price: since the synchrotron storage ring operates in ultra high vacuum and soft x-rays strongly attenuate in air, all components of the beam line must have pressures $P \sim 5{\times}10^{-9}$ mbar or better, including the scattering end station. This vacuum requirement forces the X1B end station to have certain characteristics.

Regardless of what kind of environment it needs to operate in, the basic design of diffractometers is generally the same: [23] a sample is mounted on a series of nested rotation stages that rotate the sample about one point in space. A second series of rotation stages move an x-ray detector about the same center of rotation as the sample stage. The incident beam is steered through this point; no matter what the positions of the sample or detector, the center of the incident beam will always hit a particular part of the sample and the detector will always observe that illuminated area. This precise alignment of sample, beam, and detector has the benefit of allowing us to reliably calculate the momentum transfer using the angles of the diffractometer stages.

An example of such a diffractometer, made for high vacuum environments, is the Spinoza diffractometer maintained by the Abbamonte research group at beam line X1B, NSLS, Brookhaven National Laboratory. The diffractometer resides in a stainless steel high vacuum chamber, with chamber pressure $P \sim 5 \times 10^{-9}$ mbar. Pictures of the end station are shown in Figure 2.3.

A point detector is mounted on the TwoTheta rotation stage, the motion of which is confined to a plane defined by the direct (incident) beam and the polarization: at X1B, the linear polarization is horizontal to the lab floor. This plane is called the scattering plane and it is illustrated in Figure 2.4. The zero of TwoTheta is the position at which the direct beam and the center of the detector are aligned. The TwoTheta at which a reflection is observed defines the magnitude of the momentum transfer: $q = \frac{4\pi}{\lambda} sin(TwoTheta/2)$ where λ is the x-ray wavelength.

The sample orientation is controlled using the Theta, Chi, and Phi stages, on top of which is the sample stage. The rotation axis of Theta coincides with that of TwoTheta and it is the primary rotation used to excite reflections in the sample. In the reference frame of the sample, Theta motion sweeps the direction of $\vec{Q}$ along the scattering plane. Theta and TwoTheta are related so that if Theta rotates at half the rate of TwoTheta while tracking a reflection, this coordinated "Theta/TwoTheta" scan serves to fix the direction of the momentum transfer relative to the sample coordinate system while increasing $|\vec{Q}|$. The Chi and Phi stages rotate with Theta: for Theta = 0, the Chi axis is parallel to the

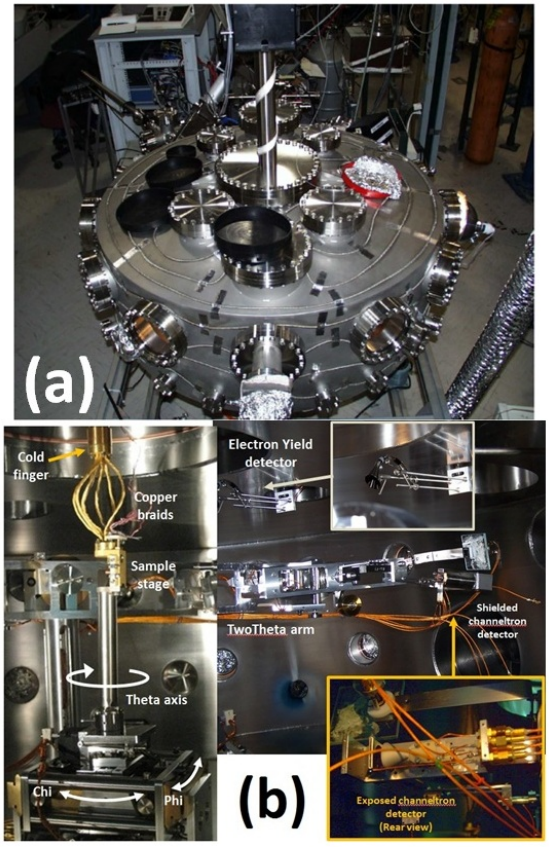

Figure 2.3: (a) Stainless steel high vacuum chamber containing the Spinoza diffractometer at X1B, NSLS. (b) A mosaic of pictures of the Spinoza diffractometer. The sample stage on the left of the image is mounted on top of a stainless steel tube, connecting it to the Theta/Chi/Phi rotation stages below it. The motions of each of the stages is illustrated. Copper braids connect the top of the sample stage to the bottom of the flow cryostat cold finger. The TwoTheta arm extends across part (b); at the end is a shielded channeltron detector. The inset in the orange box shows the exposed channeltron. The electron yield detector is on top of the chamber and is shown in greater detail in the white framed inset.

direct beam and the Phi axis is perpendicular to it and Theta. Seen again in the sample frame, Chi motions sweeps $\vec{Q}$ in a plane perpendicular to the scattering plane. Generally, Chi and Phi are used less often than Theta, and primarily to make fine adjustments to the sample orientation.

Both the TwoTheta and Theta stages can reliably make angle steps as small as 0.0005°. The point detector is located 40 cm away from the center of rotation. This distance, and the scattering slits placed in front of the detector, determine the angular resolution of the detector.

The diffractometer motions are controlled by computers, which can also perform the trigonometry required to calculate the orientation of the momentum transfer in the sample's crystallographic coordinate system. This capability also

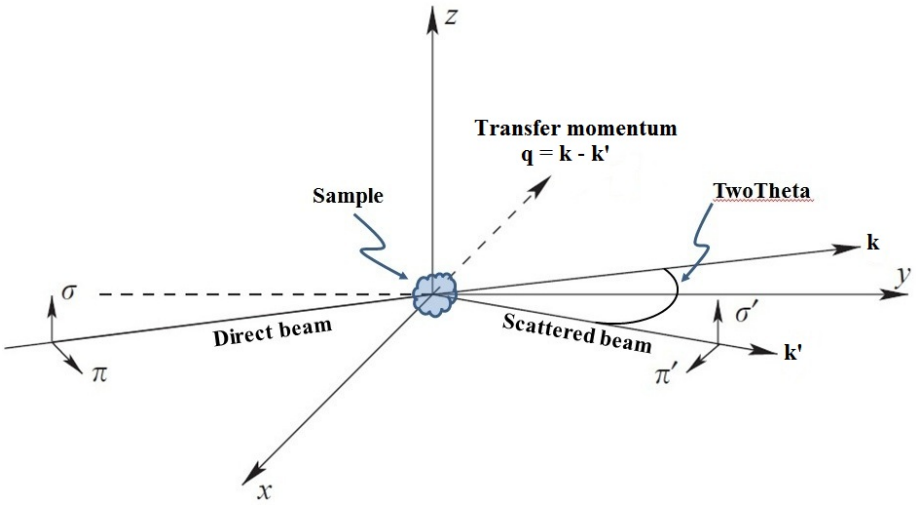

Figure 2.4: A schematic of the scattering geometry. The direct beam ($\vec{k}$) is incident on the sample from the left. The σ and π labeled arrows perpendicular to the incident beam indicate the direction of the linear polarization with respect to the scattering plane, defined as the plane defined by the incident ($\vec{k}$) and scattered ($\vec{k}'$) beam. TwoTheta is the angle between the incident and scattered wave vectors. The momentum transfer is defined in the figure and called $\vec{q}$. Adapted from S.W. Lovesey et al., Physics Reports **411**, 233289 (2005).

allows us to move the diffractometer to make scans in specific directions in the sample reciprocal space.

There are several commonly used types of scans. First, there are motions of single angle stages, often called "line scans" (as they trace straight lines in Theta). Theta scans are the most common of these, especially in alignments to Bragg peaks and characterizing the spread of misoriented crystallographic domains in the sample. There are also coordinated angle scans, such as the aforementioned Theta/TwoTheta scan, which is very handy for measuring reflectivity curves from thin films or determining the momentum transfer magnitude of a Bragg peak. The computer can also coordinate the diffractometer motion to scan along straight line trajectories in reciprocal space. Denoting position in reciprocal space by Miller indices, one can perform H (or K or L) scans so that only the Miller index H (or K or L) changes in a scan. Scans not along high symmetry directions are also permitted. In both reciprocal and angle space, scans over regular meshes of momentum or angle space points can be made—mesh scans.

X1B is a tunable x-ray source and this adds another dimension to the scans. Scans can be done at different constant beam energies and meaurements taken while on the resonance condition can be compared to simliar measurements obtained off resonance. In this way, one might distinguish between scattering peaks that are due to electronic ordering or those simply due to structural diffraction, which should persist at all energies. The diffractometer and the

beam energy can be coordinated, so that the energy dependence of a single peak in reciprocal space can be determined, in what are called "fixed Q" energy scans.

The sample temperature is controlled using a flow cryostat with a base temperature of $\approx$ 18 K, which is connected to the sample stage by copper braids. The sample stage is connected to the Theta/Chi/Phi stages by a thin walled stainless steel post; given the poor cryogenic thermal conductivity of stainless steel, this effectively isolates the sample stage from the diffractometer. To ensure good thermal contact between the sample and the oxygen-free copper sample stage, the sample is glued onto a block of oxygen-free copper using air-drying high purity conductive silver paint, usually from SPI Supplies, Inc. The block is, itself, mounted on a stainless steel carriage, the shape of which complements the shape of a slot in the sample stage. Once inserted, the stainless steel carriage is secured by tightening a screw that slightly distorts the shape of the sample stage.

This same experimental set up is used to obtain x-ray absorption data. The operation of the diffractometer to collect absorption spectra is simpler than it is to collect scattering data. In this case, TwoTheta and Theta are used to change the grazing angles of the incident beam and x-rays exiting the sample and, once chosen, can be held constant. As mentioned earlier, in Equation 2.6, the emission intensity is, in principle, proportional to the attenuation coefficient, α. The measured XAS can then be used to calculate $\sum_i^{\langle cell \rangle} f_{2,i}^{uu}$. Using tabulated values of $f_2(\omega)$ for elements Z = 1 - 92, [26], it is possible to calibrate the XAS data and obtain an expression for $\sum_i^{\langle cell \rangle} f_{2,i}^{uu}$ in absolute units of $f_2(\omega)$.

The most commonly used method to obtain XAS in this dissertation is the fluorescence yield (FY) technique. In all cases, the FY detector (same as the point detector on the TwoTheta arm) accepted all light, and no energy discrimination was made of the FY x-rays.

The heart of the FY technique lies in the change of absorption coefficients with x-ray energy, which changes the penetration depth of the x-ray beam. Both the incident x-rays and the fluorescent x-rays can be absorbed. If the incident beam penetration depth decreases, more fluorescent light is generated near the surface and can escape the sample before being absorbed. If the penetration depth increases, then more fluorescence is generated deep in the sample and much of those x-rays will be absorbed before exiting the sample. This "self-absorption" mechanism is exploited in the FY technique: the signal is high when the attenuation coefficient is large (penetration depth is small) and vice versa. [27] The greater the self-absorption, generally the more proportional the signal is to the attenuation coefficient, and the weaker the overall FY signal is. Theta and TwoTheta must then be adjusted till the best compromise between XAS proportionality to $f_2(\omega)$ and signal intensity is made.

To adjust how much the self-absorption affects the XAS, one uses different combinations of Theta and TwoTheta. To increase the effect of self-absorption,

Theta is usually oriented to make the beam hit the sample nearly normal to the sample surface, so as much of the incident light gets buried in the sample. Two-Theta is also made such that the fluorescence x-rays observed exit the sample with low take off angles with respect to the surface, which means exiting x-rays must pass through as much of the material as possible.

On occasion, the electron yield (EY) technique is used instead to obtain XAS, in which photoelectrons and Auger electrons emitted from the sample are collected by a dectector. As in the FY case, all electrons of any energy are collected by the detector. In contrast to the FY technique, the emitted electrons have an escape depth of ~ 100 Å, thus this technique is more surface sensitive than FY. [14] The limited escape depth limits the utility of EY as a bulk probe, and surface contaminants can have a greater effect on EY spectra than FY spectra. [27]

The detector used in EY measurements is different from the detector used in FY measurements, since the FY detector is designed to repel from it electrons and stray ions in the chamber. The EY detector is not—it is totally exposed to the chamber environment, as shown in Figure 2.3—as opposed to the FY/coherent scattering detector, which is shielded.

2.2.2 Experiments with X-ray Tube Sources

In this section, we discuss the equipment used in hard x-ray diffraction studies at the CMM. This discussion is shorter than that of the previous section since the Spinoza diffractometer and the diffractometer used at the CMM are rather similar.

The device used at the CMM is the commercially available X'Pert diffraction system, developed by PANalytical B. V.

The light source is an x-ray tube and the underlying mechanism of x-ray production is x-ray emission. The basic operation involves electrons emitted by a hot filament colliding with a metal anode target. Cu targets were used in this work. The incident electrons collide with electrons of the inner shell orbitals of the anode atoms; the incident electron is deflected and an inner shell electron is ejected. To fill the vacant inner shell state, an electron in an outer shell orbital drops to fill the hole, emitting a photon. The predominant emission line is Cu K_α. Note that this is the same mechanism behind the fluorescence yield technique used at X1B. The emission lines are sharp in energy and of high intensity, but the emission is also accompanied by a Bremsstrahlung background spectrum. Further, fluorescence has no angular dependence, so only a small fraction of the emitted photons can be used in an experiment, making the process rather inefficent. [20] Also, compared to synchrotrons, the energy of the x-ray beam cannot be arbitrarily tuned: this way of x-ray generation is tied to the x-ray emission energy of the anode target.

The high-resolution parallel beam configuration of the X'Pert system monochro-

mator is characterized by a hybrid x-ray mirror and a 2-bounce single crystal mirror system, resulting in a 30 arc-sec primary beam divergence. The incident beam intensity is $\sim 10^7$ photons. (This should be compared to X1B where the incident beam intensity is $\sim 10^{11}$ photons.) The bandwidth of the incident beam is $\Delta\lambda/\lambda = 4 \times 10^{-4}$.

The X'Pert diffractometer, similar to the Spinoza diffractometer, is a four-circle system, with vertically aligned Theta and TwoTheta axes and Psi and Phi rotations, which are analogus to the Spinoza Chi and Phi except that the way in which they are mounted on the Theta stage is interchanged.

The X'Pert detector is a line detector: a 255 pixel array with 2.50° total angular acceptance.

3 Orbital Ordering in $KCuF_3$

Given a concrete combination of interacting electron orbital states on two ion sites, the superexchange model can predict the strength and sign of the spin exchange between electrons on the orbitals. However, superexchange provides no means by which to decide which set of orbitals to consider. Electrons in metal-oxide systems can, in principle, inhabit degenerate manifolds of orbital states, such as the example of Cu^{2+} provided in the introduction. How do we decide what the magnetic states of such systems are when they display orbital degeneracy?

For orbitally degenerate systems, the paradigm has been the orbital ordering approach developed by K. I. Kugel and D. I. Khomskii [5], which treats electron orbital states as spin-like quantities that order themselves via exchange interactions. The Kugel-Khomskii (K-K) model incorporates these orbital pseudospins into a generalized superexchange model. Orbital ordering approaches like the K-K model has met with success, correctly describing the symmetry of the magnetic ordering in $KCuF_3$ and finding useful application to other orbitally active systems like the manganites. [1]

As mentioned in the introductory chapter, though $KCuF_3$ is the simplest orbital ordering system, some of the quantitative predictions of the K-K model for the magnetism of $KCuF_3$ do not compare favorably to experiment. These deficiencies are due to the assumptions made in the orbital ordering approximation (OOA), which is the cornerstone of the K-K model. We shall briefly discuss the OOA and then examine the discrepancies between the predictions of the K-K model and the experimental observations made of $KCuF_3$. As will be shown, there is a compelling need to re-examine the physics of the K-K model.

Much of the material presented in this chapter has been published in Reference [39] and it is reproduced here with the permission of Nature Publishing Group. A list of contributions by each of the authors of Ref. [39] is listed in the paper.

3.1 $KCuF_3$, the Orbital Ordering Approximation, and the Kugel-Khomskii Model

Orbital ordering refers to the spatial pattern in which electron orbitals on the transition metal sites of a solid are occupied. Prior to the introduction of the K-K model, this orbital ordering was at one time considered a by-product of the structural order. In most transition metal compounds, the degeneracy of orbital manifolds is lifted by spontaneous distortions of the lattice. Such compounds are unstable to these distortions because the resulting reduction of the point group symmetry of the structure, which lifts the degeneracy of the manifolds, results in a reduction of the total energy. This effect is called the Jahn-Teller effect. [28] When the octahedral environment around a Cu^{2+} ion becomes tetragonally distorted the e_g manifolds splits, as illustrated in Figure 3.1. A doubly occupied b_{1g} manifold is lowered in energy at the price of raising the energy of a singly occupied a_{1g} state, resulting in an overall energy gain. Metal-ligand complexes

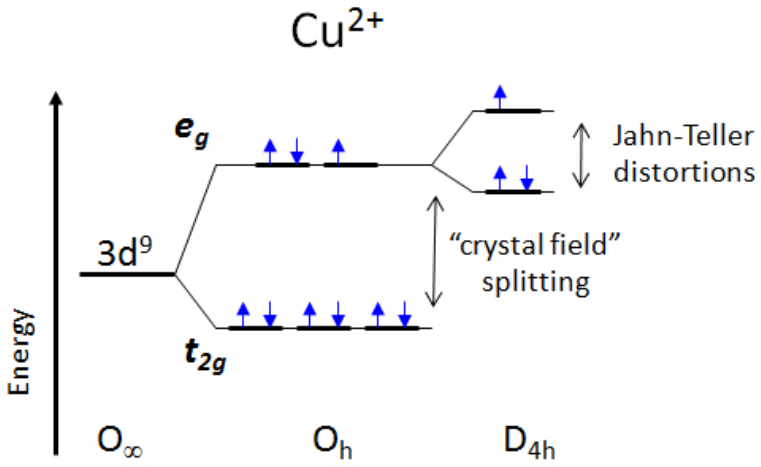

Figure 3.1: The crystal field states of Cu^{2+}: in a spherically symmetric environment (O_∞), in an octahedral setting (O_h), and tetragonal point group D_{4h}. The tetragonality is introduced by Jahn-Teller distortions of the lattice.

often share ions (the corners of octahedra, for example) so that the distortions of one unit cell must be met with complementary distortions in neighboring cells. This induces the correlations in orbital occupation between the metal sites of the system that is referred to as orbital ordering.

To understand the electronic structure of such a system, it needs to be understood what the characteristic wave functions of these new electron orbital states are. To solve such a problem, one must solve a coupled structural and electron dynamics problem, which is usually very challenging. [29]

The OOA allows structural and electron degrees of freedom to decouple, so that each aspect of the problem can be solved separately, resulting in a great simplification. This is done by shifting the center of the phonon mode coordinates such that they vary around positions that correspond with minima of the combined elastic and Jahn-Teller energies of the system. This disentangles the lattice potential energy from electronic dynamics in the Hamiltonian and allows the separation of nuclear and electronic variables in the wave function. In principle, calculating the potential minima is not easier than solving the Jahn-Teller problem, but it does create a very tidy formal separation of variables. [29]

Note that in this approach, orbital degeneracy is preserved since no crystal field-induced splitting of the e_g manifold is considered. This degeneracy is handled by considering the orbital state as a pseudospin, the basic entities of orbital ordering models.

This method was introduced by J. Kanamori [30] to analogize the Jahn-Teller problem to an Ising-like problem, which is theoretically much better understood. For two-dimensional e_g manifolds, Kanamori assumed that the solution wave functions are linear combinations of $d_{x^2-y^2}$ and $d_{3z^2-r^2}$ orbital states. In this formalism, the states of the two-dimensional manifold are treated as eigenfunctions of the σ_x and σ_z Pauli matrices for the spin-$\frac{1}{2}$ problem. These matrices were chosen because they transform under symmetry operations in the same way as the normal modes of the lattice. The possible solutions to this orbital ordering problem take the form:

$$\phi = \cos\frac{\theta}{2}\phi_{z^2} + \sin\frac{\theta}{2}\phi_{x^2-y^2}, \tag{3.1}$$

where θ is a real valued angle and ϕ_{z^2} and $\phi_{x^2-y^2}$ are the wave functions of the $d_{x^2-y^2}$ and $d_{3z^2-r^2}$ orbital states.

The two-component orbital pseudospins on neighboring sites are coupled by exchange-like interactions. Formally, the sign and magnitude of the exchange constants are dependent on what the potential energy minima are. To bypass this, we need to have detailed knowledge of lattice and electronic properties of the metal-ligand system, the exchange constants are treated as effective parameters. This is a common feature of all orbital ordering models. [29]

Once the pseudospin ordering problem is solved, the structural distortions can be easily obtained. Since the wave functions are eigenfunctions of Pauli matrices that have the same symmetries as the normal modes, the linear combination of normal modes that characterizes the distortion is analogous to the linear combination of pseudospin states. As Polinger points out, this turns upside down the normal way of approaching orbital ordering by treating the distortion of the lattice as consequences of the orbital ordering rather than the other way around. [29]

The K-K model uses the simplifications of the orbital ordering approach to

understand how the orbital ordering modifies the superexchange interactions between electron spins. [5]

Their approach, like P. W. Anderson's treatment of superexchange, [11] treated the electron hopping (kinetic energy) as a perturbation to the system and explicitly considered the effect of orbital degeneracy on the spin exchange parameters. Electron hopping parameters (t) between neighboring sites are treated as functions of the relative orientation of pseudospin states on those sites, in line with the superexchange paradigm except the orbital states are now free to arbitrarily "rotate" around their ion sites instead of assuming certain discrete states. Because t is a function of the orbital mixing angles θ on two sites, the spin superexchange terms (which go as $\sim t^2/U$) between those sites is affected. The symmetry of the orbital ordering, as reflected in the relationship of θ between two neighboring pseudospin sites, determines the symmetry of the electron spin ordering. [5]

The K-K model also explicitly considered the role of the Hund's rule coupling, or the direct spin exchange between electron spins on the same site but different orbital states. They found that the ratio of the Hund's rule coupling to the on-site repulsion parameter, J_H/U, acts as a scaling parameter to the electron spin exchange. Kugel and Khomskii also concluded that the ratio of the spin ordering temperature and orbital ordering temperature is determined by the value of J_H/U. [5]

Arguably, the first successful application of the K-K model was $KCuF_3$: the model successfully captured the symmetry of the electron spin ordering and the anisotropy of the spin exchange in an unambiguous way. $KCuF_3$ is the necessary first test since it is the simplest orbital ordering system, possessing only one unpaired electron in the e_g manifold.

The model predicts that the e_g hole orbitals in $KCuF_3$ order in an "antiferro" orbital pattern once the system cools below a single, presumably high orbital ordering temperature (T_{OO}). T_{OO} of $KCuF_3$ has never been experimentally observed, as the material undergoes an irreversible change around $\sim 600K$ [31] before that temperature could be reached. Given values of $J \sim 1$ eV and $U \sim 10$ eV typical for perovskites, T_{OO} is expected to be at most ~ 10 times higher than the spin ordering temperature T_s.

The resulting electron spin exchanges are predicted to be A-type antiferromagnetic, which was confirmed in neutron scattering observations by M. T. Hutchings et al [32] and S. K. Sajita et al [33], who measured the Néel temperature to be $T_N = 39 \pm 1$ K. Anisotropy in the electron spin exchange terms between c-axis and a-b plane coupling is predicted in the model. An extreme anisotropy has been observed in Ref. [33]: using linear spin-wave theory and a theoretical model of the spin dispersion relation for spin-$\frac{1}{2}$ 1-D Heisenberg antiferromagnets to fit the data, it was found that $J_{ab} = -2$ K and $J_c = 203$ K.

The cooperative Jahn-Teller distortion responsible for the tetragonal distorts the cubic perovskite structure, which comes as a consequence of the orbital

ordering in this model, has been observed. Past neutron and x-ray diffraction studies classify the structure as I4/mcm, [32] [34] which is characterized by a "two-in, two-out" distortion pattern of F ions in the a-b plane, as shown in Figure 3.2. $KCuF_3$ can exhibit two different types of such distortion: our interest

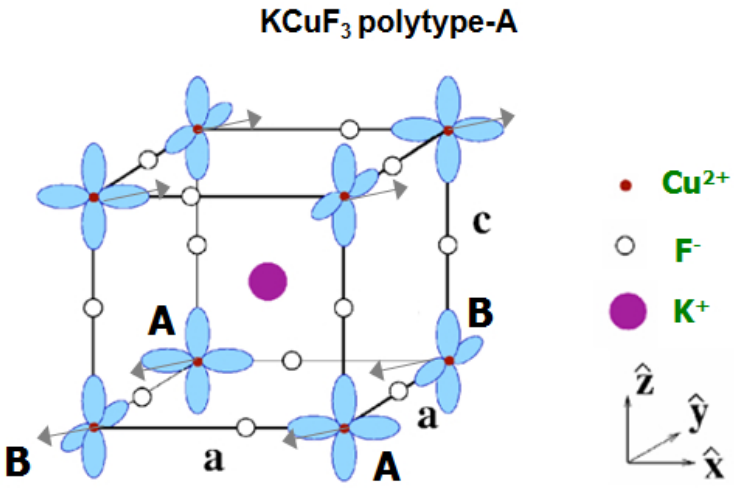

Figure 3.2: $KCuF_3$ structural variant polytype A. F ions are located on the edges of the cubic cell and the hole orbitals on the Cu sites are illustrated as blue orbital shapes. Electron spins at each Cu site are denoted by the grey arrows. Notice that they form an A-type antiferromagnetic order. The Jahn-Teller distortions are characterized by distortions of the F ions in the x-y plane away from their central positions between Cu sites, as illustrated in the figure. Figure adapted from: N. Binggeli and M. Altarelli, Phys. Rev. B **70**, 085117 (2004); and Reference [36].

in this study is in polytype A, characterized by "two-in, two-out" distortion direction reversing between adjacent a-b planes. Above T_{OO}, this distortion should disappear, as the orbital order vanishes and the structure relaxes to the ideal cubic perovskite.

Overall, the comparison between experiment and the K-K model is favorable, as the model provides predictions that are in good qualitative agreement with exchange anisotropy findings and the observation of A-type antiferromagnetism.

However, the K-K model comes short in terms of quantitative predictions for $KCuF_3$. For example, the predicted T_{OO} of the original model is too low. Subsequent refined versions of the model, including the LDA + DMFT calculation of Pavarini et al [35] which places $T_{OO} \approx 350$ K, also give unrealistic orbital ordering temperatures. The observed $T_{OO}/T_s \approx 20$ cannot be replicated by the K-K model either, as the highest value of T_{OO}/T_s the model can give, even with choices of effective parameters that are unrealistic for $KCuF_3$, is ≈ 10. This is serious, as the model neither accounts for the absolute values of the important energy scales of the problem, nor adequately describes the relative values of

these energy scales. Finally, the extreme spin exchange anisotropy in $KCuF_3$, $J_c/J_{ab} \approx -100$, cannot be captured, implying that the model is missing some important physics concerning the spin interactions.

These inadequacies in the K-K model have spurred on additional experiments on $KCuF_3$, with results that further challenge the validity of the model. Resonant x-ray scattering studies conducted by Paolasini et al [36], data from which is shown in Figure 3.3, discovered a low temperature orbital ordering transition. They did this by studying the (3, 3, 1) Bragg peak, a weak reflection

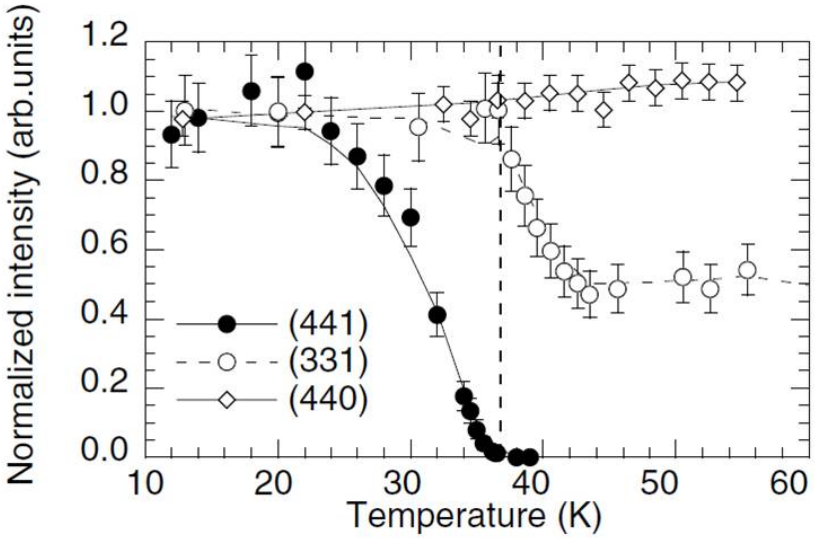

Figure 3.3: Cu K edge resonant x-ray scattering from Reference [36]: the (3, 3, 1) Bragg peak, attributed to orbital ordering in $KCuF_3$, increases in intensity at 43 K and stabilizes at the Néel temperature. Note that the (4, 4, 0) peak does not display a significant temperature dependence.

attributed to orbital ordering, using the $1s \rightarrow 4p$ dipole transition at $E \approx 8989$ eV to enhance the scattering signal. The integrated intensity of this peak was compared to the temperature dependence of the (4, 4, 1) magnetic peak and the structural Bragg peak (4, 4, 0), which is unaffected by the Jahn-Teller distortion. The (3, 3, 1) peak intensity is steady until the sample is cooled to $T \approx 43$ K, below which the intensity increases until it stabilizes at onset of the Néel state. The (4, 4, 0) structural peak intensity did not vary in this temperature range, indicating that temperature dependence of (3, 3, 1) is unrelated to a structural transition. This result runs contrary to the conclusion of Kugel and Khomskii that there is only one characteristic orbital ordering energy scale. To explain their data, Paolasini et al formulated a mean field theory that directly coupled the orbital and spin order parameters. Tuning the effective parameters of their model, they captured both the low temperature orbital order transition and the Neel transition at $T_N \approx 39$ K. Interestingly, the orbital ordering temperature they obtain by their model is $T_{OO} \sim 800$ K.

The role of the structure should not be ignored. Leaving aside the sim-

plifications of the OOA, the structure of $KCuF_3$ plays an important role in determining the character of its magnetism. The structure of $KCuF_3$ is also still a matter of debate: neutron scattering studies indicate that it is tetragonal but there are indications in contemporary experiments that this is not the case.

Electron paramagnetic resonance (EPR) experiments by I. Yamada et al [37] found evidence that the structure is not tetragonal but orthorhombic. The magnetic field orientation dependence of the EPR line width was found to vary as $\Delta H \sim (2 + sin\theta)$, where θ is the angle between the applied field and the c-axis. This angular dependence is only explicable if there is a Dzyaloshinsky-Moriya interaction (as discussed in the Introduction) between electron spins on Cu sites along the c-axis. The I4/mcm space group places the apical F ion at the midpoint between the Cu sites along the c-axis, running contrary to the requirement that there be no local inversion center between the two sites coupled by the Dzyaloshinsky-Moriya interaction.

This contradiction between the EPR data and structural space group assignment led Hidaka et al [34] to perform their own x-ray structure refinement. They collected 936 reflections with structure factor intensities greater than three standard deviations and performed a least-squared refinement. They found that the data exhibited extinction rules consistent with orthorhombic symmetries, which they attributed to static shifts of apical F ions from high symmetry positions along the 110 directions. (See Figure 3.4). This should have resolved the con-

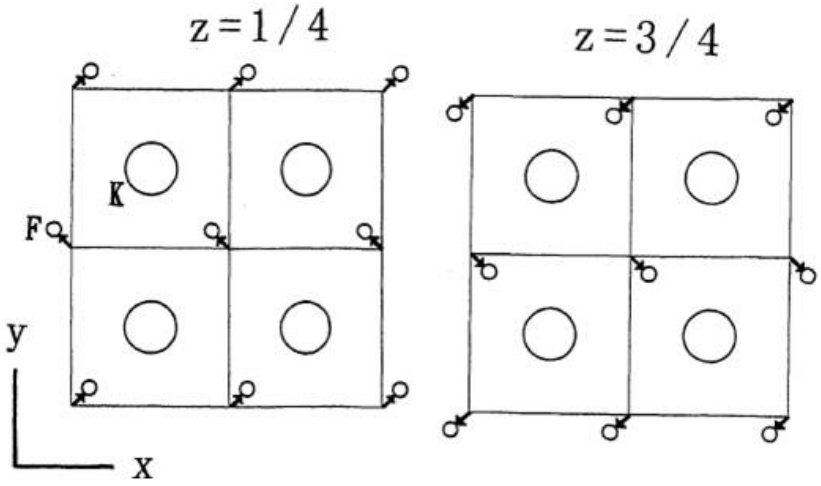

Figure 3.4: Orthorhombic shifts of the apical F ion along {110} directions away from high symmetry positions in $KCuF_3$. From Reference [34].

tradiction between the structural data and the EPR line width measurement of Yamada et al., but the data set obtained by Hidaka et al also forced them to conclude that the a and b lattice parameters were equal, which is highly irregular since an orthorhombic structure should have $a \neq b$. The x-ray data also found no indication of octahedral tilting, as would be expected by distortions of the apical F ion away from its high symmetry position.

Another EPR experiment, by M. V. Eremin [38], concluded that the Dzyaloshinsky-Moriya interaction need not require a static shift of the apical F ion, as Hidaka et al concluded in their study. Instead, Eremin et al. found that the EPR line width dependence on the applied magnetic field direction is better accounted for if an additional contribution from a dynamical anisotropic exchange arising from dynamic distortions of the apical F ion is accounted for.

These measurements suggest that phonon modes that involve displacements of apical F ions play a significant role in the orbital and spin interactions. There is no place in the K-K model to account for the influence such phonons might have on the magnetism.

3.2 A New Orbital Ordering Model of $KCuF_3$

In what follows, I will describe the conclusions we have reached regarding the role phonons play in electron spin ordering in $KCuF_3$. We add two new pieces to the puzzle of $KCuF_3$ in the form of Raman and x-ray scattering data. Our data demonstrates that the structure plays a decisive role in the magnetic order in $KCuF_3$ similar to the way Eremin et al supposed. The simplifications of the OOA led the K-K model to gloss over the effects of the structure on orbital ordering. We will present a new orbital ordering model for $KCuF_3$ that corrects this oversight. These results are also presented in Reference [39].

Naturally, emphasis will be given to x-ray scattering data in this section.

3.2.1 X-ray and Raman Scattering

In order to perform our experiments, Shi Yuan and I grew single crystal samples of $KCuF_3$ using the precipitation growth method described by Hirakawa and Kurogi. [40] Two of the samples we grew, and used in soft x-ray scattering experiments, are displayed in Figure 3.5. The samples were carefully screened

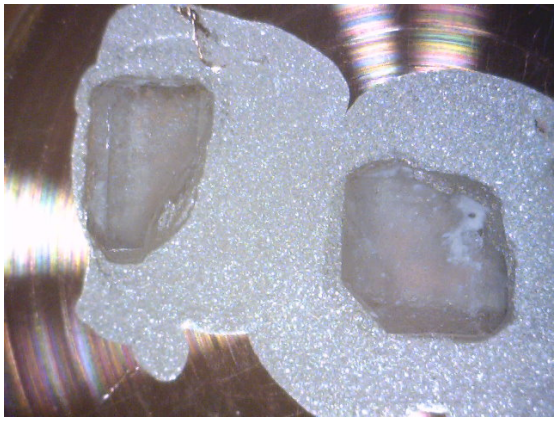

Figure 3.5: $KCuF_3$ crystals, glued onto a copper sample block with silver paint.

using Cu K_α x-ray diffraction to ensure that the samples studied were of the right structural variant, polytype A. This was done using the X'Pert 1 machine at the Center for Microanalysis of Materials, as described in the Methods chapter. Based on measurements of the c-axis parameters, which differ between polytype A and polytype D, we chose samples with volumes $> 90\%$ polytype-A.

We first present Raman scattering data taken by Shi Yuan. In this measurement, the temperature dependence of the long-wavelength lattice dynamics of $KCuF_3$ were probed. Data displayed in Figure 3.6. In the figure, the energy

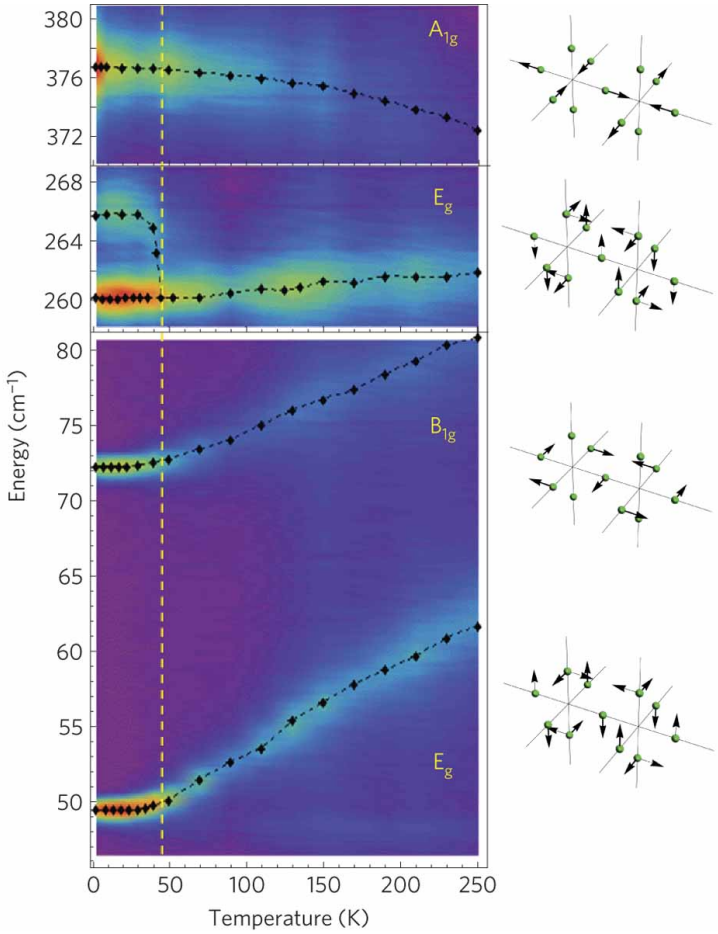

Figure 3.6: Temperature dependence of the Raman-active phonons in $KCuF_3$, and depictions of their corresponding eigenvectors showing displacements of the F ions. Taken from Ref. [39].

and intensity (as denoted by color, red being most intense and blue least) of four different Raman modes are tracked against the sample temperature. Typical anharmonic effects, attributable to the "stiffening spring constants" of the lattice, are displayed by the A_{1g} mode, the energy of which increases with decreasing temperature. The other three modes, labeled E_g and B_{1g} display an anomalous "softening" over a very wide temperature range, $\sim$ 50 K to 250 K. This is indicative of lattice fluctuations consistent with an incipient structural

phase transition. This supports the observations of Eremin et al.: lattice mode frequencies are decreasing, permitting the dynamic distortions of the apical F ions and the resulting non-zero Dzyaloshinsky-Moriya coupling vectors to persist over longer time scales, much longer than typical time scales for electronic exchange processes. [38]

At $T \approx 50$ K, the higher energy E_g mode splits, signaling the onset of a symmetry-lowering structural transition. The depictions of the Raman modes to the right of Figure 3.6 show that the softening modes, especially the higher energy E_g mode, involve displacements of the apical F ion away from high symmetry positions. With the onset of the ≈ 50 K transition, these dynamic lattice distortions slow down and become increasingly static.

Further examination of the Raman mode cartoons show that the associated F ion distortions are consistent with octahedral rotations and tilts. The character of these octahedral rotations and tilts can be compared to those of $GdFeO_3$, as shown in Figure 1.2, which occur in many perovskites, such as $LaMnO_3$. [41]

X-ray scattering data will now be discussed. These experiments were performed on our samples primarily at two locations.

Soft x-ray studies were conducted at beam line X1B, National Synchrotron Light Source, at Brookhaven National Laboratory, Upton, NY. Scattering measurements were primarily conducted at beam energies near the Cu $L_{3,2}$ edges ($\approx 933 - 952$ eV) with beam energy resolution $\Delta E \approx 0.28$ eV. The detector angular resolution was $\approx 1^\circ$. Fluorescence yield data was obtained near both Cu $L_{3,2}$ edges as well as near F K edge. Sample temperature was controlled using a flow cryostat with base temperature of ≈ 20 K. Additional information about X1B may be found in the Methods chapter.

Hard x-ray studies were conducted mostly at beam line 4ID-D, Advanced Photon Source, Argonne National Laboratory, Lemont, NY. A commercial available Huber 6-circle diffractometer was used to collect the scattering data. The beam energy used as a constant 8.8 keV, with $\Delta E \approx 1.23$ eV and was σ polarized. A Vortex Si drift diode was used for photon detection, with a pulse height analyzer employed to discriminate out x-rays that are from fluorescence as well as higher harmonics from the monochromator. Detector resolution was $\approx 0.02^\circ$. Sample temperature control was maintained using a closed cycle cryostat mounted on the diffractometer, with a base temperature of ≈ 6 K. Additional hard x-ray measurements were made at the end station on C-line, Cornell High Energy Synchrotron Source, Cornell University, Ithaca, NY.

The momentum transfer in the x-ray scattering data is denoted by Miller indices: $\vec{q} = 2\pi(\frac{H}{a_T}, \frac{K}{a_T}, \frac{L}{2c})$, with lattice parameters $a_T = 5.85\mathring{A}$, $2c = 7.82\mathring{A}$ consistent with the use of the tetragonal cell, as schematically shown in Figure 3.7 For comparison, the nearest neighbor Cu distance is $a = 4.14\mathring{A}$.

Soft x-ray studies were done with the primary aim of exploring properties of the A-type antiferromagnetism of this system. A wealth of interesting phenomena was found and the results confirm many previously reported properties

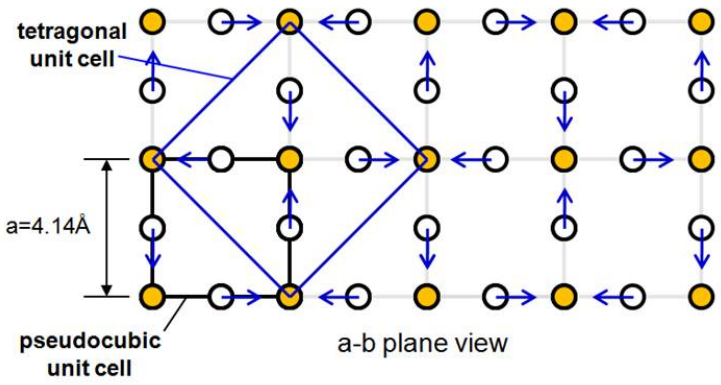

Figure 3.7: The a-b plane of $KCuF_3$. Yellow dots represent the Cu ions and white dots represent F ions. The direction of the distortions of the F ions due to the Jahn-Teller effect are indicated. The pseudocubic unit cell is outlined in black while the tetragonal unit cell is outlined in blue. The nearest neighbor Cu ion distance is 4.14 Å.

regarding the antiferromagnetic order.

X-ray absorption measurements (XAS) using the fluorescence yield technique were performed using F K edge and Cu $L_{3,2}$ edge x-rays. The beam angle with respect to the surface of the sample was 80° and the fluorescence takeoff angle was 30° for both measurements. The spectra obtained near the F K edge ≈ 696.7 eV displays pre-edge peaks at 684.5 eV and 689.8 eV, as shown in Figure 3.8a reminiscent of the "mobile carrier peaks" in $La_{2-x}Ba_xCuO_4$ XAS data reported in Reference [42]. Unfortunately, there are no reflections accessible

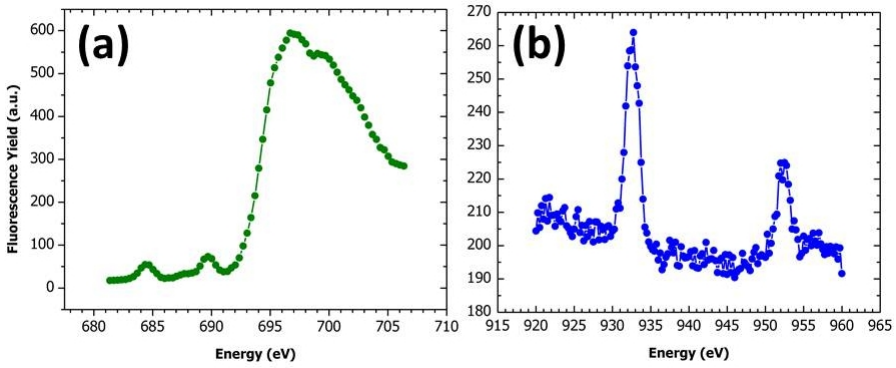

Figure 3.8: Fluorescence yield F K and Cu $L_{3,2}$ XAS data from $KCuF_3$. (a) Absorption features just below the F K edge at ≈ 697 eV can be seen at 684.5 eV and 689.8 eV. (b) The Cu L_3 and L_2 peaks can be seen in the FY XAS data.

within the range of available transfer momentum at F K edge energies, so we cannot explore the momentum dependence of the electronic structure displayed here. Cu $L_{3,2}$ XAS data is displayed in Figure 3.8b. The spectra is consistent

with the presence of only Cu^{2+} ions in the system. The peak of the Cu L_3 peak was set as 932.7 eV for all XAS and scattering measurements done near this range of energy.

The only reflection from $KCuF_3$ accessible near the Cu $L_{3,2}$ edges is the one associated with its magnetic order: (0, 0, 1). In this region of reciprocal space, just above the Néel transition, critical fluctuations of the magnetic order parameter can be observed, as shown in Figure 3.9. Using 932.7 eV x-rays,

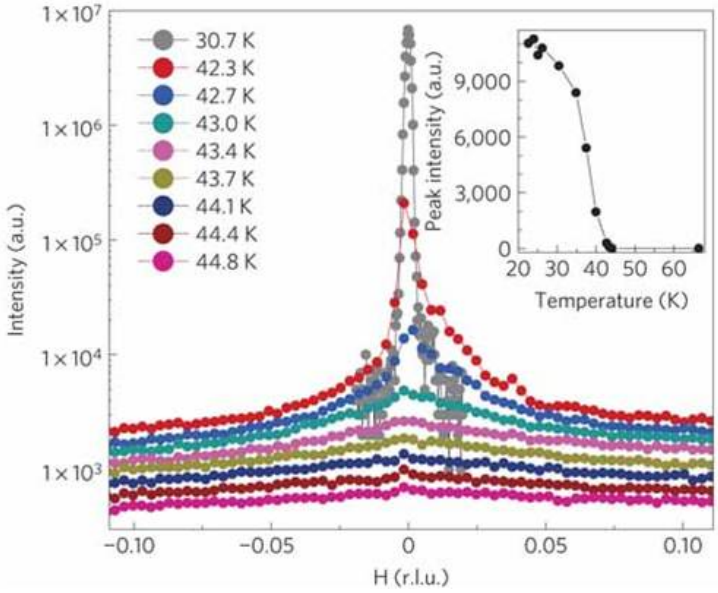

Figure 3.9: Resonant scattering at the Cu L_3 edge of the (0, 0, 1) reflection, which is an order parameter for A-type antiferromagnetism. Critical magnetic fluctuations, visible above T_N, reveal highly anisotropic spin correlations in the fluctuating regime. Inset: Temperature dependence of the magnetic order parameter below T_N. Taken from Reference [39].

line scans along the H direction in reciprocal space were made through (0, 0, 1) as the sample temperature was lowered from 44.8 K to 30.7 K. At 44.8 K, there is no peak and negligible diffuse scattering. As the sample is cooled broad profile, low intensity scattering arises, centered on H = 0. As the sample is cooled down further, diffuse scattering takes on a peak-like form that is still quite broad compared to the Bragg peak observed below T_N, at 30.7 K, which has a resolution limited line width and is orders of magnitude more intense than the diffuse scattering. This data is consistent with neutron scattering data from Sajita et al [33], which observed critical magnetic fluctuations. As for as the author knows, this is the first report of critical magnetic fluctuations being measured with the resonant soft x-ray scattering technique.

The momentum line width of the diffuse scattering is highly anisotropic, as shown in Figure 3.10. The line widths were measured using scans along the H and L directions through the diffuse scattering and fitting the profiles with Gaussians to obtain the full width at half maximum (FWHM) of the diffuse

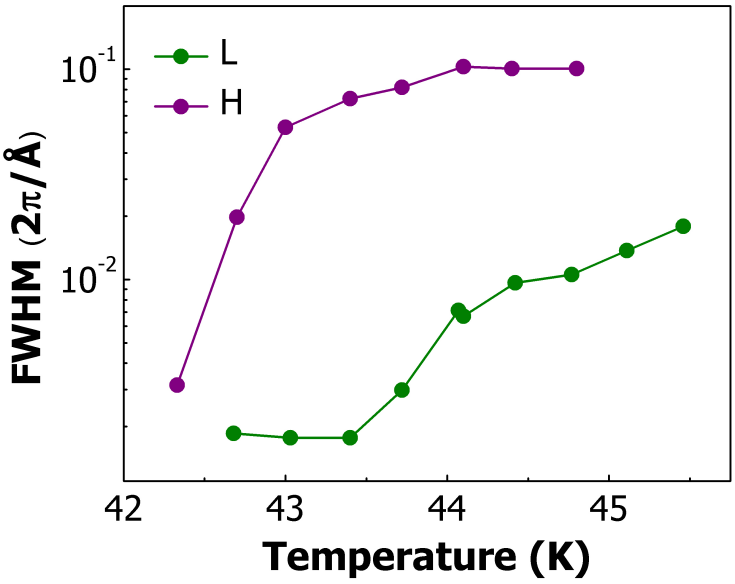

Figure 3.10: The temperature dependence of the line width of the (0, 0, 1) magnetic Bragg peak at the Cu L_3 edge, measured in scans through (0, 0, 1) along H and L directions in reciprocal space.

scattering. The FWHM is inversely proportional to the magnetic order correlation lengths crystallographic directions corresponding to the H and L directions. Line widths along H and L differ by an order of magnitude, with the L-direction line width narrower than in the in-plane line width. L-direction line width measurements become resolution limited below 43.5 K, so the evolution of the L-direction line width cannot be further examined below that temperature. The differences in magnetic order line widths along the in-plane and c-axis directions is consistent with other observations of anisotropic spin exchange in $KCuF_3$.

The resolution-limited (0, 0, 1) peak emerges from the diffuse scattering as the temperature falls below 40 K, as shown in the inset to Figure 3.9. Attempts to fit the peak intensity versus temperature plot with a power law relation of the form $(1-\frac{T}{T_N})^{2\beta}$ yielded fits with 40.3 K $\leq T_N \leq$ 41.6 K, a range consistent with other measurements. The critical exponent β falls in the range of $0.312 \leq \beta \leq 0.376$. One such fit, parameterized by $T_N = 40.3$ K and $\beta = 0.312$, is shown in Figure 3.11. Compared to similar power law fits performed by Tennant et al [43], which found that $\beta = 0.184$, our results indicate that the magnetism is similar to the 3D Heisenberg model, β =0.367. [43] This is puzzling, since the (0, 0, 1) line width supports the notion that the magnetic order is strongly one-dimensional in character. One cause may be improper data normalization between $T \leq T_N$ and $T \geq T_N$ scattering data. Close to T_N the magnetic scattering intensity increases very rapidly as a function of temperature. Given the limited dynamic range of the x-ray detector, the exit slit was narrowed to decrease the incident flux on the sample, thereby decreasing the scattered intensity and protecting the detector. As a result, measurements $T \leq T_N$ are obtained with very different exit slit

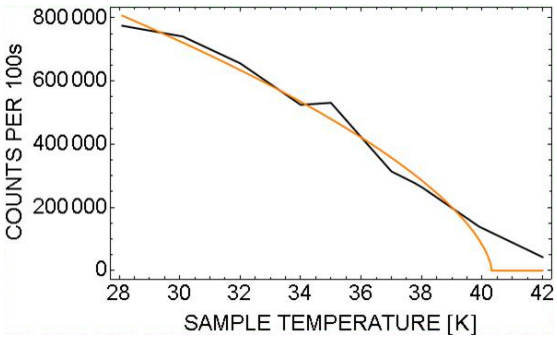

Figure 3.11: The temperature dependence of the (0, 0, 1) magnetic Bragg peak intensity at the Cu L_3 edge (black line), is fit by a power law of the form $(1 - \frac{T}{T_N})^{2\beta}$ (yellow line). The fit displayed is parameterized by $T_N = 40.3$ K and $\beta = 0.312$.

settings compared to $T \geq T_N$ measurements. This makes direct comparison of absolute intensities difficult. Data taken at a few common temperatures were used to normalize the data set. However, this may not have been done correctly and the long tail for $T > 40K$ of the peak intensity may be the result. A less prosaic possibility is that the normalization between the high and low temperature data was properly done and the transition really is smeared out, possibly due to the presence of disconnected spin ordered pockets with very short correlation lengths, as might occur in the presence of disorder.

Incidentally, this data also confirms that our samples are mostly of structural polytype A, since it exhibits a $T_N \approx 40$ K while the other likely variant, polytype D, has $T_N \approx 22K$. [32]

When in the Néel state, fixed Q energy scans of (0, 0, 1) show a single peak near the Cu L_3 edge, with no obvious shoulders or complicated multiplet structure, as seen in Figure 3.12. This is expected because Cu^{2+} has no multiplet structure, the final state being d^{10}. This remains the case across all temperatures at which the system was observed: 22.6 K $\leq T \leq$ 43.4 K.

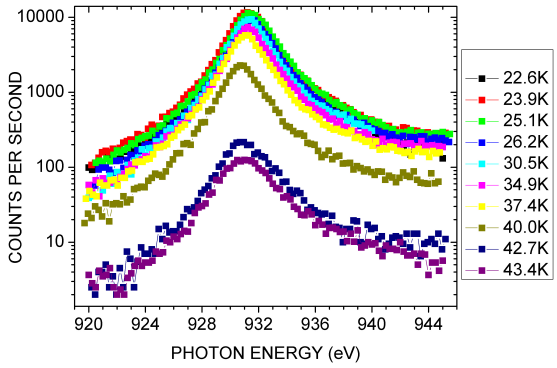

Figure 3.12: Fixed Q energy scans of the (0, 0, 1) magnetic Bragg peak intensity at several different sample temperatures.

A study of the energy and temperature dependence of the critical magnetic fluctuations was also done, in particular the correlations along the c-axis. This required collecting a mesh of data at many beam energies and L positions. In order to expeditiously collect such L versus E meshes, the diffractometer was aligned to (0, 0, L), for many positions around L = 1, at a reference energy E_{index} = 932.7 eV. Then, fixing the diffractometer angles, the beam energy was scanned. The principle behind this method is that the location observed in reciprocal space changes as a known function of energy. Given the scattering geometry, the change is along the (0, 0, L) direction. Bragg's law links the L position in reciprocal space with the beam energy E: $\frac{L}{2c} = \frac{2}{\lambda(E)} sin(\frac{TwoTheta}{2})$, where λ is the x-ray wavelength. From Bragg's law, the following relationship can be obtained:

$$L_{true} \frac{E_{index}}{E_{true}} = L_{index}, \tag{3.2}$$

where L_{index} is the L position the diffractometer was aligned to at E_{index}, and L_{true} and E_{true} are the actual L values for each energy in the scan. The fixed diffractometer energy scan traces straight line paths in reciprocal space along (0, 0, L) as a function of E, as shown in Figure 3.13. Energy scans at each E_{index}

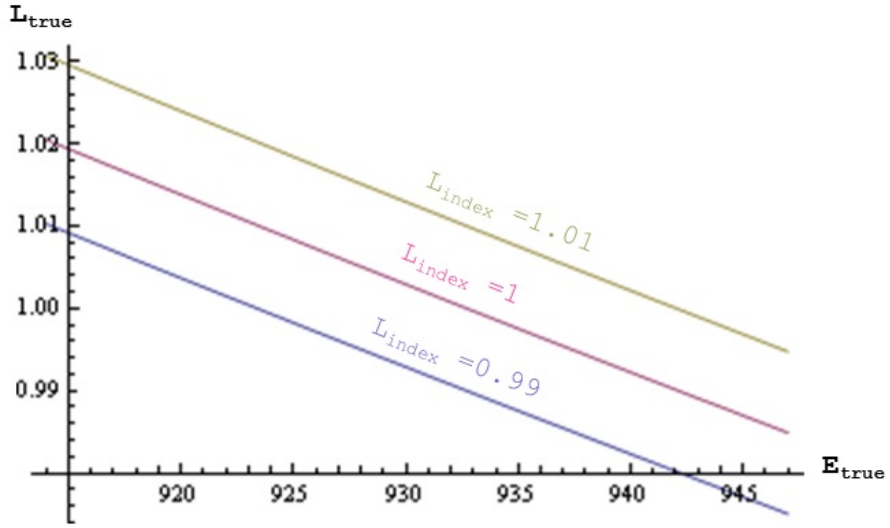

Figure 3.13: Straight line paths in reciprocal space of the scans described by Equation 3.2 for three different L_{index}.

and L_{index} for a given sample temperature were combined into single data sets. Using Eq. 3.2 and linear interpolation, a regular grid of points were generated from the data and plotted, as shown in Figure 3.14. The steps in the energy scans were ΔE = 0.33 eV, and ΔL_{index} = 0.001 typically, though ΔL_{index} = 0.00186 for data obtained at 43.2 K. Observation times per data point were 3 or 4 seconds.

The data shows that the magnetic scattering is concentrated along a rod centered on L = 1.000, with the scattered intensity highest around 930-935 eV.

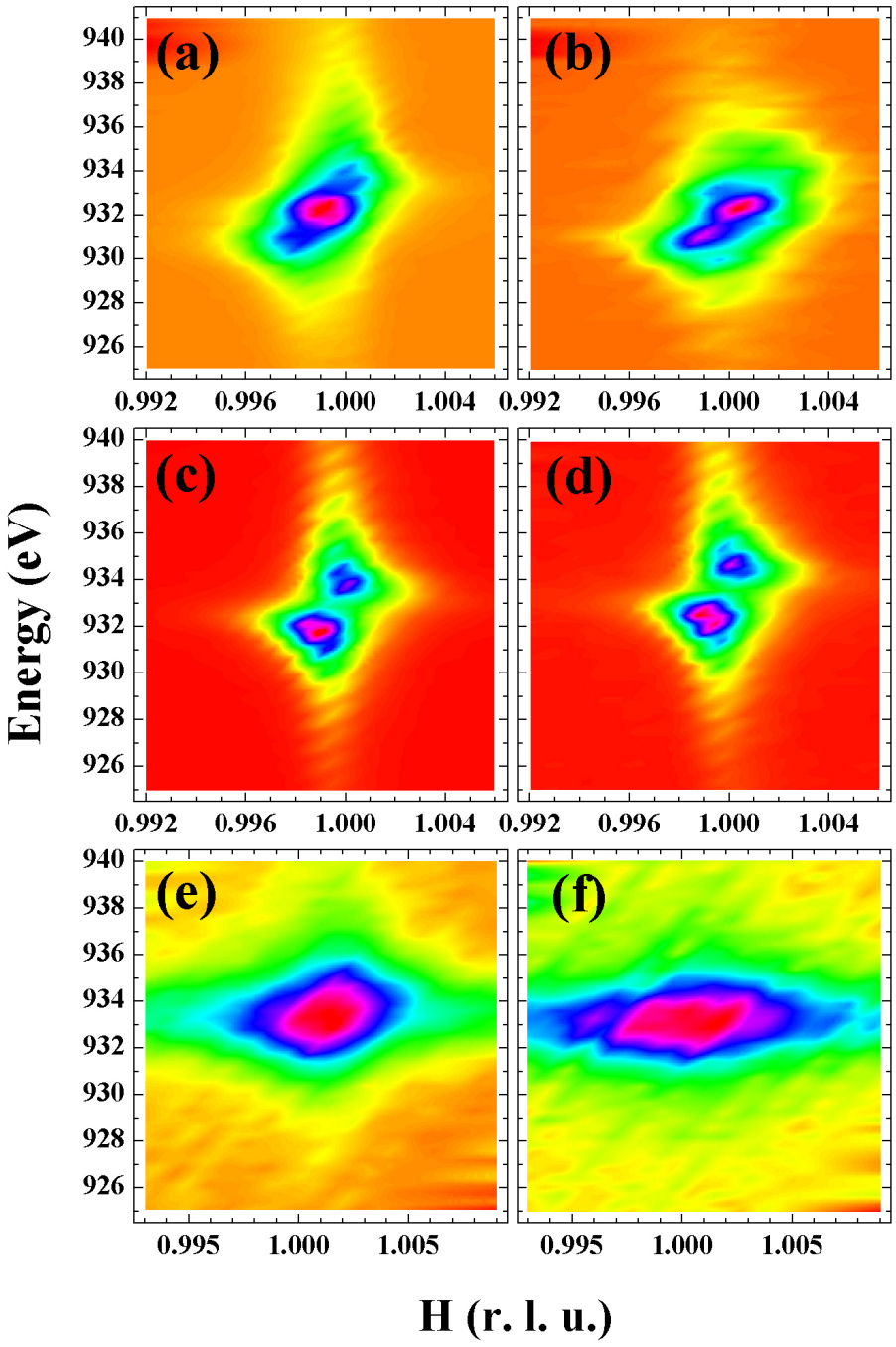

Figure 3.14: Representative L versus E meshes near (0, 0, L) and the Cu L_3 transition edge. These meshes were obtained at several different sample temperatures: (a) T = 42.0 K; (b) T = 42.3 K; (c) T = 42.7 K; (d) T = 43.0 K; (e) T = 43.4 K; and (f) T = 43.7 K. Color denotes scattering intensity, with red and yellow on the low count rate end, and blue and violet on the high count rate end. "(r. l. u.)" stands for "reciprocal lattice units".

As the temperature of the sample is warmed from 42.0 K to 44.8 K, the rod of magnetic diffuse scattering around (0, 0, 1) gradually fades away as T →

44.8 K. As the signal from the magnetic scattering gets weaker with increasing temperature, the exit slit was gradually opened to increase the incident flux. This results in a lower beam energy resolution and results in an increase in the fluorescence signal relative to the coherent scattering. In the figure, the fluorescence signal takes the form of a band of intensity centered on 932.7 eV. For data at T $>$ 43.4 K, fluorescence completely dominates the coherent magnetic scattering, which cannot be discerned from the background.

There appears to be a periodic structure in the scattering intensity, which is particularly pronounced in the tails leading from L = 1 in Figures 3.14c and 3.14d, shaded yellow in the contour plots. These are artifacts: a modulation of the incident beam intensity that was not seen before or since at X1B. We believe it may be due to the operation of a then-newly commissioned superconducting wiggler a few beam lines down, but we cannot be sure.

In terms of learning more about the energy and temperature dependence of the critical magnetic fluctuations, these scans turned up not much more information than was in the fixed Q energy scans of (0, 0, 1) shown in Figure 3.12. The resonant critical magnetic scattering peaks at one area in reciprocal space; no satellite peaks distinct from the (0, 0, 1) appear at different L or beam energy, so we detect no further modulation of the magnetic order beside that induced by A-type antiferromagnetism.

This data is interesting for quite different reasons than those for which we initiated these studies. Below T = 43.7 K, the diffuse scattering does not form one well defined peak near (0, 0, 1); instead, it appears to split into two peaks around E = 932.7 eV. This is an optical effect: due to the resonant enhancement of the scattering near the Cu L_3 transition edge, the Born approximation discussed in the Methods chapter is no longer valid and the effect of the scattered field from neighboring electrons must be taken in to account when solving for how the scattered beam propagates through the sample. The index of refraction displays a strong energy dependence as the beam energy is scanned through the Cu L_3 transition edge. The resulting change in refraction alters the direction of the beam. This has the effect of shifting the peak positions in scattering: looking along the direction of increasing energy, the peak shifts from L $\approx$ 0.9995 to L $\approx$ 1.001 as some characteristic energy is crossed. This effect is most prominent in Figures 3.14b (T = 42.3 K) to 3.14d (43.0 K) which clearly show two peaks with a dip in intensity around 932 eV. The presence of the 932 eV intensity dip is due to increased absorption from the increased magnitude of the imaginary part of the scattering amplitude, $f_2(\omega)$. In principle, with a more careful measurement, the index of refraction can be determined at each energy.

We now turn from resonant soft x-ray scattering and measurements of the valence band density of states, to non-resonant hard x-ray scattering which probes the electron density. These measurements were performed to explore the behavior of the higher-momentum Fourier components of the lattice and are complementary to the Raman scattering study by Shi Yuan. We find that the

instability of the lattice, as displayed by the softening of the Raman modes, is evident in the scattering data from the forbidden Bragg peak (1, 0, 5). This peak arises from structural distortions due to the Jahn-Teller distortion and $GdFeO_3$ octahedral tilts. For the sake of comparison, this reflection would be denoted as (1, 1, 5) using the coordinate system of Paolasini et al. Like their (3, 3, 1) reflection, the intensity of (1, 0, 5) is a measure of the Jahn-Teller structural distortion, which is the underlying phenomenon that gives rise to orbital ordering. With 8.8 keV x-rays, line scans in the K direction through (1, 0, 5) were made at several different sample temperatures, as shown in Figure 3.15 At T = 249 K, (1, 0, 5) is a well defined peak. As the sample is cooled to 99.8 K,

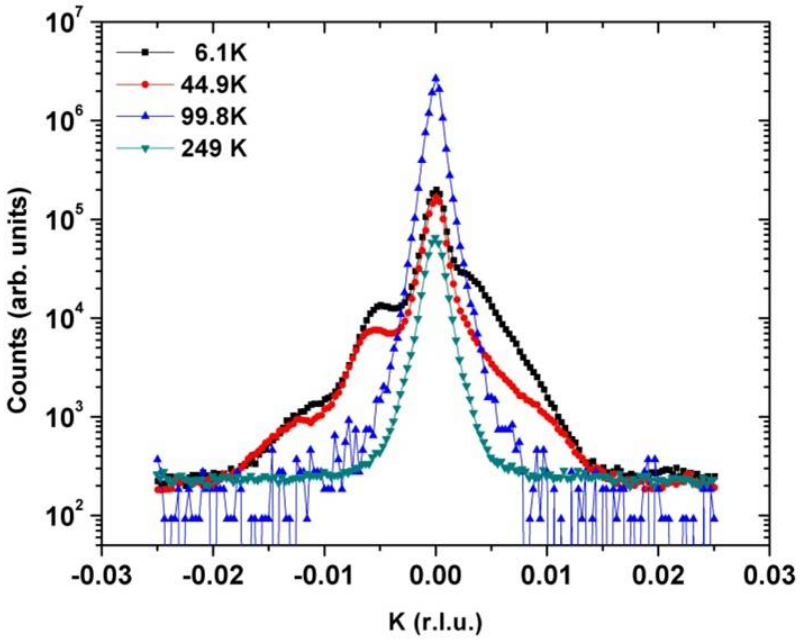

Figure 3.15: Line scans along the (0, K, 0) direction through the weak Bragg peak (1, 0, 5) at several different sample temperatures. (1, 0, 5) reflection occurs because of the the Jahn-Teller distortion of the lattice and, for T $\leq$ 50 K, the $GdFeO_3$ octahedral tilts.

the peak remains well defined but, surprisingly, its intensity increased by more than an order of magnitude. Note that this is the middle of the temperature range in which the Raman modes display their anomalous softening. Below T = 50 K, the temperature at which the higher energy E_g mode split, the intensity of (1, 0, 5) decreases dramatically and the peak develops diffuse side bands. The shape of the side bands evolves and side band intensity increases as the sample is cooled. Diffuse scattering develops in all directions in reciprocal space, displaying structure in the HK and HL planes, as shown in reciprocal space mesh

scans made at a sample temperature of 6 K and shown in Figures 3.16 and 3.17.

The development of these side bands indicates that the long-range order of

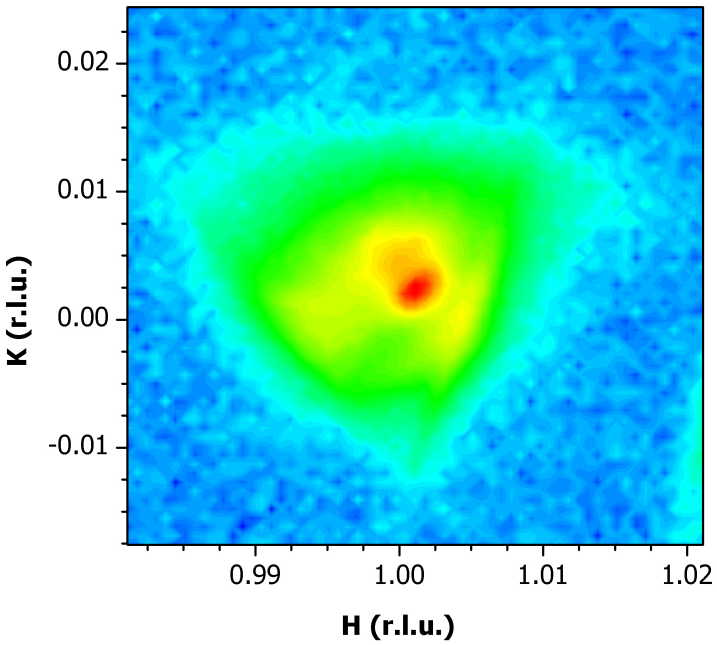

Figure 3.16: Reciprocal space mesh scan in the HK plane intersecting the (1, 0, 5) reflection. Blue tones denote low intensity and red high intensity. Diffuse scattering around (1, 0, 5) is visible. There is also fine structure in the diffuse scattering, corresponding to the side bands seen in the K line scan of Figure 3.15. The sample temperature was 6 K.

the cooperative Jahn-Teller distortions is absent and small domains of coherent distortions are forming instead.

It was also noticed that the shape of the side bands around (1, 0, 5) is not reversible as the temperature of the sample is cycled through 50 K. Fixing a sample temperature of 40 K as our point of comparison, we observed that the diffuse sidebands did not overlap with thermal cycling: the same line scan taken after cooling was different from the same line scan after warming to the same temperature. This irreversibility in the shape of the diffuse scattering indicates that the details of the structure depend on the thermal history of the system. This is characteristic of glassy structural disorder, which sets in when the lattice undergoes a tetragonal to orthorhombic transition at ≈ 50 K.

Our data indicates that the structure plays a critical role in the magnetic order in $KCuF_3$. Unlike the K-K model, which is based on the assumption that there is one stable tetragonal structural phase below T_{OO}, our data shows that the lattice is only tetragonal on average, undergoing critical orthorhombic fluctuations over a wide range of temperatures: ≈ 50 K to 250 K, and presumably to much higher temperatures. Reasoning along the lines of the OOA, this should

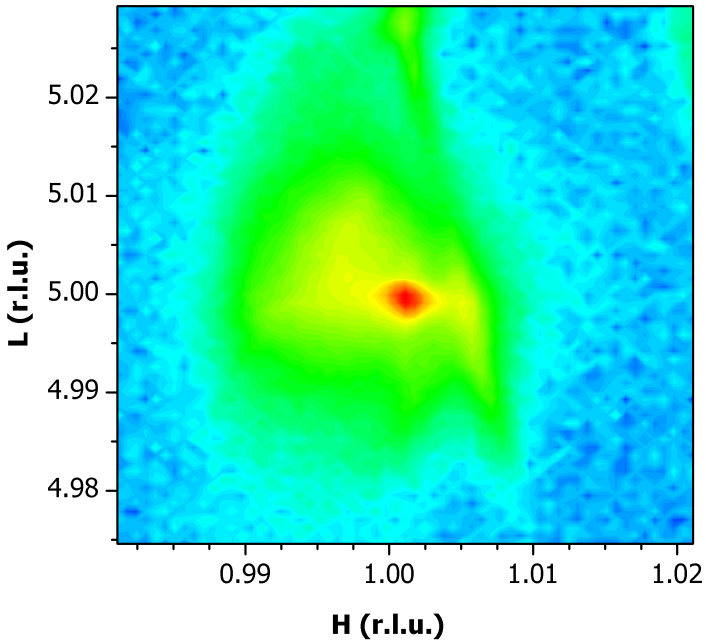

Figure 3.17: Reciprocal space mesh scan in the HL plane intersecting the (1, 0, 5) reflection. Blue tones denote low intensity and red high intensity. Diffuse scattering and small ill-defined peaks around (1, 0, 5) are visible. The sample temperature was 6 K.

manifest itself as a fluctuation of orbital order over this range of temperatures. The lattice fluctuations stabilize at ≈ 50 K, when a structural distortion lowers the point group of the lattice from tetragonal to orthorhombic, conceivably by undergoing $GdFeO_3$-like octahedral tilts. This is consistent with the results of Paolasini et al, which shows an increase in intensity of the (3, 3, 1) Bragg peak (or (3, 0, 1) if classified in our coordinate system) at 43 K, which is not just a measure of the orbital order but also of the orthorhombic distortions. The intensity of the reflection stabilizes at the Néel temperature. Our 8.8 keV x-ray scattering data show that the lattice stabilizes into a glassy quasi-ordered state, characterized by short range ordered orthorhombic distortions due to $GdFeO_3$-like octahedral tilts. In an OOA treatment like the K-K model, the orbital order should display glassy disorder. This immediately raises the question of how that affects the electron spin ordering.

The simplifications of the OOA led the K-K model to gloss over the effect of the structure on the orbital ordering and, thus, the magnetic ordering. In particular, by mapping the ligands out of the physical model and account for their influence only through the pseudospin exchange parameters, orbital ordering models lose the ability to take into account distortions of the ligand ions away from ideal crystallographic directions. However, by reintroducing the ligands—

and explicit consideration of the normal modes of the lattice—one risks losing the simplicity of the OOA. At least in the case of $KCuF_3$, taking account of the orthorhombic distortions of the ligands can be made in a Kugel-Khomskii-like model.

3.2.2 A Modified Kugel-Khomskii Model

With the two new pieces found in our x-ray and Raman scattering experiments, we will see if we can fill in the theoretical gaps remaining in the $KCuF_3$ orbital order puzzle.

The main effort in this regard was made by Siddhartha Lal, who introduced new theoretical concepts to the K-K model so that it might account for the experimental data. Lal culled new ideas from two different sources: L. F. Feiner et al [44], whose work dealt addressed the stability of long-range classical spin order against quantum fluctuations of orbital order; and the work of M. V. Mostovoy and D. I. Khomskii, [45] which studied the effects on orbital order due to electron-lattice interactions and holes occupying neighboring ligands in charge transfer insulators.

The mathematics of the K-K model is stated in Equation 2 of Reference [39]. The K-K model has two important sets of effective parameters: the superexchange parameters between spins on neighboring sites, called J_2; and the Hund's rule coupling, controlled using $\eta = J_H/U$. To this, the nucleus of the K-K model, a direct orbital-orbital exchange term is added:

$$H_{\tau\tau} = \sum_{\langle i,j \rangle} \sum_{\alpha=a,b,c} J_1^\alpha \tau_i^\alpha \tau_j^\alpha \tag{3.3}$$

This term takes direct account of Jahn-Teller distortions and their effect on the orbital occupation. To do this, J_1 is set to be much larger than the K-K orbital-spin superexchange J_2, thereby becoming the dominant interaction. The τ are the pseudospin operators of each site, and the α index denotes whether it is represented by the x, y, or z Pauli matrix. As in the K-K model, interactions are confined to nearest neighbor sites. This term also takes into account what Mostovoy and Khomskii called an "orbital Casimir effect", or the favoring of orbital ordering in charge transfer insulators that directs the orbital wave functions away from shared ligands if those ligands are occupied by holes. [45]

Additionally, Siddhartha Lal formulated an electron-lattice coupling term that directly accounts for the effect of $GdFeO_3$-like distortions on spin and orbital order:

$$H_{OR} = -\mu \sum_{\langle i,j \rangle} \sum_{\alpha=a,b} J_2^\alpha (\vec{S}_i \cdot \vec{S}) j) (\tau_i^\alpha - \frac{1}{2})(\tau_j^\alpha - \frac{1}{2}) |\vec{Q}_{ij}|^2 \tag{3.4}$$

In Equation 3.4, μ is the electron-lattice coupling, $J_2 \gg \mu$; $\vec{S}$ is the electron spin operator at a site; and $\vec{Q}_{ij}$ is the order parameter that tracks the distortion of

the apical F ion between site i and j transverse to the direct line between sites i and j. This type of distortion is characteristic of octahedral tilts and is consistent with reports that such distortions mediate the Dzyaloshinsky-Moriya interaction between sites along the c-axis. This term takes into account how much such a distortion affects the spin order in the a-b plane. Taking a cue from Paolasini et al, this term was also designed to directly couple the electron spin and orbital pseudospins. Since the octahedral fluctuations are not expected to energetically favor any particular direction in orbital- or spin-space, the term is symmetric under orbital and spin rotations. Further, reflecting the glassy disorder of the lattice, the energy cost of octahedral fluctuations associated with the apical F ion distortions is set to be the same regardless of the distortion direction: thus the term goes as $|Q|^2$. [39]

For computational convenience, a crystal-field splitting term was introduced: $H_{CF} = \lambda_{CF} \sum_i \tau_i^z$, with $\lambda_{CF} \ll J_1$ set as the smallest energy scale of the problem.

Just as Kugel and Khomskii solved their model, a variational ground state for the modified K-K model was obtained by applying an orbital ordering ansatz that predetermines the relationship of the orbital wave function, Equation 3.1, mixing angles θ between the sublattices of the system. θ is varied until the variational energy is minimized. The ansatz that produces the lowest overall energy is called the ground state. (Note: in our treatment, we use the form $sin(\theta)$ in Equation 3.1 instead of $sin(\theta/2)$ as Kanamori and Kugel and Khomskii did.)

As for the K-K model, the orbital order ansatz with θ alternating signs between nearest neighbor sites, consistent with antiferro-orbital order that $KCuF_3$ is known to have, are the lowest energy states. Surprisingly, the mixing angle of the ground state obtained ($\theta \approx \pi/4$) is quite different from that of the K-K solution ($\theta_{K-K} = \pi/6$). So, while the symmetry of the orbital order remains the same, the ground state orbital wave functions are quite different. Even more surprisingly, it was found that there are two nearly degenerate states with $\theta \approx \pi/4$. These states were labeled HO1, with $\theta \approx 0.244\pi$, and HO2, with $\theta \approx 0.256\pi$. Cartoon depictions of HO1 and HO2 can be found in Figure 3.18. Though HO1 and HO2 are both antiferro-orbital, the spin order in the a-b plane associated with them are markedly different. HO1 is characterized by antiferromagnetic electron spin order in the a-b plane, while HO2 displays ferromagnetic electron spin order in the a-b plane. The energy difference between the two states is

$$\Delta E = E_{HO1} - E_{HO2} \approx (\eta - \frac{1}{4}) J_2^{a/b} + \frac{\eta}{4} J_2^c + \frac{\mu}{16} |\vec{Q}|^2. \tag{3.5}$$

Note that HO2, the orbital ordering solution associated with ferromagnetism in the a-b plane, is the variational ground state. The energy of HO1 is greater, but it is separated in energy from HO2 by the smallest energy scales of the problem. In contrast, the K-K solution is of much larger energy, with $\Delta E \approx \frac{3}{8} J_1$, the

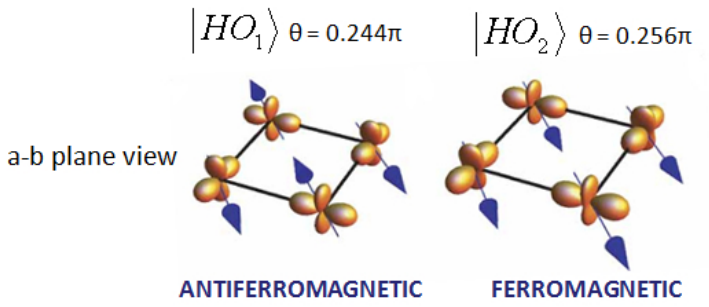

Figure 3.18: Depictions of the orbital ordering in the a-b plane of $KCuF_3$ for the two hybrid orbital solutions HO1 and HO2, as well as their a-b plane spin order: the electron spin directions are shown as blue arrows centered on the orbital sites. HO1 is characterized by a mixing angle of $\theta = 0.244\pi$; HO2 is characterized by a mixing angle of $\theta = 0.256\pi$. HO1 favors antiferromagnetic spin order in the a-b plane while HO2 favors ferromagnetic spin order in the a-b plane.

largest energy scale of the problem.

For reasonable choices of effective parameters ($J_1^a = 600K, J_1^c = 630K, J_2^c = 200K, J_2^{a/b} = 30K, \lambda_{CF} = 50K, \eta = 0.1$) $E_{HO1} - E_{HO2} \sim 3K$. The choices in effective parameters reflect the dominant role of J_1, due partly to lattice effects, as well as the larger anisotropy in J_2, as dictated by experiment.

The modifications to the K-K model fixes many of its problems, and a natural explanation for the extended lattice fluctuation regime found in the Raman data and the low temperature structural phase transition can now be made in terms of it. The consequences of the modified model are illustrated in Figure 3.19. In the high temperature regime (> 800 K), the spin and orbital exchange

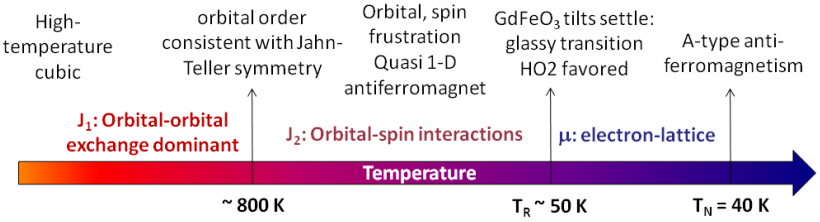

Figure 3.19: Important energy scales for the modifed Kugel-Khomskii model are marked along a temperature axis, with high temperature on the left side and low temperature on the right side.

terms, and the electron-lattice interactions are small compared to the thermal energy: the state of the system is that of an ideal cubic perovskite. As the system is cooled to ∼ 600 K, orbital-orbital exchange causes antiferro-orbital ordering, the ground state orbital wave function mixing angle becomes $\theta \approx \pi/4$. The system thermally occupies both HO1 and HO2 orbital states, leading to fluctuations in the orbital and spin ordering. Given the small difference in θ_{HO1} and θ_{HO2}, the orbital ordering fluctuations are small. The fluctuations

of the electronic spin order in the a-b plane, on the other hand, are significant since the system alternates between antiferromagnetic and ferromagnetic order in the a-b plane. Spin order in the a-b plane is, therefore, completely frustrated. This explains why an apparently stable orbital ordering sets in at temperatures (800 K $< T_{OO} <$ 500 K) so much greater than that of the electron spin order. In this temperature regime, $\vec{Q}$ is vanishing since orthorhombic distortions are thermally averaged and the system is, on average, tetragonal. As the system temperature approaches $\sim$ 50 K, fluctuations diminish and HO2 is increasingly favored, allowing ferromagnetic spin correlations in the a-b plane to stabilize.

The gradual development of in-plane spin correlations affects the lattice. As discussed in the on-line Supplementary Material to Reference [39], the effective spring constant of the lattice is:

$$K_{eff} \approx K - 2\mu\langle\vec{S}_i \cdot \vec{S}_j\rangle \sum_{\alpha=a,b} J_2^{\alpha}\langle(\tau_i^{\alpha} - \frac{1}{2})(\tau_j^{\alpha} - \frac{1}{2})\rangle. \tag{3.6}$$

As HO2 is stabilized and in-plane ferromagnetism sets in, the effective spring constants of the lattice decrease, which is consistent with the observed softening of the Raman modes.

When the system is cooled below $\sim$ 50 K, the orthorhombic $GdFeO_3$-like distortions undergo a critical slowdown and $|\vec{Q}|^2 \neq 0$. By Equation 3.5, the near degeneracy of HO1 and HO2 is further lifted and the energy of HO2 becomes decisively lower. Orbital fluctuations cease and in-plane ferromagnetic spin order stabilizes. By Equation 3.6, since the average spin and orbital products are stable against temperature, K_{eff} stops decreasing and the Raman mode softening ceases. Since $|\vec{Q}|^2 \neq 0$, the local crystal symmetry lowers from tetragonal and causes the higher energy E_g mode to split. The additional electron-lattice interaction expressed by Equation 3.4 is not sensitive to the direction of the octahedral distortion. Therefore, the system is allowed to form the glassy disordered state observed in the 8.8 keV x-ray scattering experiment, since many different octahedral tilt patterns are energetically degenerate.

The modifications made to the K-K model, Equations 3.3 and 3.4, which take into account electron-lattice effects and charge transfer effects (that may be relevant to $KCuF_3$), allow it to reproduce the essential features of the experimental data—lattice instability over a wide temperature range, a low temperature glassy structural distortion, antiferro-orbital order, and A-type antiferromagnetic order in the a-b plane.

3.3 Conclusions

In studying $KCuF_3$, it has been learned that direct orbital-orbital exchange terms, like Equation 3.3, may be essential to describing the physics of orbitally active systems. Its utility in explaining how the peculiar structural behavior of

$KCuF_3$ affects its electron spin order provides evidence that the orbital exchange mechanism proposed by Mostovoy and Khomskii is valid. This result can have a wider impact on other orbitally active systems. One such system may be $LaMnO_3$, the parent compound of the colossal magnetoresistance manganites: it has one electron in the e_g manifold, in analogy to $KCuF_3$ which has one hole in that manifold. Similar orbital-orbital exchange effects will be relevant to the physics of $LaMnO_3$.[45]

The other lesson learned is that, in Jahn-Teller systems, low symmetry phonons may significantly alter orbital-spin interactions. The OOA sweeps the effects of ligand ions into orbital exchange parameters. This has the effect of artificially raising the symmetry of the system, since the only interacting entities are the orbitals on metal sites. [29] This leaves OOA approaches blind to the effect of certain low symmetry phonons, such as the $GdFeO_3$-like octahedral tilts. As these octahedral distortions are common in perovskites, including the orbitally active perovskites, they will have to be explicitly considered. Doing so may spoil the simplicity introduced by the OOA, but we have been able to demonstrate, at least in the case of $KCuF_3$, that incorporating the effect of lattice distortions on orbital ordering can be relatively painless and that it is possible to extend OOA approaches to account for low symmetry phonons.

4 Stripe-like Domain Structures in $BiFeO_3$ Epitaxial Thin Films

This section describes the state of on-going efforts to study the structural and electronic properties of (001)-oriented $BiFeO_3$ epitaxial thin films that exhibit arrays of stripe-like domains separated by 109° and 71° domain walls.

The domain structure of these thin films has been characterized using Cu K_α x-ray diffraction. Based on the data collected, simple charge density models of the domain structure have been formulated that agree with the data in a satisfactory way.

Resonant soft x-ray scattering measurements have also been made of the 109° domain wall systems. Resonant scattering near the Fe L_3 transition edge has revealed a spatial modulation of the Fe 3d valence density of states. The period of the Fe 3d valence state modulation follows that of the underlying ferroelectric domain structure. Scattering associated with the ferroelectric domain structure has also been seen near the O K transition edge and the results of that study are discussed as well.

This chapter concludes with some remarks regarding the future course of this research.

4.1 Properties of $BiFeO_3$: Bulk and Epitaxial Thin Film Systems

The electronic properties of the surfaces of materials, and interfaces between different materials, can be very different from those of the bulk. Perhaps the most common example of this is the MOSFET, which is a metal-semiconductor heterostructure with an oxide layer in between. The application of a transverse voltage using the metal "gate" can cause charge carriers to accumulate at the oxide interface. These devices form the backbone of all modern electronics, thus demonstrating how important being able to control the electronic properties of materials at their interfaces is for modern society. There is much that is not known about the physics of the interface, placing it at the frontier of science. Similar semiconductor heterostructures can cause the formation of a two-dimensional electron gas at the oxide interface. Under quantum conditions ($T \sim 1$ K, $B \sim 17$ T), the two-dimensional electron gas can be made to exhibit quantized Hall resistances, in either integer or fractional units of e^2/h. The origins of this effect are intimately related to concepts of topology and localization. [46]

A reason why such novel properties arise at interfaces is due to the fact that the interface is missing symmetries that would be present in the bulk. Atomic sites near the interface no longer are surrounded by an infinite environment of identical and repeating sites. At the interface, the arrangement of atoms can reconstruct itself in a way that makes it very different from the bulk structure. Chemical bonds with neighboring atoms and the ionic potential the sites experience are also changed. One should expect that the band structure near the interface should be different from that of the bulk. For complex oxide systems, like $BiFeO_3$, these changes can be significant since they exhibit narrow bands; slight changes to the structure or chemistry can cause shifts in bands energy that are large compared to their bandwidths. Radical changes to the electronic properties of the interface can therefore occur. [47]

Strong correlation effects can also create states at the interface that the bulk system cannot manifest. Parameters such as the on-site repulsion parameter U and intersite spin exchange J are very important in characterizing strongly correlated systems. At the interface, U and J can attain values that they cannot in the bulk, thereby allowing the nucleation of new ground states in the phase diagram of the system. [47] This can be seen in $LaTiO_3/SrTiO_3$ heterostructures. [48] These systems are superlattices of materials that are, in their bulk forms, band and Mott insulators. Their interfaces, however, can be metallic but only if the $LaTiO_3$ layers in the superlattice are at least five unit cells thick. The underlying reason is the fact that charge density from $LaTiO_3$ layers diffuses to neighboring $SrTiO_3$ layers, [49] which can change the magnetic and orbital order near the interface. This effect is often called "electronic reconstruction", in analogy to the relaxation of top-layer atoms at the surfaces of crystals.

A similar effect occurs in the domain walls of $BiFeO_3$ (BFO) epitaxial thin films, which can exhibit electronic properties very different from bulk BFO or the bulk-like domains separated by the domain walls (DWs).

In the bulk, BFO exhibits multiferroic behavior, or coexisting ferroelectric and ferromagnetic order. There are very few materials in which these order parameters coexist, and fewer yet that exhibit these properties at or above room temperature, as BFO does. [50] The bulk BFO Curie temperature is $T_C \approx 820°$ C. The bulk is also known to exhibit a metal-insulator transition at $T_{MI} \approx 933°$ C, below which it is an electrical insulator. [51]

There are significant differences between the bulk system and epitaxial thin films of BFO. For one, large ferroelectric moments, as BFO was predicted to have, did not appear in bulk systems in early attempts to synthesize the compound. It was only in epitaxial thin films that the large remnant ferroelectric polarization $P \sim 90\ \mu C/cm^2$ was first stabilized. [52] A large reason for this is the influence epitaxial strain in the BFO film, caused by the BFO relaxing to accommodate the slightly different atomic lattice of the substrate. [50]

Epitaxial strain can also induce structural changes to the film, such as the

formation of domain walls between ferroelectric bulk-like domains. There are three types of domain walls: 71°, 109°, and 180°. These labels are based on how the ferroelectric moment changes direction from one domain to the next, which can be described as a rotation, as illustrated in Figure 4.1.

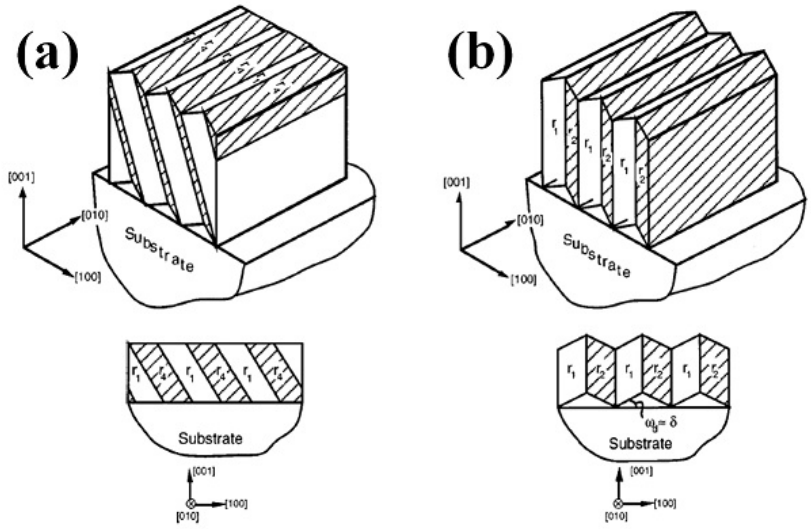

Figure 4.1: (a) Shaded and unshaded ferroelectric domains, the polarization moments of which are rotated by 71° with respect to each other, are separated by domain walls that are tilted by 45° with respect to the substrate surface normal. Notice that the surface of this 71° domain wall film is flat. (b) Shaded and unshaded ferroelectric domains, with polarization moments that differ in direction by rotations of 109°. These 109° domain walls are oriented normal to the substrate surface. Note that the top surface of this film exhibits puckering. From Reference [57].

The DWs exhibit fascinating electronic properties: the electrical conductivity of 109° and 180° DWs are orders of magnitude greater than that of the bulk-like domains. Curiously, the 71° DWs do not exhibit a similar giant electrical conductivity increase. These observations were first made by Seidel et al [53] using conducting atomic force microscopy (AFM). Some of the data they obtained is illustrated in Figure 4.2. Using a conductive AFM probe tip, they "wrote" in DWs of all three types into a (110)-oriented BFO thin film on a $SrTiO_3$ substrate. They then used the same conductive tip to probe the electrical conductivity of the DWs and found that the 109° and 180° DWs are $\sim 10^5 - 10^6$ times more electrically conductive than 71° DWs, which exhibited conductivities similar to the domains.

The mechanism for this difference in conductivity is unclear. One possibility is that the band gap closes at the DWs. LDA calculations by Seidel et al, however, found that the band gap closes by only $\sim 5-10\%$. Another mechanism might be charge carrier accumulation at the DWs. Since the surface charge density associated with such a moment is $\sim \vec{P} \cdot \hat{n}$, where $\hat{n}$ is the vector normal to the domain wall, the component of $\vec{P}$ normal to the wall (P_{norm}) must be

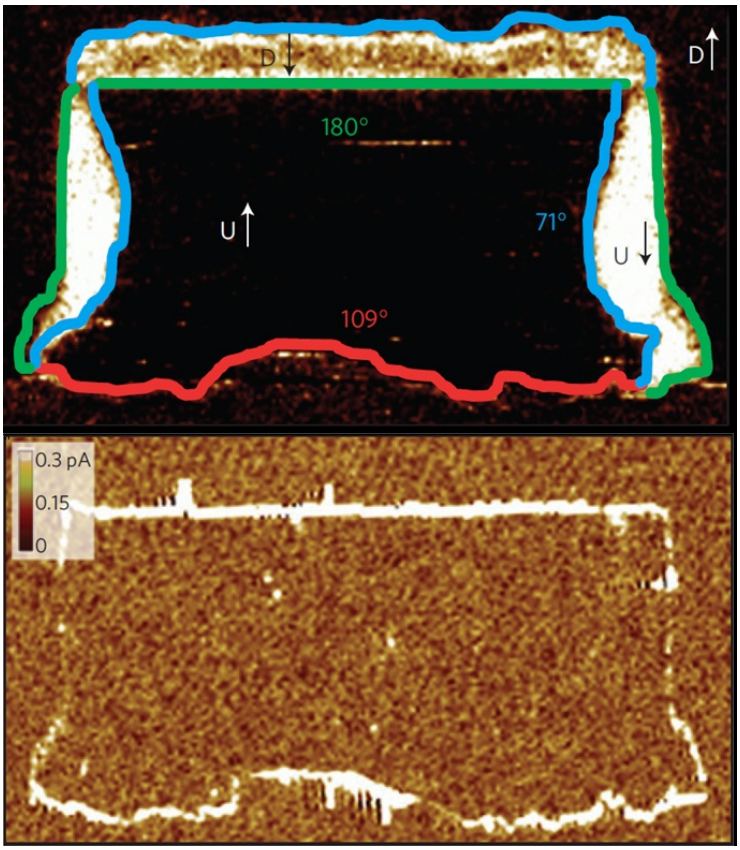

Figure 4.2: 71°, 109°, and 180° DWs are "written" into a (1, 1, 1) oriented film of BFO using a conductive AFM tip. The location of the domain walls and their types are shown in the top panel: 71° DWs are blue, 109° DWs are red, and 180° are green. The bottom panel shows a spatial electrical current map of the film surface. High currents are light colored and low currents are dark colored. Notice that the areas where the 109° and 180° DWs are present show enhanced conductivity. From Reference [53].

discontinuous for charge carriers to accumulate. Seidel et al claim in Reference [53] to see in transmission electron microscopy scans of 109° DWs changes in the atomic structure consistent with a discontinuous P_{norm} at the wall, but no such changes in 71° DWs. However, the size of the lattice distortions at the 109° DWs in the measurement by Seidel et al was on order of the instrument noise. Further, their own spatial conductivity map casts doubt on this. In Figure 4.2, there are segments of DWs labeled as 109° and 180° types where P_{norm} is continuous and segments of 71° walls where P_{norm} is discontinuous.

There are no insights to be gained from existing work on the bulk electronic structure of BFO, as that is poorly understood. For example, LDA band structure calculations by Neaton et al [54] were performed on BFO. The resulting band structure did not exhibit a band gap, whereas the bulk system is known to be an electrical insulator. To obtain a band gap in their calculation, an on-site repulsion U had to be introduced, which was tuned to get the band gap size

correct. This illustrates that there is no first-principles understanding of why BFO is an electrical insulator.

What is the mechanism of DW electrical conductivity in BFO epitaxial thin films? How is it related to the low temperature insulating phase and the structure of BFO epitaxial thin films near its domain walls?

Before we address these questions, we should first review some of the relevant properties of the bulk system, to gather clues as to why this is happening.

As mentioned, BFO exhibits a metal-insulator transition at $T_{MI} \approx 933°$ C. There is an accompanying structural phase transition at this temperature. According to a neutron study by Arnold et al, [55] above the transition the system is a cubic perovskite, and presumably metallic. Below the transition, the structural symmetry becomes less-than-cubic and insulating, with Arnold et al reporting an orthorhombic structure. This is an indication of a structurally driven band gap formation.

As the temperature is lowered, ferroelectricity manifests at $T_C \approx 830°$ C. This is due to a shift of the Fe and O sublattices in BFO with respect to the Bi sublattice, creating a permanent electrical dipole moment in the sample. This shift occurs because highly electrically polarizable Bi $6s^2$ "lone pair" electrons hybridize with the O 2p orbitals. This makes the structure unstable to distortions along the cubic $\langle 111 \rangle$ directions. The distorted lattice can be obtained from the cubic system by shifting the Fe ions along the [111] (or equivalent) direction; the corners of the cubic unit cell are stretched along that direction as well, resulting in shifts of the Bi ions as well. Due to these distortions, the angles between the a, b, and c lattice vectors are no longer 90° but each of the interaxial angles are equally slightly smaller than 90°. The O octahedra surrounding the Fe ion also distorts, such that three Fe-O distances are made shorter than the other three. [51] This distortion lowers the lattice space group to rhombohedral R3m. [56]

Due to the smallness of the unit cell distortions away from the cubic ideal, it is customary to refer to the crystal features such as crystallographic plane and directions using "pseudocubic" indexing, which is explained in Reference [57]. For the rest of this chapter, we will use pseudocubic indexing.

Spins in BFO are arranged in a G-type antiferromagnetic order, which sets in at $T_N \approx 370°$ C. The lattice distorts again on the onset of the Néel state, with the O octahedra now rotating about [111] by $\approx 13°$. Octahedra located on neighboring unit cells along the [111] vector also rotate, but the sense of rotation is reversed between the two cells. Because the octahedra share corners, the rotations are coordinated throughout the entire crystal. [51] These distortions define the low temperature rhombohedral space group R3c. [56] This distorted unit cell is shown in Figure 4.3.

The antiferromagnetic spin order also displays spin canting. Since the oxygen octahedral rotations force the oxygen ions away from the local inversion centers between the Fe sites, [51] and due to the high symmetry about the cubic

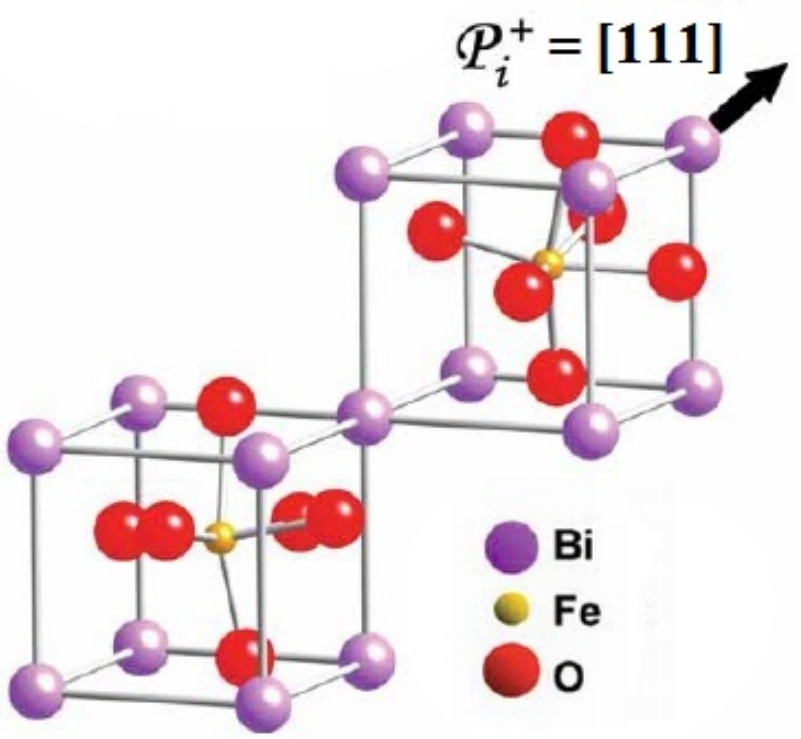

Figure 4.3: The distorted unit cell of BFO in its low temperature R3c symmetry. The Fe ions are shifted along the [111] direction, the direction of the polarization. The corners of the cubic unit cell are stretched along that direction as well, resulting in shifts of the Bi ions. The angles between the a, b, and c lattice vectors are no longer 90°. The O octahedra surrounding the Fe ion is distorted, such that three Fe-O distances are made shorter than the other three. Note that the O-octahedra are rotated about the [111] vector but the sense of their rotations are oppposite. From F. Zavaliche et al, Phase Transitions **79**, 991-1017 (2006).

[111], the Dzyaloshinsky-Moriya coupling vector $\vec{D}$ and the polarization $\vec{P}$ are collinear, which forces the polarization and the weak ferromagnetic moment $\vec{M}$ to be orthogonal. [56]. In the bulk, a macroscopic magnetization fails to form because the spins in neighboring cubic (111) planes are successively rotated with respect to each other. This results in the forming of a long wavelength ($\approx$ 620 Å) spin spiral that washes out the weak ferromagnetic moment. [56]

While many bulk properties are also found in epitaxial thin films, there are also significant differences between them. The first clear difference between is the strain induced on the BFO film by the substrate to create an epitaxial interface. As we have seen, the epitaxial strain has a significant effect on the ferroelectricity. It also, in many cases, destroys the spin spiral and stabilizes a small net magnetization of ~ 0.3 emu/g. [51] The thin film morphology can also differ quite markedly from that seen in the bulk. Anisotropic epitaxial strain can be used to induce the formation of bulk-like domains separated by specific

types of domain wall. Chu et al, [58] for instance, used the anisotropic strain introduced to BFO films by (110) oriented $DyScO_3$ substrates to create stripe-like formations of domains, separated by either 109° or 71° DWs, the type of which can be selected by manipulating the electrostatic boundary conditions.

The domain walls in BFO thin films are crystallographically distinct from the bulk-like portions of the films. In (001)-oriented films of BFO, the subject of this study, ferroelectric polarization must rotate between separate domains by either 71° or 109° in order to create coherent, low strain energy domain walls. These walls are confined to form on either the {101} or {100} crystallographic planes. [57] 109° DWs are oriented along {100} planes and they are normal to the substrate surface; 71° DWs are oriented along {101} planes that are tilted by 45° with respect to the substrate normal. The geometries of these DWs are illustrated in Figure 4.4. Since the way in which the ferroelectric moments change near DWs is constrained by the wall type, the magnitude and direction of the ferroelectric lattice distortions, especially those of the Fe and Bi sublattices, must be distinct for each type of domain wall. In this way, the lattice structures near different types of DW are distinct from each other and from the bulk-like domains, which must be the main reason why their electronic properties are so different.

Based on what is known about the magnetic properties of BFO, we might speculate as to what role its magnetic properties have on domain wall conductivity. Experiments with BFO thin films suggest that the domain walls possess unusual magnetic properties. Heterostructures made of BFO films with stripe-like domain morphologies with CoFe films deposited on top show enhancements of the exchange bias in M versus H loops. [59] Much like the AFM experiment by Seidel et al,[53] Martin et al found that this exchange bias enhancement occurred only in films that manifested arrays of stripe-like domains separated by 109° DWs and not by 71° DWs: the magnetic properties of the 109° DWs are different from those of 71° DWs. It has also been observed in electrical resistivity measurements in bulk BFO [51] that the band gap widens from ≈ 0.6 eV to ≈ 1.3 eV as the BFO is cooled below T_N. Similar changes to the band gap probably occur in thin films as well. Could the difference in the electrical conductivities of 109° DWs and 71° DWs be due to differences in their magnetic properties, as well as their structural characteristics?

The ability to create quasi-regular arrays of stripe-like ferroelectric domains separated by a single type of domain wall in epitaxial thin films of BFO makes it possible to study the unique properties of such systems using x-ray scattering. In this chapter, we will describe the progress we have made in characterizing the structural properties of these domain arrays using Cu K_α x-ray diffraction, and in modeling these properties with conceptually simple charge density models. Data from resonant soft x-ray scattering studies of these domain arrays will also be presented. Resonant scattering due to the spatial modulation of Fe 3d valence states will be described. The modulation of the Fe 3d valence states

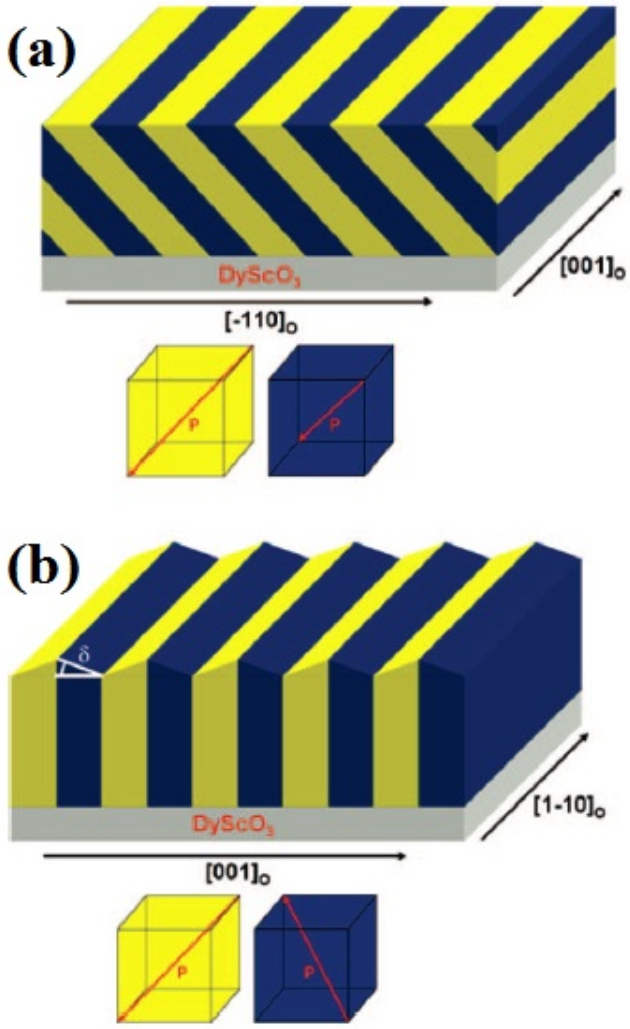

Figure 4.4: DW geometry for (001)-oriented BFO thin films exhibiting periodic arrays of stripe-like ferroelectric domains on (110)-oriented DSO substrates. Domains with polarizations that point in different directions are colored yellow and blue; the direction of the polarization is indicated by red arrows in the yellow and blue cubes (a) 71° DW system; these domain walls are canted by 45° with respect to the [-110] and [110] substrate directions. (b) 109° DW system, with domain walls perpendicular to the substrate surface. Notice the surface puckering. The angle of the canted domain surface with respect to the substrate surface is labeled δ. From Reference [58].

exhibits the same period as that of the ferroelectric domain array. We will discuss how that modulation of the Fe 3d valence states may relate to magnetic ordering in the domain structure. Attempts to detect resonant scattering due to the domain array structure near the O K edge will be discussed. Finally, our plans to understand the origins of the resonant scattering seen near the Fe L_3 transition edge will be outlined, particularly in the context of whether there is a magnetic character to the resonant scattering.

4.2 Structure of Stripe-like Domain Arrays: PFM and Hard X-ray Diffraction

The epitaxial BFO thin films studied in this work were grown by Qing He, formerly of the Ramesh group at the University of California at Berkeley and now at the Advanced Light Source, Lawrence Berkeley National Laboratory. The films exhibit only 109° and 71° DWs. In all, three 109° DW samples and one 71° DW sample were studied. For tracking purposes, the three 109° samples shall be called 109-1, 109-2, and 109-3.

The films were grown using the pulsed laser deposition method, the details for which may be found in Reference [58]. The films were grown on (110)-oriented $DyScO_3$ substrates with very low miscut angles. No $SrRuO_3$ electrodes were used to create the 109° DW samples; such electrodes were used to create the 71° DW film, which was used to manipulate the electrostatic boundary conditions on the film during growth.

The ferroelectric properties of the stripe-like domain arrays in the films were characterized using piezoresponse force microscopy (PFM). A Cypher AFM-PFM microscope from Asylum Research was used. The principles of PFM are explained in detail in Reference [60]; they are summarized here.

A cantilever with a sharp tip is scanned over the surface of a sample while the cantilever is driven to vibrate such that it periodically taps the surface. The position of the cantilever is tracked using a laser beam reflected from the cantilever. The cantilever deflection phase and amplitude is collected along "lateral" and "vertical" channels. The lateral signal is due to torsion of the AFM cantilever from forces on the apex of the tip along the direction of the scan. The vertical signal is due to deflection and bucking of the cantilever from forces on the apex of the tip directed normal to the surface or along the length of the cantilever, respectively.

To study the piezoelectric response, an electric field from a conductive AFM tip is emitted to induce a piezoelectric response of the sample region just below the tip. If the ferroelectric moment has a component along the lateral or vertical directions, this will cause the sample to distort along those directions. These distortions affect both the deflection magnitude and phase of the oscillation with respect to the driving force. The AFM phase and amplitude can change drastically when the ferroelectric moment changes direction, resulting in strong contrasts of these quantities from one domain to the next. Strong contrasts in amplitude can be caused by orienting samples such that the in-plane components of the ferroelectric moments point either (mostly) in the scan direction, or perpendicular to the cantilever length.

The spatial resolution and the probe depth of PFM is often poor compared to the length scales of objects we are interested in, such as the widths of domain walls, which are ~ 1 nm. In contrast, the lateral resolution of AFM is around 10 - 100 nm, depending on the radius of the tip. Field lines produced by con-

ducting tips also spread beyond the area below the tip, causing the piezoelectric distortion of the sample to occur over a wide area around the tip, which further worsens the spatial resolution. Given the $\sim$ 100 nm thicknesses of the BFO samples, the field of the AFM tip does penetrate and probe the whole depth of the film samples. The radius of the Cr/Pt tips used to measure the PFM had radii $\sim$ 25 nm. The lateral spread of the field from the tip likely broadens the lateral resolution further, to $\sim$ 30-35 nm.

PFM measurements of the ferroelectric domain array structure in our BFO thin film samples were conducted by R. Anoop Damodaran, of the Materials Science Department at the University of Illinois.

We first discuss the ferroelectric domain arrays of the 109° DW samples, the data for which is shown in Figure 4.5 Topographical data from AFM of the surfaces show stripe-like features parallel to the ferroelectric domains arising from surface puckering associated with 109° DW samples. In these scans, debris on the surface can be seen, in the form of red dots in the lower right corner of Figure 4.5(o). This likely is from silver paste used to glue the undersides of the samples to copper blocks needed for experiments at X1B. (See the Methods chapter.) Both lateral and vertical PFM phase data show a modulation of the ferroelectric moment direction and magnitude (see Figure 4.5(e, f, i, j, m, and n)), consistent with the established behavior of the ferroelectric moment in 109° DW films. [58] Note that Figure 4.5(e) and Figure 4.5(f) are shifted by ≈ 0.5 μm from each other.

Fourier transforms of the lateral phase data (as well as vertical phase data, not shown) show peaks (blue spots) next to the zero-momentum peak at the center of the plot arising from periodic ferroelectric domain structure. Notice that the peaks lie along a line perpendicular to the domain walls in Figure 4.5(h, l, and p). The domain period associated with the array of ferroelectric domains can be determined by the momentum spacing of the peaks from the zero-momentum position. The values of the domain spacing extracted from Fourier transforms of the PFM data are summarized in the first row of data in Table 4.1. The main features of the topographical data from the 71° DW sample (Figure 4.5(c)) are red and green spots from silver paste debris on the surface—just like those seen in the 109-3 sample in Figure 4.5(o)—and faintly visible viscinal steps. The vertical amplitude data (not shown) shows no indication of contrast due to domains of alternating ferroelectric moment, just a faint signal from cross-talk from the lateral amplitude data. The lateral amplitude (Figure 4.5(a)) and phase (Figure 4.5(b)) data show very clear modulations of the ferroelectric moment direction and magnitude.

The Fourier transform of the lateral phase data provides information that shows that the momentum of the domain structure is associated with a domain period of 2974.1 $\pm$ 575.8 Å. As in the 109° DW case, the error is determined using the full width at half maximum of the Fourier peak. The 71° DWs are nominally tilted by 45° with respect to the substrate normal (see Figure 4.4(b)).

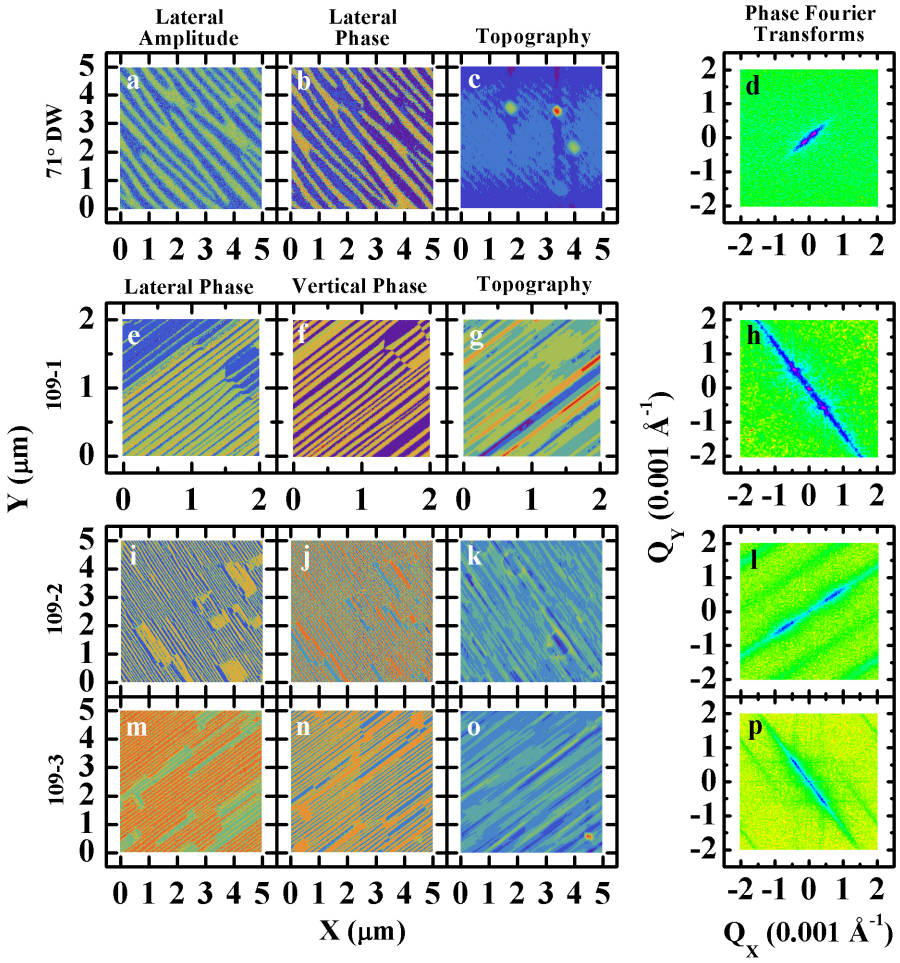

Figure 4.5: Real space PFM and representative Fourier transforms of that data from the ferroelectric domain structure of the 109-1, 109-2, 109-3, and the 71° DW sample. Real space PFM data from the 71° is shown in parts (a) - (c). Both the lateral phase and amplitude show strong contrast due to the lateral component of the polarization in neighboring domains alternating directions. Part (c) shows a topographical map of the film surface. The green and red dots are from debris on the surface of the film. Part (d) shows the Fourier transform of the lateral phase information. There are two peaks (magenta) associated with the domain period at momenta consistent with a period of 4206.0 Å. Data for the 109° DW samples are organized in a similar way, except lateral and vertical phase data are shown. Notice that the PFM scans in parts (e) and (f) are shifted with respect to each other by 0.5 μm. The Fourier peaks in part (h) for the 109-1 sample are located at momenta equivalent to a domain period of 1140.2 $\pm$ 283.9 Å, with the error obtained from the width of the Fourier peak; in part (l) for the 109-2 sample, the domain period is 1013.0 $\pm$ 349.9 Å; in part (p) for the 109-3 sample, the domain period is 1210.1 $\pm$ 230.4 Å.

The tilt of the 71° walls causes the domain spacing extracted from PFM to be $\sqrt{2}$ larger than the true domain repeat distance. For completeness, the momentum interval between the Fourier peak and the zero-momentum peak in the PFM

	109-1	109-2	109-3
Domain period (Å)	1140.2 ± 283.9	1013.0 ± 349.9	1210.1 ± 230.4
c (Å)	3.9675	3.9849	3.9863
d-spacing (Å)	1123.5 ± 272.9	985.3 ± 247.0	1318.4 ± 413.1

Table 4.1: Parameters of the film lattice and domain structure from PFM and XRD measurements of the 109° DW samples: 109-1, 109-2 and 109-3. The first row of data displays the periods of the ferroelectric domain structures of each film, as obtained from Fourier transforms of their PFM data. The second row displays the c-axis parameters associated with the BFO (0, 0, 1) Bragg peak, as determined in the XRD data. The third row displays the in-plane d-spacing associated with the sidebands seen in the XRD data.

scan, before compensating for the domain wall geometry, is consistent with a d-spacing of d = 4206.0 Å.

While PFM provides information regarding the coarse features of the ferroelectric domain structure, in order to obtain information regarding the lattice structure near and at the domain walls, a more sensitive probe is required. Naturally, the method we will use is x-ray scattering.

In what follows, hard x-ray diffraction data will be presented in order to characterize the real space structure of the domain walls in the BFO thin film. This will be done by attempting to simulate the observed x-ray diffraction with simple charge density models. Developing these models for the domain walls may inform the way we analyze our soft x-ray scattering data, which is presented in the next section, since it gives us a template for how to construct real space models of the electronic properties of the domain structure.

This is not the first attempt to understand the structure of ferroelectric domain arrays in BFO epitaxial thin films using x-ray diffraction. Some of the most relevant works will be reviewed before we get into the details of our experiment. We begin with the studies of C. M. Folkman et al [61] on domain structures of films exhibiting 109° DWs. They used a variety of substrates to study the effect of epitaxial strain and substrate miscut on the domain structures, as well as to describe their domain morphologies and domain wall geometry. While their results were reasonable compared to their data, they approached each domain in the film as separate crystallographic lattices with no phase relation to other domains—no coherent scattering from the domain structure was considered, in other words. S. O. Hruszkewycz et al [62] examined 109° DW films on $TbScO_3$ substrates with nanometer-scale spot size beams as part of a study of the structural response of tilted domains to applied electric fields. In their study, they made spatial maps of the domain tilt angle in their films. The nature of their experiment was such that each domain was treated in isolation, rather than part of a coherent lattice of domains. Finally, C. J. M. Daumont et al [63] pursued a combined x-ray diffraction, PFM, and ab initio calculation study of 71° DW films on $SrTiO_3$ substrates. They studied Bragg peaks with in-plane components (e.g. (1, 1, 0), (0, 1, 0), and (1, 0, 0)) to examine the effect of

film thickness on the domain geometry and the symmetry of the BFO unit cell. Their treatment of the XRD data was similar to that of models of Sr-doped $PbTiO_3$ films by G. Rispens, which treats the film as a coherent crystal lattice but oddly produces streaks instead of peaks in intensity calculations.

There is still a need for simple models that can be used to describe x-ray diffraction and extract from it, in an economical manner, quantitative descriptions of the domain structure. To this end, we develop a simple charge density model based on data obtained from near the (0, 0, 1) Bragg peak in our BFO films to study the effects that 109° and 71° domain walls have on the structure factor.

To do this, we used the X'Pert MRD system at the Center for Microanalysis of Materials at the University of Illinois. The specifics of the device were described in the Methods chapter. Here, we note that we used a primary beam mask that creates an incident beam with a width of five pixels across on the line detector (or 1/32°).

We will study the momentum distribution of scattering seen near (0, 0, 1) from the domain array.

What we see and what we can resolve in momentum space is dependent on the instrument. To understand what the limits of our measurement are, the resolution function of the scattering system for this experiment must be calculated. The resolution function is plotted in Figure 4.6(f). The ideal shape of the resolution function is a rhombus, with the rhombus edge lengths determined by the pixel size of the detector and the primary beam divergence. The edges of the rhombus are oriented along lines tilted by TwoTheta/2 away from the (0, 0, L) line; the acute internal angle of the rhombus is TwoTheta degrees wide. The rhombus edge dependent on the detector pixel size is 2.22×10^{-3} Å^{-1} long and has a positive slope in Q_X/Q_Z space. This edge of the rhombus is sharply defined since the pixel has a definite size. The rhombus edge dependent on the primary beam divergence has a negative slope; due to the distribution of wave vectors associated with the primary beam divergence, this edge has no definite length. The full width at half maximum of the wave vector spread is 5.93×10^{-3} Å^{-1}. The finite incident beam energy bandwidth causes this resolution rhombus to smear out along $\vec{Q}$, which does not deviate greatly from (0, 0, L) during the scan. To account for this effect, the resolution rhombus is convolved with a Gaussian along the (0, 0, L) direction with a line width of 6.93×10^{-3} Å^{-1}.

4.2.1 109° Domain Wall: Data and Model

The diffraction data from the 109° DWs is shown in Figure 4.6(a, b, c). All data sets show a strong (1, 1, 0) Bragg peak from the $DyScO_3$ (DSO) substrate, seen at $Q_Z \approx 1.5936$ Å^{-1}. A streak-like resolution artifact intersects the DSO (1, 1, 0) peak and forms a rod of intensity tilted from the (00L) direction by

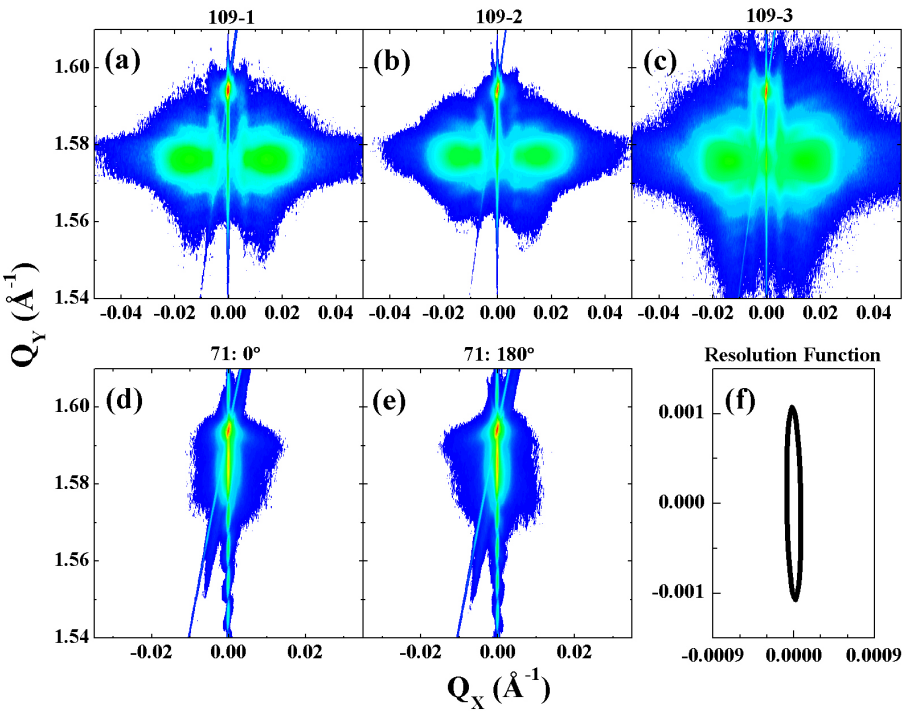

Figure 4.6: X-ray diffraction data from BFO thin film samples and the X'Pert 1 resolution function near the (0, 0, 1) peak. Strong (1, 1, 0) peaks from the DSO substrate are seen at ≈ (0, 0, 1.5936) Å^{-1} in all the diffraction data. Streak-like detector artifacts intersect the DSO peak and form rods of intensity tilted from the (00L) direction by an angle TwoTheta/2 in momentum space. Rods of scattering centered on $Q_X = 0$ passing through the DSO peak and (0, 0, 1) BFO Bragg peak along the (0, 0, L) direction arises from the finite size of the film and is a truncation effect. Parts (a)-(c) show two broad peaks that are roughly centered on (± 0.015 Å^{-1}, 0, 1.575 Å^{-1}): these are due to coherent scattering from the domain structure. Streaks of intensity near the same Q_Z as the broad peaks but at Q_X± 0.0056 Å^{-1} can also be seen. Parts (d) and (e) show diffraction data from the 71° sample, with the sample at a reference 0° orientation in part (d) and rotated by 180° about its surface normal in part (e). A streak of diffuse scattering tilted by 45° with respect to the (0, 0, L) direction in reciprocal space rotates with the sample. The resolution function for the X'Pert system is shown in part (f).

an angle TwoTheta/2 in momentum space. This feature confirms that the rod is a resolution artifact. It is likely so prominent in the data because of point-broadening effects in the line detector, as it appears at only the most intense peaks.

A rod of scattering centered on $Q_X = 0$ can be seen that passes through the DSO (1, 1, 0) peak and (0, 0, 1) BFO Bragg peak along the (0, 0, L) direction. This arises from the finite size of the film and is a truncation effect.

The surfaces of the domains in the 109° DW samples are spatially correlated, which washes out Kiessig fringes in diffraction near the (0, 0, 1) BFO Bragg

peak. As a result, there is no convenient way to infer film thickness by diffraction for the 109° DW samples. A reasonable range of thicknesses for these films is $\sim 800 - 1000$ Å.

The BFO pseudocubic lattice parameter can be extracted from the position of the film peaks, which can be seen by examining the $Q_X = 0$ rod of scattering. Sample-specific c-axis parameters are given in the second data row of Table 4.1.

Beside the $Q_X = 0$ rod of scattering, two broad peaks can be seen, which are due to coherent scattering from the domain structure, which causes the (0, 0, 1) planes of the domains to have alternating canting angles from one domain to the next (i.e. puckering). These broad peaks are roughly centered on ($\pm$ 0.015 Å^{-1}, 0, 1.575 Å^{-1}).

Some internal structure is visible in the broad peaks. Weak, vertically elongated peaks are seen in Figure 4.6(a, b, c), roughly placed at $Q_X \approx \pm$ 0.0056 Å^{-1}. The d-spacing associated with these peaks are displayed in the third data row of Table 4.1, where the errors are based on the width of the peaks. Note that the d-spacing extracted from the side bands seen in the diffraction compare well with those extracted in Fourier Transforms of the PFM data. The two data sets are compared in Figure 4.7. This confirms the notion that the diffraction pattern is due to scattering from the ferroelectric domain structure.

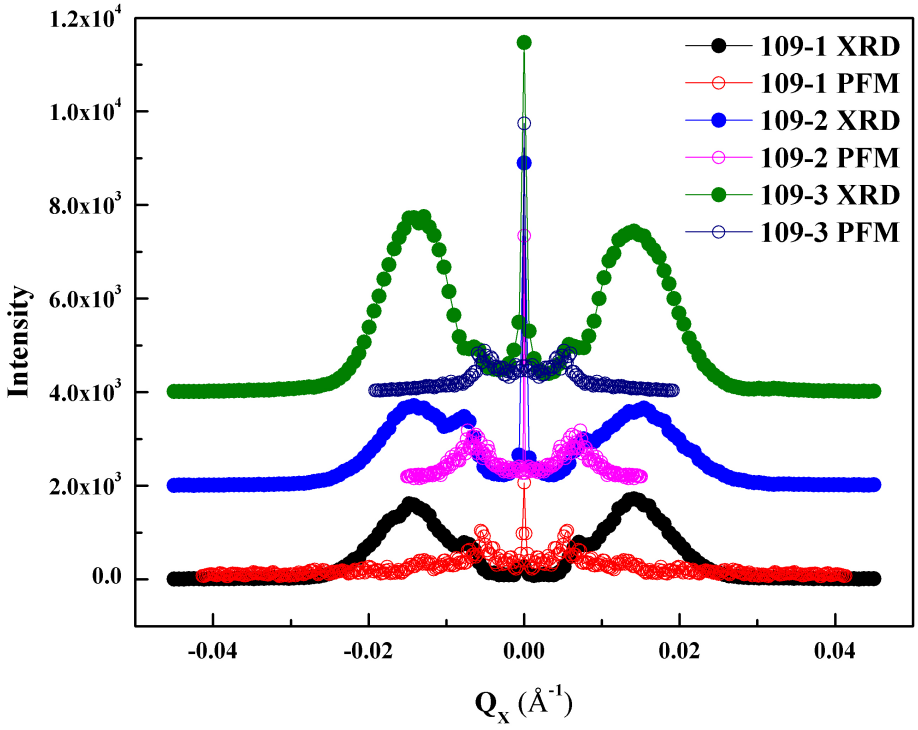

Figure 4.7: Diffraction data taken along line cuts at $Q_Z = 1.575$ Å^{-1} from 109-1, 109-2, and 109-3 are compared to line cuts taken from the PFM Fourier transforms that intersect both Fourier peaks. Note that the peaks from the Fourier transforms of the PFM and the side bands seen in scattering have approximately the same in-plane momenta.

An interesting side light is the presence of diffraction near the DSO (1, 1, 0) peaks in the 109° DW samples. There appear small satellites around the substrate peak, which are most prominent in 109-3, less so in 109-1, and not very apparent in the 109-2 color plot in Figure 4.6, but it is seen in all of the 109° DW samples. In 109-3, the pronounced satellite peaks appear at the same Q_Z as the substrate peak. The satellites are located at $Q_X \approx 0.005$ Å^{-1}, which is very close to the in-plane momentum of the side bands near the BFO film peak, an indicator that this scattering is due to the thin film domain structure, which is causing a modulation of the substrate strain. This may be due to the Somiligiana dislocations that form to compensate for the domain structure. [65] With deeper study, these peaks might provide insight into how the film and substrate interact to form coherent interfaces for this system.

We will now attempt to demonstrate that the essential features of the data just discussed can be described using a simple charge density model. In our model, the average charge density of the film remains the same from domain to domain. The contrast mechanism giving rise to coherent scattering between the ferroelectric domain structure and the Bragg peaks of the domains is the fact that the canting angles between adjacent domains alternate in direction.

In what follows, we will use a coordinate system that has its X-axis parallel to the substrate surface and its Z-axis perpendicular to the substrate surface.

Since only the (0, 0, 1) peak is considered in this model, instead of using a realistic unit cell one can substitute it with a sinusoidal function with a period equal to the c-axis lattice parameter.

Step functions are used to define the ferroelectric domain walls. Consequently, the model treats the domains as sharply defined rectangular slabs of infinite extent along the Z-axis with widths along the x-axis that are half the ferroelectric domain period. Pairs of these slabs form the motifs that repeat throughout the film. The period of the resulting domain pattern is used as a parameter that can be varied to fit the diffraction data of each 109° DW film. The domain walls are not given any internal structure and just act as sharp edges to the bulk like domains.

Since adjacent domains are distinguished by the alternating sign of their (0, 0, 1) plane canting angles, the basic repeating unit of the charge density model is a pair of adjacent ferroelectric domains with c-axis directions that are mirror reflected about the Y-Z plane. The c-axis modulation wave vectors for each canted domain are restricted to the X-Z plane: $\vec{k}_R = \frac{2\pi}{a}(\hat{x}\sin(\alpha) + \hat{z}\cos(\alpha))$ and $\vec{k}_L = \frac{2\pi}{a}(-\hat{x}\sin(\alpha) + \hat{z}\cos(\alpha))$, where a is the pseudocubic lattice parameter and α is the domain canting angle. The subscripts "L" and "R" denote the direction in which the c-axis of each domain points. This angle is nominally $\alpha \sim 0.34°$, as estimated from AFM measurements in Reference [58]. The value of a extracted from (0, 0, 1) BFO peaks in the diffraction data will be used and the canting angle α will act as a fit parameter.

The domain walls are parallel to the (1, 0, 0) planes and therefore parallel

to the substrate normal. The real space charge density model for this repeating unit of domains is, then:

$$\begin{aligned}\rho_{cell} &= \rho(\cos(\vec{k}_R \cdot \vec{r})\Theta(x)\Theta(\frac{d}{2} - x) + \cos(\vec{k}_L \cdot \vec{r})\Theta(-x)\Theta(x + \frac{d}{2})) \\ &= \rho(\cos(\frac{2\pi}{a}(x\sin(\alpha) + z\cos(\alpha)))\Theta(x)\Theta(\frac{d}{2} - x) \\ &\quad + \cos(\frac{2\pi}{a}(z\cos(\alpha) - x\sin(\alpha)))\Theta(-x)\Theta(x + \frac{d}{2}))). \quad (4.1)\end{aligned}$$

The parameter d is the ferroelectric domain repeat distance and, like α, will be used as a fit parameter to model the data.

Equation 4.1, the real space expression for a single repeating pair of ferroelectric domains, is the motif used to create an expression that describes the domain structure of the whole film. Call this expression $\rho(x, z) = \sum_{n=-\infty}^{\infty} \rho_{cell,n}(x, z)$, with the index n running over all pairs of ferroelectric domains, tracking the shift of the coordinate system of each cell from the cell at the origin: $x \to x+nd$.

The structure factor associated with this charge density modulation needs to be calculated. To do this, the scattering amplitudes associated with the charge density model have to be determined. Since $\rho(\vec{r}) = \sum_{\vec{G}} \rho_{\vec{G}} e^{-i\vec{G}\cdot\vec{r}}$, to obtain the scattering amplitude $\rho_{\vec{G}}$ associated with the reciprocal lattice vector $\vec{G}$ of the domain array, the Fourier transform of the real space charge density must be calculated.

The Fourier transform of ρ separates into an unit cell integral that is analogous to $\rho_{\vec{G}}$ and a lattice sum: $\sum_{n=-\infty}^{\infty} e^{-ik_X nd}$. The lattice sum only runs over one dimension, as 109° DW films are being treated as one dimensional lattices. The unit cell integral is a quantity proportional to the scattering amplitude for a specific one dimensional reciprocal lattice vector G. The modulus squared of the amplitude is proportional to the scattered intensity and can be compared to the measured intensity. [18] The condition required for the unit cell integral to equal ρ_G is provided by the lattice sum: for any given reciprocal lattice vector G, the only terms in the lattice sum that positively interfere with the phase factor e^{-iGx} are those that satisfy $k_X d = 2\pi H$, where H is an integer Miller index associated with the reciprocal lattice of the domain structure.

We only consider cases where $k_Z > 0$, as our data concerns features around (0, 0, 1), so the sinusoidal functions standing in for the c-axis modulation in the domains contribute Dirac delta functions that, along with restrictions on k_X imposed by the lattice sum, restrict the scattering to a line in reciprocal space defined by $k_X = \frac{2\pi}{d}H$ and $k_Z = \frac{2\pi}{a}\cos(\alpha)$.

It should be noted that this result only holds true if the domain walls are truly oriented normal to the substrate surface; different inclinations of the walls will create different restrictions on where the diffraction can appear, as will be seen in the 71° DW case.

The scattering amplitude associated with the 109° DW structure is, then:

$$\rho_H = \frac{\rho}{4} i^{\frac{d}{a}\sin(\alpha)}((-i)^H \frac{\sin(\frac{\pi}{2}(\frac{d}{a}\sin(\alpha) - H))}{\frac{\pi}{2}(\frac{d}{a}\sin(\alpha) - H)} + i^H \frac{\sin(\frac{\pi}{2}(\frac{d}{a}\sin(\alpha) + H))}{\frac{\pi}{2}(\frac{d}{a}\sin(\alpha) + H)}). \quad (4.2)$$

In calculating Equation 4.2, the volume of the two-domain unit cell $V_{cell} = a^2 d$ was used to normalize the ρ_G extracted from the Fourier transform.

With a model scattering amplitude in hand, it is possible to compare the model to the diffraction data from the 109° DW samples and extract values of the canting angles of the (0, 0, 1) planes and the ferroelectric domain period. The data plotted in Figure 4.6 was sampled along a line at $Q_Z = 1.576$ Å^{-1}, which cuts through the centers of the broad peaks as well as the side bands associated with the film domain structure. Least-squares fits to the data were performed on 109-1 and 109-2 data using Gaussian broadened structure factor peaks in order to account for the role of disorder in the domain structure; the full width half maximum of the Gaussian broadening was $\approx 9 \times 10^{-3}$ Å^{-1}. Data points comprised by the sharp peak centered on $Q_X = 0$ were not included, as the peak likely arises from a feature other than the ferroelectric domain structure.

Realistic fit parameters were obtained: they are listed in Table 4.2. The average canting angle is 0.569°, which is consistent with the $\approx 0.34°$ canting angle reported in Reference [58], and the domain structure periods are within 20% of the PFM values. The broad peaks seen in diffraction were successfully captured with the model, which arise from canted (0, 0, 1) Bragg peaks "blazing" (as in a blazed grating) several lower order structure factor components in the model. Importantly, features corresponding to the domain structure side bands seen in the data are also reproduced at approximately the same in-plane momentum positions.

A fit to the 109-3 data that reproduced both the domain structure side bands as well as the diffraction related to c-axis plane canting could not be obtained using the same method used for the 109-1 and 109-2 data. A reasonable set of model parameters was chosen to obtain a result that resembled the 109-3 diffraction data and, for completeness, they are listed in Table 4.2. The $Q_Z = 1.576$ Å^{-1} diffraction data and the model fit results are plotted together in the bottom panels of Figure 4.8; the top panels of the figure feature model fits with reduced Gaussian broadening, to highlight the positions of the structure factor peaks generated by the model.

4.2.2 71° Domain Wall: Data and Model

Unlike the 109° DW samples, the (0, 0, 1) of the 71° DW sample should be a single peak due to the c-axis modulation of the film. Without a c-axis canting angle contrast, no harmonics or other interesting diffraction is anticipated. However, a subtle diffraction feature can be seen, which we will show is associated with the momentum of the domain wall array in this system.

	109-1	109-2	109-3
α (°)	0.572	0.565	0.548
domain period (Å)	924.6	864.3	1034.0

Table 4.2: Values for the c-axis tilt angles α and ferroelectric domain periods for the 109° DW samples. These values have been obtained by fitting the model structure factor, in Equation 4.2, to the XRD data, displayed in Figure 4.7. Fit parameters for 109-1 and 109-2 were obtained using a least-squares method. Fit parameters for 109-3 were obtained by choosing a reasonable set of fit parameters to obtain a result that resembles the 109-3 XRD data.

Let us first examine the data, shown in Figure 4.6(d, e), with the data shown in Figure 4.6(d) taken with the sample in a reference 0° position and the data in Figure 4.6(e) taken with the sample rotated about its surface normal by 180°. Just as for the 109° DW samples, a DSO (1, 1, 0) Bragg peak is seen at $Q_Z \approx 1.5936$ Å^{-1}. The BFO pseudocubic lattice parameter can be extracted from the film peak position, by which we conclude that a = 3.9641 Å.

The 71° DW sample has a very smooth surface, which is due to a lack of domain puckering [58]. Kiessig fringes are quite visible in the diffraction along the (0, 0, L) rod of scattering running through the BFO and DSO Bragg peaks, as is shown in the Q_X/Q_Z plots of the data in Figure 4.6(d, e). A fit to the Kiessig fringes in our data yields a film thickness of 727 ± 26 Å.

There is weak diffuse scattering centered on the (0, 0, 1) Bragg peak at $Q_Z \approx 1.5849$ Å^{-1}. The diffuse scattering runs along a line tilted 45° away from the (0, 0, L) direction. This angle is significant since the domain walls are supposed to be tilted 45° away from the substrate normal. The direction along which the diffuse scattering runs strongly indicates that it arises from the domain structure. Note also that the Kiessig fringes are broadened in the same manner as the (0, 0, 1) Bragg peak.

The diffuse scattering runs along a line tilted by 45° to the right in Figure 4.6(d) to a line tilted 45° to the left in Figure 4.6(e). The change in direction of the diffuse scattering is due to the rotation of the sample by 180°. Notice that the other features of the data do not change direction as the diffuse scattering does. These invariant features are from the detector point broadening effects, as seen in the 109° DW data. To be specific, these features include the rod like artifact intersecting the DSO (1, 1, 0) peak and a similar rod like artifact around the (0, 0, 1) BFO film peak, running parallel to the DSO (1, 1, 0) centered artifact. Unfortunately, the presence of this detector artifact complicates the study of the diffuse scattering.

The weak diffuse scattering around the BFO (0, 0, 1) displays some fine structure but it is not as well defined as the peaks of the 109° DW case. Line cuts taken through the Q_X/Q_Z plots, along the diffuse scattering and in a direction perpendicular to it, in both the 0° and 180° sample orientations have been made to examine the diffuse scattering fine structure. Two perpendicular line cuts are shown in Figure 4.9 with the sample in the 0° orientation. The

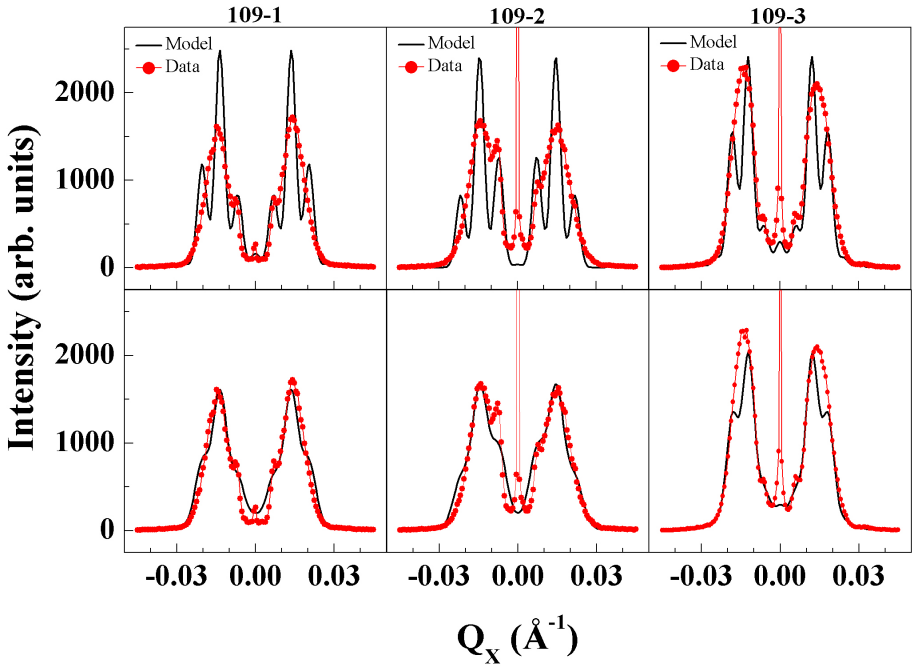

Figure 4.8: Structure factors calculated from real space models of the 109° DW structure is compared to data in this figure. Bottom panels show the result for least-squares fits for 109-1 and 109-2 and a fit by eye for 109-3. The top panels show the same data and model fits except that the Gaussian broadening of the structure factor peaks have been reduced to better indicate where the structure factor peaks are located in reciprocal space.

intensity of the line cut is plotted against Q_X. The line cuts show small sharp peaks at $Q_X \approx$ -0.003 Å^{-1} and -0.0015 Å^{-1}. These peaks arise from the detector artifact mentioned earlier and do not reflect any intrinsic properties of the sample. The line cuts parallel and perpendicular to the diffuse scattering, represented respectively by orange and black lines in Figure 4.9, appear to be similar except for a shoulder in the diffuse scattering around $Q_X \approx 0.003$ Å^{-1}, a feature missing in the line cut perpendicular to the diffuse scattering.

One way to tell if this fine structure in the diffuse scattering is intrinsic to the sample or if it is spurious would be to look for a companion peak on the other side of the (0, 0, 1) peak. However, the detector artifact obscures any scattering signal that might be present at $Q_X \approx$ -0.003 Å^{-1}, which is where such a companion peak would appear in the line cut. A similar but weaker shoulder is seen at $Q_X \approx 0.003$ Å^{-1} in the diffuse scattering line cut taken from the 180° data.

If this shoulder is a domain diffraction peak, it would suggest that there is a modulation of the (0, 0, 1) Fourier component of the charge density, and that this modulation is somehow associated with the array of 71° domain walls.

Unlike the 109° DW samples, there is no canting angle contrast mechanism for the 71° DW case, since the (0, 0, 1) peaks of neighboring ferroelectric do-

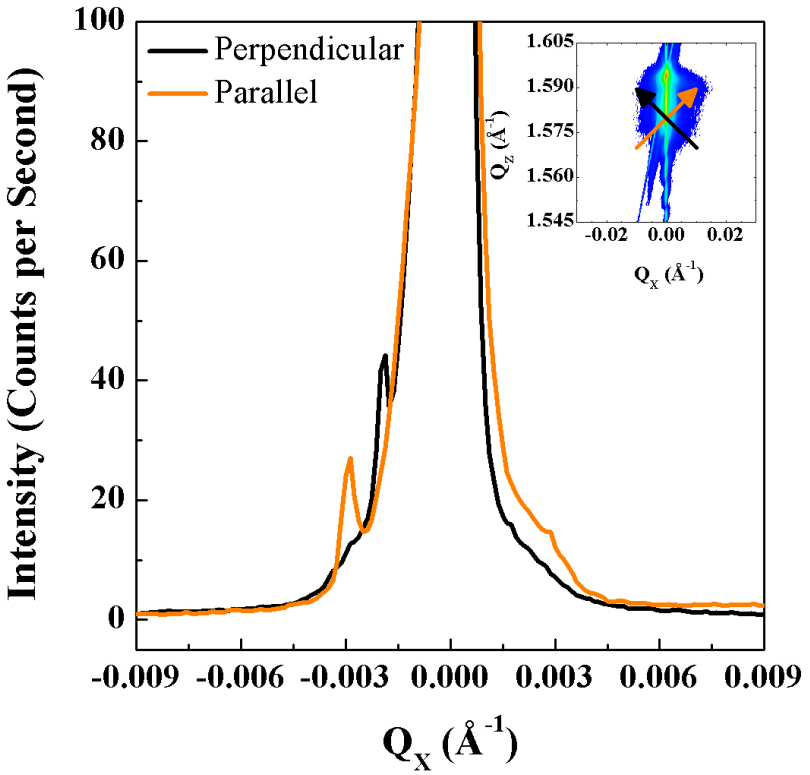

Figure 4.9: Line cuts taken from the 0° diffraction data of the 71° sample. The line cut through the diffuse scattering around the (0, 0, 1) Bragg peaks of the 71° DW sample (orange) is plotted against a line cut in a direction perpendicular to the diffuse scattering line cut in order to show the presence of fine structure in the diffuse scattering that is not present in the line cut in the perpendicular direction. Peaks at $Q_X \approx$ -0.003 and -0.0015 Å^{-1} are from detector artifacts.

mains separated by 71° DWs are parallel to each other. This constraint on the (0, 0, 1) directions is necessary in order for the film to form coherent interfaces along the {110} crystallographic planes. Given the orientation of the diffuse scattering, we postulate that charge density fluctuations in the film associated with the domain wall array cause the diffuse scattering. In the model, we give the density fluctuation the same period as the domain walls: $\frac{d}{2\sqrt{2}}$.

Like the 109° DW case, a sinusoidal function with a period equal to the measured c-axis lattice parameter of the 71° DW sample stands in for the detailed unit cell. 71° DWs are parallel to the (101) planes, and step functions are used to define the domains. It may be convenient to use a coordinate system that is rotated by 45° compared to the 109° DW case, such that the Z-axis is parallel to the domain walls (tilted 45° away from the surface normal), and the X-axis is perpendicular to the domain walls, mimicking the 109° DW arrangement. The relationship between the rotated system and the 109° DW coordinate system is explicitly stated: $\hat{z}_{71} = \frac{\hat{x}_{109}+\hat{z}_{109}}{\sqrt{2}}$ and $\hat{x}_{71} = \frac{\hat{x}_{109}-\hat{z}_{109}}{\sqrt{2}}$. The subscripts denote which coordinate system we are using.

In this rotated coordinate system, the c-axis modulation wave vector is $\vec{k}_c = \frac{2\pi}{a}\frac{\hat{z}_{71}-\hat{x}_{71}}{\sqrt{2}}$ and the domain wall wave vector is $\vec{k}_{DW} = \frac{4\pi\sqrt{2}}{d}\hat{x}_{71}$

The real space model for the charge density of a single domain is

$$\begin{aligned}\rho_{cell} &= \rho(1+\Delta Cos(\vec{k}_{DW}\cdot\vec{r}))Cos(\vec{k}_c\cdot\vec{r})\Theta(x)\Theta(\frac{d}{2\sqrt{2}}-x) \\ &= \rho(1+\Delta Cos(\frac{4\pi\sqrt{2}}{d}x))Cos(\frac{\sqrt{2}\pi}{a}(z-x))\Theta(x)\Theta(\frac{d}{2\sqrt{2}}-x). \quad (4.3)\end{aligned}$$

In Equation 4.3, d = 4606.0 Å is the average ferroelectric domain period seen by the PFM scans of the film surface and Δ is a dimensionless parameter that describes the amplitude of the charge density fluctuations. It is assumed that the fluctuations of the average charge density will be small, Δ should be much smaller than unity.

As before, ρ_{cell} is used to create an expression that covers the whole film's domain structure, with an index n that tracks the shift of the coordinate system for each cell. Along the X-axis, the unit cell must shift by $x \to x + n\frac{d}{2\sqrt{2}}$; along the Z-axis, the shift is $z \to z + n\sqrt{2}aMod(\frac{d}{4a},1)$. The shift along Z is unique to the 71° DW case and needs a little explaining. The shift along Z by integer multiples of $\sqrt{2}aMod(\frac{d}{4a},1)$ must be imposed on this model to maintain epitaxial domain walls (i.e. crests of c-axis modulations in one domain smoothly match the crests of neighboring domains). Note that for the 109° DW samples that the real space model automatically displayed this quality due to the symmetric canting of the c-axis planes in the left and right domains. The notation $Mod(\frac{d}{4a},1)$ means "d/4a modulo 1", the non-integer part of the ratio. For ease of reading, $\zeta \equiv Mod(\frac{d}{4a},1)$.

The Fourier transform of $\rho(x,z) = \sum_{n=-\infty}^{\infty}\rho_{cell,n}(x,z)$ separates into an integral over a unit cell and a lattice sum. The arguments of the lattice sum terms restrict the non-zero scattering amplitudes to a line defined by $2\pi H = k_X\frac{d}{2\sqrt{2}} + k_Z\sqrt{2}a\zeta$, where H is an integer Miller index associated with domain scattering. We only consider $k_Z > 0$, ensuring that even in this rotated coordinate system that the structure factor terms we examine are near (0, 0, 1). Doing this, the sinusoidal function standing in for the c-axis modulation contributes a Dirac delta function in the Fourier transform, restricting $k_Z = \sqrt{2}\pi/a$. If follows from this that $k_X = \frac{4\sqrt{2}\pi}{d}(H-\zeta)$.

The scattering amplitude as a function of H is, then:

$$\begin{aligned}\rho_H = \frac{\rho}{2}e^{-i\pi(H+\frac{d}{4a}-\zeta)}(&\frac{Sin(\pi(H+\frac{d}{4a}-\zeta))}{\pi(H+\frac{d}{4a}-\zeta)} \\ &-\frac{\Delta}{2}(\frac{Sin(\pi(H-1+\frac{d}{4a}-\zeta))}{\pi(H-1+\frac{d}{4a}-\zeta)}+\frac{Sin(\pi(H+1+\frac{d}{4a}-\zeta))}{\pi(H+1+\frac{d}{4a}-\zeta)})). \quad (4.4)\end{aligned}$$

This expression was obtained by dividing the integral over the unit cell in the Fourier transform by $V_{cell} = a^2\mathrm{d}/2$, which endows ρ_H with units of charge

density, just as we did for the 109° DW case.

The model results in two satellite peaks around the (0, 0, 1) Bragg peak. The first term in Equation 4.4 creates a peak at $\vec{Q}_0 = \frac{\sqrt{2}\pi}{a}(-\hat{x}_{71}+\hat{z}_{71}) = \frac{2\pi}{a}\hat{z}_{109}$, which is the (0, 0, 1) Bragg peak. The second and third terms cause harmonic peaks around (0, 0, 1) due to the density modulation $\vec{Q}_{\pm} = (-\frac{\sqrt{2}\pi}{a} \pm \frac{4\sqrt{2}\pi}{d})\hat{x}_{71} + \frac{\sqrt{2}\pi}{a}\hat{z}_{71} = \frac{2\pi}{a}\hat{z}_{109} \pm \frac{4\sqrt{2}\pi}{d}(\frac{\hat{x}_{109}-\hat{z}_{109}}{\sqrt{2}})$. These harmonics lie on lines tilted by 45° away from the (00L) direction; which line they lie on depends on the solution selected.

Using the charge density model created for the 71° DW system to calculate the structure factor components of this system, we find a reasonable agreement between the data and model. The simulated scattering using the model is shown in Figure 4.10. Account has been made of the instrumental broadening, crystal

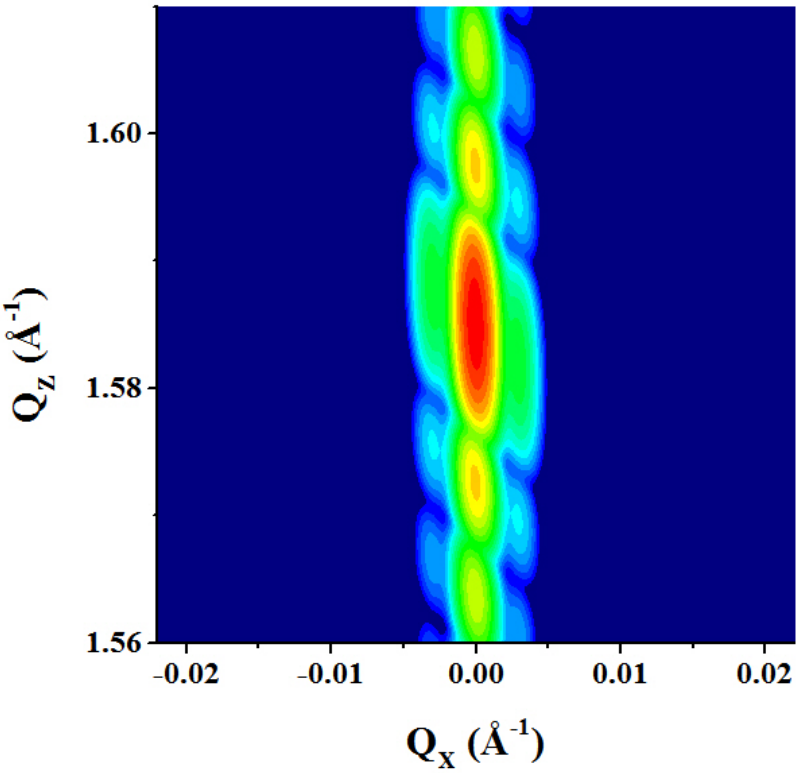

Figure 4.10: Simulated 71° DW scattering in the Q_X/Q_Z plane. The resolution function and a sinc function to account for film truncation effects has been convoluted with the charge density model of the 71° system. Structure factor peaks have also been Gaussian broadened to approximate disorder in the system.

truncation, and domain disorder in the form of Gaussian broadening to make the result more realistic. The crystal truncation effects are taken into account using a convolution of the model results with a sinc function, a choice that suits this system rather well; the film thickness used is 727 Å. A fit to the data would be very difficult given the detector artifacts and other features in the diffraction

data (such as the substrate peak and its tails) that we did not choose to model. We confine ourselves to qualitative comparisons of the model results to the data.

There is a quite reasonable agreement between the location of the harmonic peaks and the shoulder-like features observed in the line scans through the diffuse scattering. The harmonic peaks that result in the charge density model are located $\frac{4\pi\sqrt{2}}{d} = 0.00423$ Å^{-1} away from the BFO (0, 0, 1) in reciprocal space. The shoulder-like features seen in the line scan through the diffuse scattering have $Q_X \approx 0.003$ Å^{-1}, which means that the reciprocal space interval between the shoulders and the BFO (0, 0, 1) is ≈ 0.00424 Å^{-1}, which translates into a d-spacing of 1485.4 Å that is very nearly equal to the domain wall period: $\frac{d}{2\sqrt{2}}$ = 1487.0 Å.

Comparing the intensities of the (0, 0, 1) peak to the intensity of the shoulder at $Q_X \approx 0.003$ Å^{-1}, the ratio of which is $\sim 10^3$, one can estimate that $|\Delta| \sim 0.06$. Since there are only first order harmonic peaks, the model does not capture the very weak but persistent tails of the diffuse scattering away from the (0, 0, 1).

For both 109° and 71° DW systems, the charge density model approach to describing the domain structures works fairly well: it can reproduce essential features of the diffraction data and plausibly extract realistic values of important physical parameters.

The canting angle contrast model captures the essential features of the diffraction data from the 109° DW samples. Values of the canting angles of the (0, 0, 1) planes obtained from fits to the diffraction data compare favorably to the AFM result reported by Chu et al in Reference [58]. The domain array periods extracted from the data using the model are also within the error bars of the PFM values of the domain array periods of the samples.

The charge density fluctuation model successfully reproduces many of the features of the diffuse scattering around (0, 0, 1) in the 71° DW sample. Using 45° inclined domain walls in the model, harmonic peaks that lie along the rod of diffuse scattering were described. The position of the harmonic peaks in the model coincides with faint shoulder-like features seen in line cuts through the diffuse scattering: the d-spacing associated with the shoulders is nearly equal to the domain wall period.

The success of these domain structure models indicates that one does not necessarily need to resort to detailed analyses of unit cells and atomic positions to capture these important features.

However, there are some aspects of the data that these models did not replicate. One such feature is the mysterious central peak seen in the 109° DW data. Though there is a central peak in the model for H = 0, the intensity and sharpness of the observed peak are not accounted for by the canting angle contrast model. This could be the case because the substrate peak and its truncation rod are not accounted for in the structure factor, which will run through Q_X = 0 and give a small peak like the one seen in Figure 4.8. Defects in the sample

could also contribute. Having only surveyed 4 μm^2 and 25 μm^2 patches of film, one cannot rule out the possibility that there are regions of the sample that do not exhibit domains, which would give rise to a sharp central peak. Such regions are known to exist in other (0, 0, 1) oriented BFO films: the nanodiffraction experiments by Hruszkewycz et al, [62] on thin films exhibiting 109° DW arrays deposited by $TbScO_3$ substrates showed many areas of the film that displayed no canting of the c-axis planes.

The data also exhibits asymmetric sidebands but the model produces symmetric scattering intensities. This is not due to absorption effects, as the asymmetry changes direction if the sample is rotated 180°. The origin of this effect is unclear.

There is also a phase ambiguity in the 71° DW charge density model. The density fluctuations were spatially assigned to domain walls in the real space model. The same result for intensities will obtain if the sinusoidal modulation of the average charge density is shifted by some phase so that its crests no longer lie on domain walls. This ambiguity is an example of the classic "phase problem" of crystallography. However, if the charge densities at each domain wall are to be treated as identical, it seems natural to assume that the density modulation in a domain will be symmetric about the center of the domain, in much the same way our model was set up, rather than exhibit an arbitrary phase shift with respect to the domain structure.

It is completely undeterminable whether the charge density fluctuation amplitude Δ is positive or negative, as either value gives the same scattered intensity. This is not altogether divorced from the phase ambiguity, since it amounts to whether the sinusoidal modulation of the fluctuation should be shifted in phase by half a domain array period.

What might the physical origin of the average charge density fluctuation be and what controls its value? One possibility is strain associated with the domain walls. Regions of the film with compressive strain should have a higher average density than bulk-like regions, while regions with tensile strain should have a lower-than-bulk average density. For the 71° DW case, a model with an average density modulation parallel to the domain wall modulation successfully reproduces the fine structure seen in the diffuse scattering. It is tempting to connect the average charge density modulation to the modulations of strain normal to the domain walls. This is a reasonable connection to make, as others [66] have calculated in Landau free energy models film strains at domain walls that vary significantly from bulk values for realistic treatments of several materials.

We conclude this study of the domain structure by remarking that a simple charge density model of the domain structure compares in a satisfactory way to data collected around the (0, 0, 1) Bragg peak of BFO. For the 109° DW system, a model that accounts for coherent scattering between the canted c-axis planes and the domain structure successfully captured both the broad peaks and sharper domain modulation side bands seen in the data. For the 71° DW system,

density modulations associated with the domain walls successfully captures the fine structure seen in the diffuse scattering around (0, 0, 1).

The diffraction data also contains signatures of the substrate strain being modulated due to the formation of a coherent interface between the $DyScO_3$ lattice and the BFO film.

4.3 Resonant Soft X-ray Scattering From Stripe-like Domain Arrays

Now that we have developed a way to formulate a real space charge density model for stripe-like domain arrays displaying either 109° or 71° DW types, we need to study their electronic properties. With a thorough understanding of the electronic properties uniquely tied to the domain arrays, we hope to integrate that knowledge with our understanding of the real space structure of the domain structure. This will allow us to create a simple model for the real space susceptibility in which we can assign electronic properties to specific parts of the domain array.

Soft x-ray scattering and absorption can be used to characterize the electronic properties of BFO thin films. The domain structure forms a quasi-regular array; just as this regularity causes diffraction peaks to appear in hard x-ray data, so should it in soft x-ray scattering. The properties of the resonant scattering at Fe L and O K electric dipole transition edges should reveal the spatial modulation of the electronic states associated with Fe 3d and O 2p states. States that are modulated with the same momentum as the domain wall array will be prime candidates for study in terms of what they might reveal about the domain walls and their differences from the bulk like domains.

This part of the study is still in a state of flux. The majority of the data so far is from 109° DW samples and all further discussion will be limited to those systems.

As far as we know, this is the first resonant soft x-ray scattering study of domain modulated BFO thin films. Similar experiments on different magnetic thin films have been done, such as those of H. A. Dürr et al [67] and G. van der Laan et al [68] to characterize the structure of stripe-ordered magnetic domains in FePd thin films on (100)-oriented MgO substrates. They observed scattering from the domain structure in the form of side band peaks about the specular reflection from the film surface. The period of the domain modulation was $\sim$ 1000 Å, which is very similar to the period of our 109° DW samples. The studies made use of circularly polarized incident x-rays to discern whether there were magnetic closure domains present between the bulk domains. The asymmetry in the diffraction data between left and right circularly polarized light was claimed to be an interference effect between the closure domains and the bulk domains in coherent scattering from the total domain structure. Using

a simple model, in which the bulk domains and closure domains were treated as sinusoidal waves, the amplitudes of which and phase relation between the two would be determined by the polarization asymmetry. This is similar to the way we modeled the domain structures in our hard x-ray diffraction study. Dürr et al and van der Laan et al concluded by their fits to the data that closure domains were indeed present.

Our situation differs somewhat in that the size of some of the features we seek to characterize, such as the narrow regions between domains that form the domain walls, are rather small compared to the ~ 100 Å sized magnetic closure domains in the FePd film experiments.

To conduct the experiment, the X1B beam line at the NSLS was used. Details regarding the diffractometer and beam line can be found in the Methods chapter. Experiments were primarily conducted at the Fe $L_{3,2}$ transition edges: $\approx 706 - 720$ eV. The beam energy resolution in this range is nominally $\Delta E \sim 0.21$ eV. Some measurements were performed using O K edge light: ≈ 543 eV. The beam energy resolution in this range is $\Delta E \sim 0.16$ eV.

The x-ray absorption data obtained at the O K and Fe $L_{3,2}$ edges will be discussed first. Both the fluorescence yield (FY) and electron yield methods (discussed in the Methods chapter) were used to measure x-ray absorption spectra (XAS).

For FY measurements at both transition edges, the direct beam incidence angle was 10°, as measured from the sample surface normal, and fluorescent x-rays with take off angles of 30°, as measured from the sample surface, were measured with the detector on the TwoTheta arm.

Data at the O K edge is shown in Figure 4.11. Compared to FY XAS data from α-Fe_2O_3 in Reference [69], the O K edge data from the BFO films display a t_{2g}-like peak at 531.3 eV and an e_g like peak at 533.4 eV, which arises from hybridized O 2p-Fe 3d states in the nearly octahedral symmetry of the FeO_6 complex. Signatures of the lower-than-octahedral point symmetry can be seen in the additional fine structure in the BFO data than is present in the α-Fe_2O_3 XAS: for example, there is a small peak on the low energy side of the t_{2g} peak at ≈ 530 eV. These states were probed using resonant scattering at the O K edge and the results of that study will be described later.

FY XAS data collected at the Fe $L_{3,2}$ edges is shown in Figure 4.12. As in the O K edge data, e_g like and t_{2g} like features can be observed in the spectra, with a t_{2g} like peak at 708.4 eV and an e_g like peak at 710.2 eV in the FY spectrum. These features are qualitatively similar to XAS from orthoferrites like $LaFeO_3$ [70]. However, the FY XAS displays an extreme self-absorption effect that makes the data disproportionate to the true absorption coefficient. This is likely due to very large absorption coefficients arising near the Fe L_3 absorption edge. This will cause the penetration depth to decrease to a point where there is too little volume to create fluorescence in, suppressing the signal.

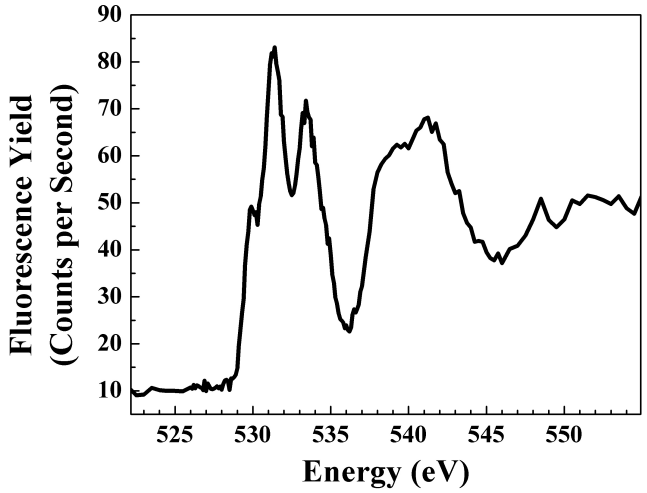

Figure 4.11: O K edge FY XAS. O K edge data from the BFO films display a t_{2g}-like peak at 531.3 eV and an e_g like peak at 533.4 eV. A small peak on the low energy side of the t_{2g} peak at $\approx$ 530 eV is also visible and likely arises from the lower-than-octahedral point group of the structure.

As an alternative to the FY technique, the electron yield (EY) technique was used. An EY spectrum is also shown in Figure 4.12 and it compares more favorably to the $LaFeO_3$ spectrum in Reference [70]. However, using the EY technique poses challenges of its own. Charging effects were observed in EY spectra in the form of a history dependence on the direction of previous EY scans, if any were done in the minutes or hour prior to it. The underlying reason for this charging effect is the fact that neither the BFO nor the $DyScO_3$ substrates are electrically conducting. To mitigate this effect, the conductive silver paint used to glue the samples onto the sample stage was also smeared around the edges of the sample to create a conductive pathway between the sample and ground. If EY measurements are performed exactly the same way many times, eventually the measured spectra attain a steady state form.

Having some knowledge of the electronic structure from XAS scans, resonant scattering studies were performed on the domain structures in the BFO samples. The momentum transfer is denoted by Miller indices in what follows: $\vec{Q} = \frac{2\pi}{a}(H, K, L)$, where the pseudocubic lattice parameter a = 3.987 Å.

No temperature dependence was observed in any of the scattering data over a range of sample temperatures from $\sim$ 100 K to room temperature. Unless otherwise indicated, the soft x-ray scattering data was obtained with the sample temperature at $\approx$ 100 K, which was done to guard against the possibility of the sample suffering thermal damage as a result of long exposure to the direct beam.

Using Fe $L_{3,2}$ transition edge x-rays, scattering from the domain structure was observed. The range of energies used prohibits observation of the (0, 0, 1) Bragg peak. However, side bands, in the form of two broad peaks about a central specular peak in H scans through the (0, 0, L), were observed. The

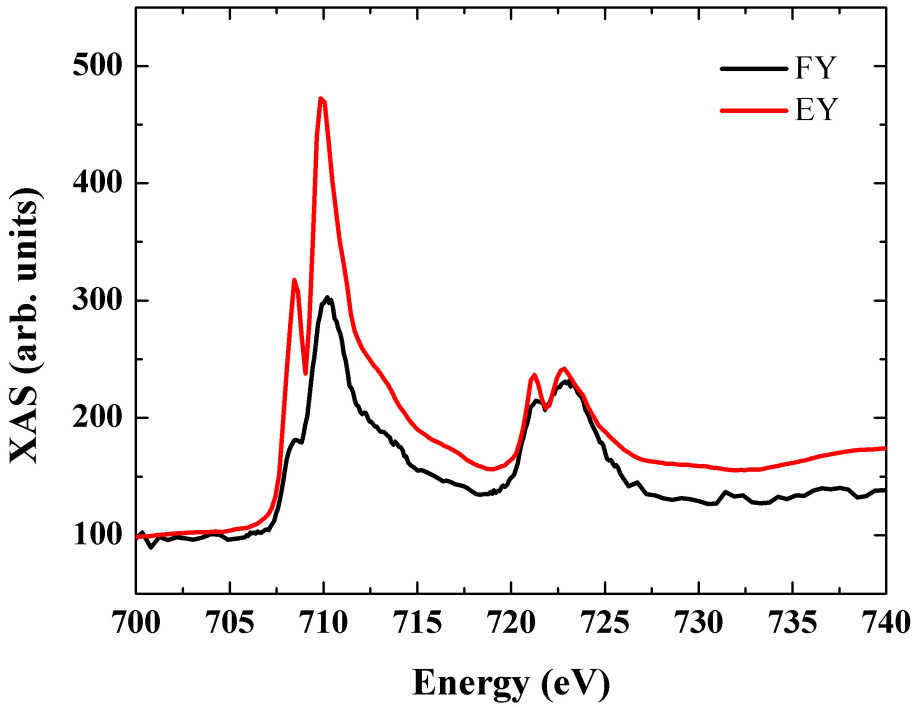

Figure 4.12: Fe $L_{3,2}$ edge XAS obtained using both the FY and EY technique. A t_{2g} like peak at 708.4 eV and an e_g like peak at 710.2 eV are apparent; analogous features are visible in the Fe L_2 XAS peak near $\sim$ 725 eV. The difference between the FY and EY spectra is due to extreme self-absorption effects in the FY.

in-plane momenta of the sidebands are consistent with the momentum of the domain period. As shown in Figure 4.13(c), using Fe L_3 x-rays ($\sim$ 707 eV to $\sim$ 712 eV), the side bands were found around (H, 0, 0.44) at $|H| = 0.0035 \pm 0.0010$, which corresponds to an in-plane modulation with a period of 1147 $\pm$ 250 Å, the same period seen in PFM and hard x-ray diffraction. The correspondence of these side bands to domain structure features seen with hard x-rays and PFM is made clear in Figure 4.14. We momentarily break from the use of Miller indices with this figure: the PFM vertical phase Fourier transform, the diffuse scattering observed near (0, 0, 1) with Cu K_α x-rays, and the Fe L_3 side band scattering are plotted on a common momentum axis. The peaks corresponding to the domain structure modulation in the PFM and hard x-ray data are located at the same in-plane momentum as the Fe L_3 side bands, $Q_X \approx 9 \times 10^{-4}$ Å^{-1}.

Scattering from the domain structure is visible at all L-values experimentally attainable. However, as can be seen by comparing parts (a) and (c) in Figure 4.13, the distribution of the scattering along the H-direction changes as L is varied. For example, in Figure 4.13(a) the domain structure scattering near (0, 0, 0.1177), rather than resembling the side bands at L = 0.44 in Figure 4.13(c), manifests itself as tails of the specular peak that do not decay quickly in intensity as H moves away from zero. The Fe L_3 transition edge scattering at L = 0.1177 appears in the same range of in-plane momenta as the sidebands

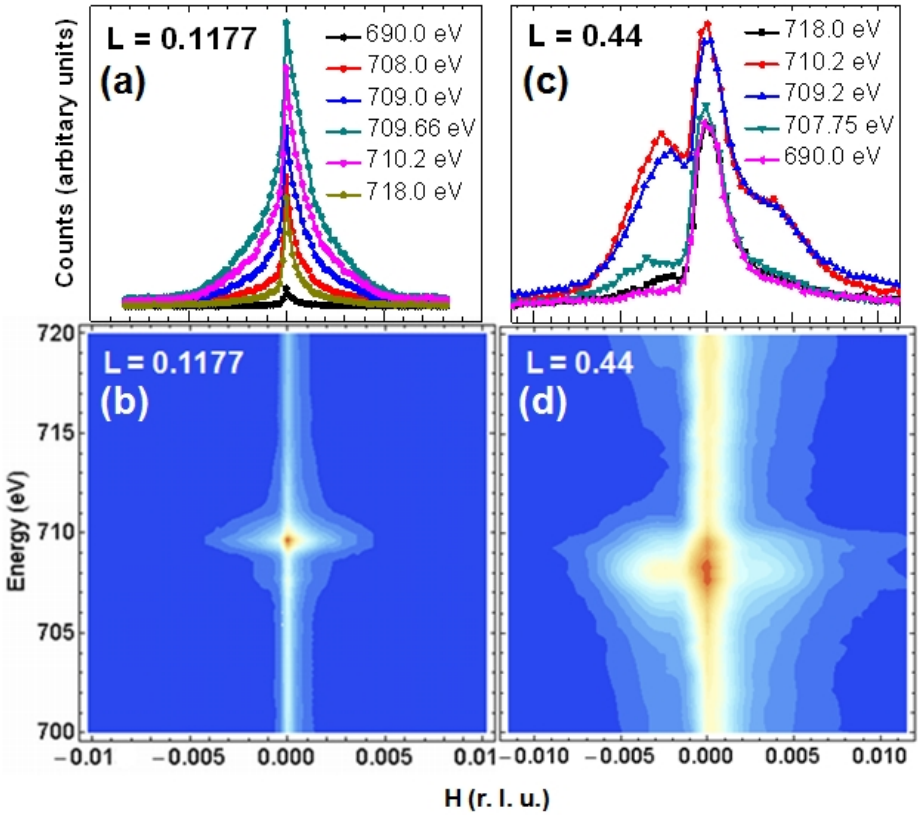

Figure 4.13: Parts (a) and (c) show side band scattering in H scans through (0, 0, 0.1177) and (0, 0, 0.44) at several incident beam energies. The line shapes and intensities of the side bands are energy dependent. In Parts (b) and (d), H versus beam energy mesh scans are presented.

seen at L = 0.44, so the scattering at both L-values can be associated with the momentum of the domain structure.

This change in the momentum distribution of the scattering between the two L positions is not due to the resolution function changing with the scattering geometry: at lower L (which means lower TwoTheta angles), the tilt angle of the resolution function rhombus away from the (0, 0, L) direction is small and the resolution function is narrow in extent along the H-direction in reciprocal space. The in-plane momentum resolution is therefore better in the low L region, and the sidebands should be more easily distinguished from the specular than at high L values, where they appear as more distinct side bands despite the poorer in-plane momentum resolution. The distribution of the scattering along the H-axis, therefore, depends in a non-trivial way on the L-position.

A detailed examination of the L-dependence of the sideband scattering was made in a series of H scans at regular L intervals at beam energy 709.7 eV. The scans form an H-L mesh, over which the square root of the intensity has been plotted in Figure 4.15. In the color scale of the figure, red denotes high intensity and blue denotes low intensity. Scattering from the stripe-like domain

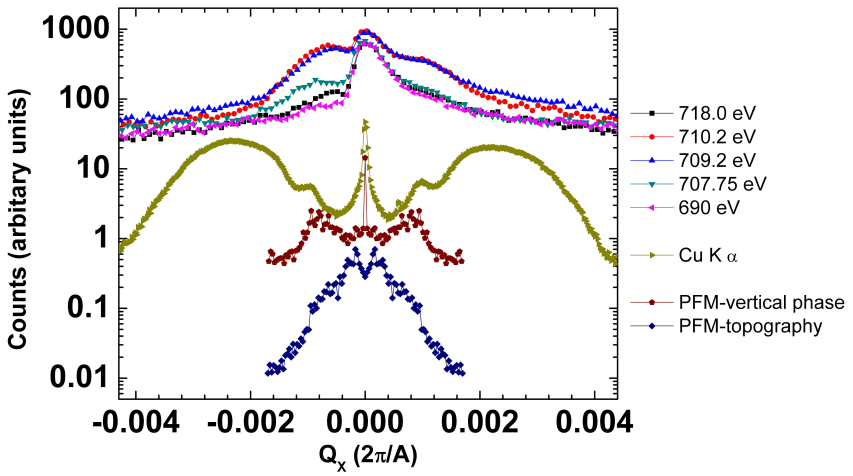

Figure 4.14: Fe L_3 edge side band scattering is compared to hard x-ray diffraction and PFM Fourier transform data.

array evolves continuously as a function of L. At L $\approx$ 0.35, the domain structure scattering intensity reaches a minimum, indicating that the electronic structure modulation being probed has more than just an in-plane modulation but also varies through the depth of the film. Modeling will be necessary to understand what the depth profile might look like. However, it can be seen that treating the domains as infinite slabs with sharp step function-like domain walls, as in the Cu K_α diffraction study, will be an unacceptable simplification for real space models based on the soft x-ray data.

The domain structure scattering displays resonance behavior near the Fe L_3 transition edge. As seen in Figure 4.13(c), even though the side bands are still visible in scattering if the beam energy is tuned away from the Fe L_3 transition edge (690 eV), the side band scattering as the beam energy nears the Fe L_3 transition edge is qualitatively different than the scattering at 690 eV. This is apparent if one compares the 690 eV scattering to the data taken at 709.2 eV and 710.2 eV. If the side band scattering at the 690 eV and, say, 709.2 eV simply differed in overall intensity and could be scaled to overlap with each other, then that would not represent resonant scattering from a modulation of the Fe 3d valence states. Instead, it would be due to resonant enhancement of the fluorescence, which does not favor any particular momentum. The energy dependence of the side band scattering is shown in greater detail in Figure 4.13(d), with the scattering along the H axis plotted against the beam energy. The intensity of the side bands at H = $\pm$ 0.0035 is shown in this figure to not mimic the background energy dependence as the beam energy is scanned.

The specular reflection at H = 0 displays the same energy dependence as the side bands. This is likely the case because the side bands and the specular

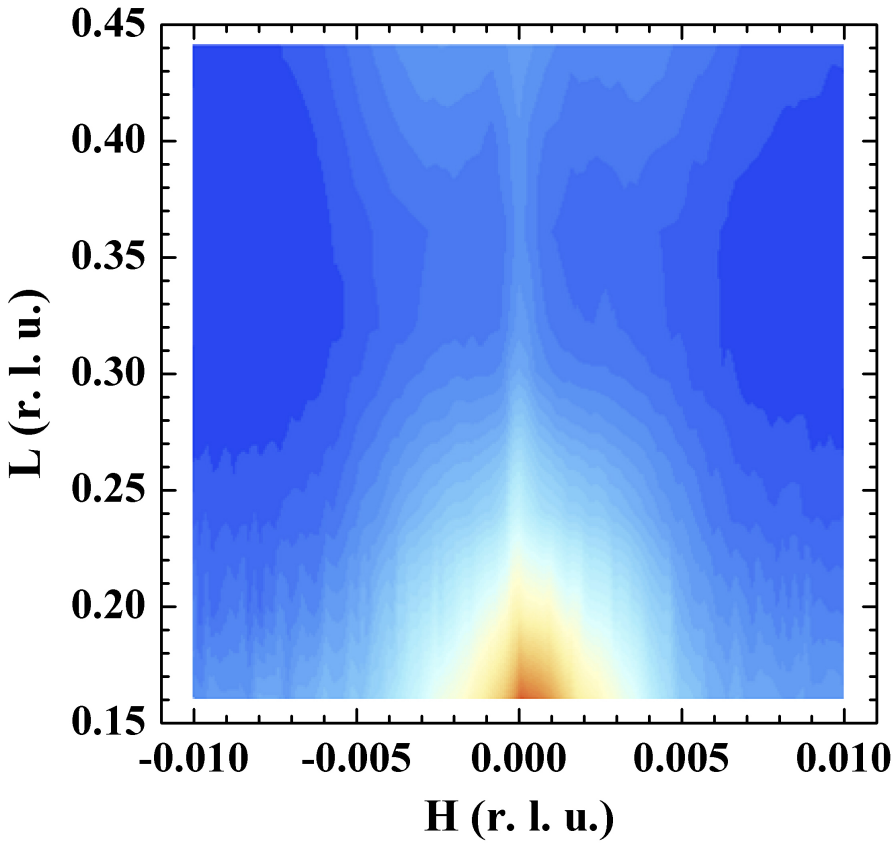

Figure 4.15: The side band scattering is tracked in the (H, 0, L) plane; E = 709.7 eV and the square root of the observed intensity is plotted. Blue shades denote low intensity regions and red shades denote high intensity regions.

peak significantly overlap and should not necessarily be treated as an indication that the modulation of the valence states has a momentum component at (0, 0, 0.44). The scattering along the H-direction near (0, 0, 0.1177) exhibits similar resonance behavior, as shown in Figure 4.13(a, b).

In order to study in detail the domain structure scattering energy dependence, the intensity at a transfer momentum associated with scattering from the domain array is examined while the beam energy is scanned—a fixed Q energy scan, in other words. Fixed Q energy scans at L = 0.15 and L = 0.44 are shown in Figure 4.16(a) and (b), respectively, with fixed in-plane momentum H = -0.003. The direction of the L = 0.44 fixed Q energy scan indicated in part (c), to give an impression of how this scan is related to the data in Figure 4.13. The scans exhibit e_g and t_{2g} like features, just as the Fe L edge XAS does. At L = 0.44, the e_g like peak appears at 709.6 eV and the t_{2g} like peak appears at 708.2 eV, as seen in Figure 4.16(b); the analogous features in the EY XAS at the Fe L_3 edge do not lie at the same energies, with the e_g = 708.66 eV in the XAS scan for example. The features of the L = 0.15 fixed Q energy scan in Figure 4.16(a) are also shifted away from those of the L = 0.44 scan. The relative

intensities of the e_g and t_{2g} like features differ markedly, with the e_g like peak much more intense than the t_{2g} like peak at L = 0.15; the difference between the intensities of the two peaks is much less drastic at L = 0.44. The resonant line shape is, thus, shown to evolve as a function of L. In other words, different momentum components of the domain structure scattering display different resonance behaviors.

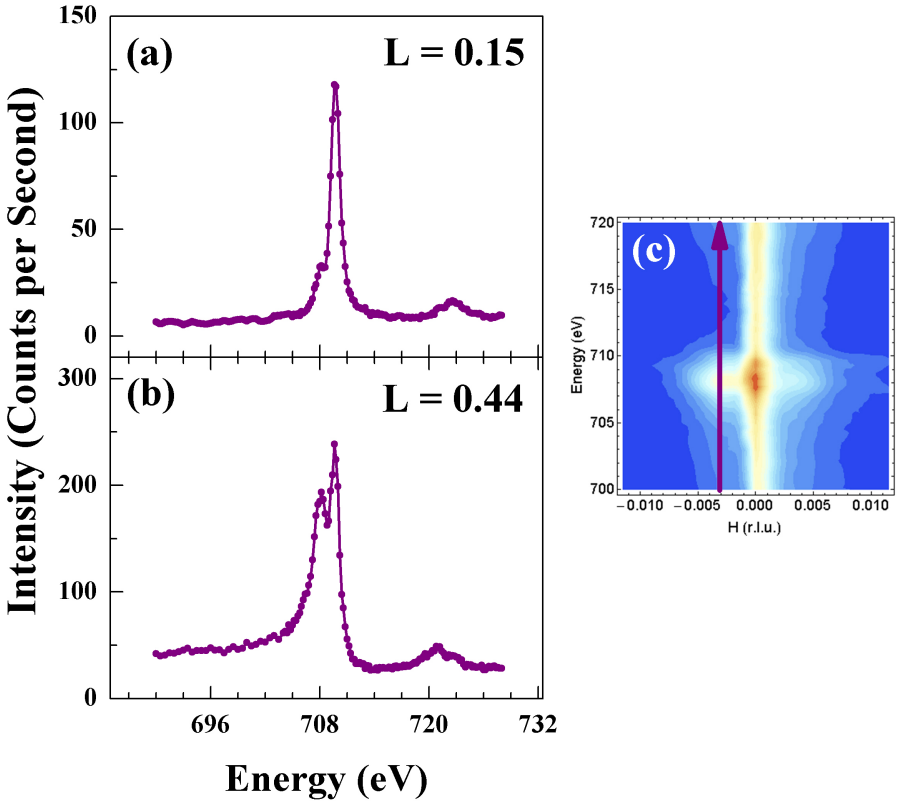

Figure 4.16: Fixed Q energy scans at (-0.003, 0, L) are plotted. Part (a) shows data obtained at L = 0.15; part (b) shows data obtained at L = 0.44. Part (c) indicates the direction of the fixed Q energy scan in a H/E mesh scan at L = 0.44.

The strong resonances seen near the Fe L_3 edge suggests that there is a magnetic contribution to the domain structure scattering. The background information presented earlier in this chapter supports this notion: the lattice symmetry forces the Dzyaloshinsky-Moriya coupling vector $\vec{D}$ and the polarization $\vec{P}$ to be collinear, in turn restricting the polarization and the weak ferromagnetic moment $\vec{M}$ to point in orthogonal directions. The polarizations must change direction from one domain to the next in these films in a manner consistent with a 109° rotation between the two domains and the $\vec{M}$ between two adjacent domains likely does something similar, leading to a magnetic modulation with a period equal to the ferroelectric domain period. To what degree the magnetism contributes to the scattering and how it interferes with the charge scattering

contribution at the level of the scattering amplitude remains a topic for future study.

We now address the issue of resonant scattering at the O K edge. The energy dependence of the domain structure scattering was examined near the O K edge. Figure 4.17 shows data obtained at a sample temperature of ≈ 250 K near (0, 0, 0.33), the highest practical L value for O K edge energies. Along the H-direction, domain structure scattering appears as side bands centered on H = $\pm$ 0.003, as shown in the top panel of the figure. The bottom panel of the figure illustrates how the scattering along the H-direction depends on the beam energy. Though there are increases in intensity of the side band as the energy is tuned through the fine structure near the O K edge, the energy dependence of the scattering is exactly that of the fluorescence yield data shown in Figure 4.11. Comparing the sideband scattering profile along the H-direction at 531 eV, near the t_{2g} peak, and at 517 eV, far below the transition edge, one finds that with a constant scaling factor the two scattering profiles can be made to overlap nearly exactly. This confirms that there is very little or no resonant scattering at these energies and that there is little O 2p character to the valence states participating in the domain array scattering.

Finally, it should be noted that the scattering is asymmetric about H = 0. This is particularly noticeable in the L = 0.44 H scans in Figure 4.13(c); H scans at L = 0.1177 are also asymmetric, as shown in in Figure 4.13(a), though it is not as pronounced as at higher L values. The asymmetry is independent of the sample, as rotating the sample 180° about its surface normal does not change the sense of the asymmetry in the H scans. It seems unlikely that it is due to self-absorption effects, as the H scans represent only a few degrees of change in Theta. That the asymmetry becomes more pronounced at higher L values (higher TwoTheta) suggests that this effect may be due to changes in the resolution function of the X1B/Spinoza diffractometer system.

Let us briefly discuss our preliminary results.

The strong resonant behavior of the domain structure scattering near the Fe L_3 transition edge demonstrates that there is a modulation of the valence band density of states due to the domain array. Further, the modulated valence states have a predominant Fe 3d character. This hints at a magnetic contribution to the scattering, as the electrons on the Fe sites are antiferromagnetically ordered and form a weak ferromagnetic moment due to the Dzyaloshinsky-Moriya effect.

How can it be quantitatively demonstrated that the resonant scattering observed near the Fe L_3 transition edge has a magnetic origin? The Methods chapter discussed the fact that magnetic x-ray scattering arises from the antisymmetric component of the scattering tensor. If a model susceptibility tensor with an antisymmetric component can account for the resonant line shape of the domain structure side bands, and a susceptibility tensor that is purely symmetric cannot do this, then a strong case can be made to support a claim of magnetic scattering from the domain structure.

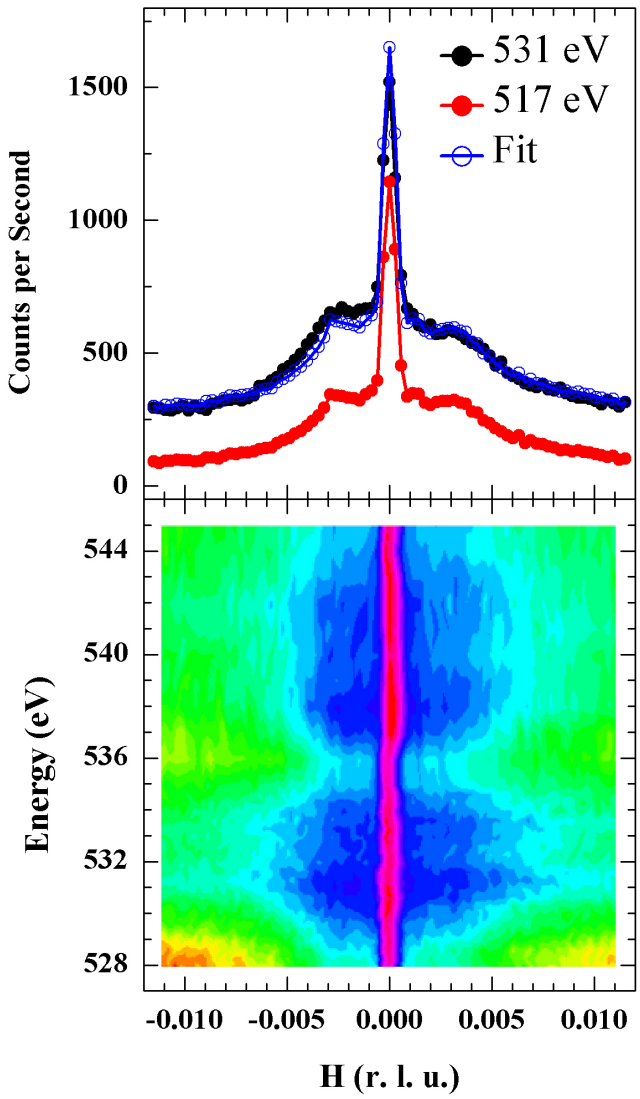

Figure 4.17: Domain structure scattering is observed near O K transition edge. In the bottom panel, the energy dependence of the side bands and specular are plotted against beam energy in the H versus beam energy mesh scan. The top panel compares H scans at two different energies, 531 eV (black) and 517 eV (red). By multiplying the 517 eV data by a constant and adding a constant background, the "Fit" curve is obtained; note that it overlaps very well with the 531 eV data.

In contrast to the Fe L_3 edge scattering, the O K edge scattering displays no resonance behavior. This observation can inform the general discussion regarding the origins of the anomalously high 109° and 180° domain wall electrical conductivity: there is speculation that oxygen deficiencies give rise to increased electrical conductivity at the 109° domain walls. [71] The oxygen deficiencies should give rise to hole doping of the oxygen 2p states. These deficiencies are supposed to occur in the vicinity of the domain walls, so resonant scattering near the O K edge should arise at a momentum characteristic of the domain

wall period. This is not observed in the data. This could be because there are too few holes in the O 2p states to notice in scattering. By carefully measuring the integrated intensity of the domain structure side bands seen at the O K edge as a function of beam energy, an upper bound on the average number of holes at the domain walls can be established.

4.4 Conclusions and Future Prospects

The preliminary results presented in this chapter demonstrate that simple charge density models can be used to adequately describe the structure of stripe-like domain arrays with a single type of domain wall. X-ray diffraction data obtained near the (0, 0, 1) Bragg peak of $BiFeO_3$ thin films exhibiting arrays of 109° and 71° domain walls have been reproduced using structure factors derived from these charge density models.

Resonant scattering near the Fe L_3 transition edge has revealed a modulation of valence states that are strongly Fe 3d in character that exhibits the same period as the ferroelectric domain structure. The possibility of a magnetic origin to the resonant scattering is being explored. A susceptibility tensor, possibly with an antisymmetric component, that can describe the resonant scattering line shape is being constructed. Additional scattering experiments to measure the polarization dependence of the resonant scattering from the domain structure are also planned. This will be done by rotating the sample about the momentum transfer of the resonant domain structure scattering, effectively rotating the linear polarization of the incident beam around this vector. The dependence of the scattering intensity as a function of the rotation angle about the domain structure scattering momentum transfer will be studied in order to determine if there is magnetic ordering associated with the domain structure.

It is hoped that this information, integrated into a real space model of the domain structure, can be used to gain insight into the electronic properties of the domain walls, particularly the origins of the giant electrical conductivity of the 109° domain wall compared to that of the 71° domain wall.

5 Conclusions

As this dissertation has demonstrated, a great deal about the novel physics of strongly correlated electron materials can be discovered using x-ray scattering techniques.

In the case of $KCuF_3$, a combined Raman and x-ray scattering survey of the lattice dynamics and structure revealed a previously unreported structural phase transition at T $\approx$ 50 K. This transition, and the critical orthorhombic lattice fluctuations at temperatures above this transition, proved critical to explaining many of the mysterious magnetic properties of $KCuF_3$. The critical orthorhombic fluctuations causes the orbital ordering to fluctuate between two nearly degenerate antiferro-orbital states over the same wide range of temperatures as the critical structural fluctuations. The orbital fluctuations, in turn, frustrate the electron spin ordering in the a-b plane. This provides a natural explanation for why the spin exchange in the a-b plane and the c-axis are so extremely anisotropic, and why the ratio of orbital ordering and spin ordering temperatures is $\sim$ 20 rather than less than 10. Below the structural transition temperature, the lattice exhibits glassy quasi-order characterized by domains of short range ordered $GdFeO_3$-like octahedral tilts. The near degeneracy of the orbital states is lifted by the distortions and the orbital fluctuations cease, favoring the orbital ordering solution that exhibits A-type antiferromagnetism, the known magnetic ground state.

In explaining the physics of $KCuF_3$, we have had to re-evaluate the basic assumptions of the orbital ordering approximation: because the effect of the ligand ions are swept into the effective orbital exchange parameters, the symmetry of the system is made artificially high. The effect of phonon modes that distort the apical F ions away from their high-symmetry positions, like the higher energy E_g Raman mode, do not get considered because they are incompatible with the high symmetry of the system. Critical physics was left out of the Kugel-Khomskii orbital ordering model as a result. The Raman and x-ray scattering observations revealed new physics, helping to inspire a new approach to orbital ordering that demonstrates that the effect of low symmetry phonons on orbital order can, at least in limited cases, be considered.

The x-ray scattering studies of epitaxial thin films of $BiFeO_3$ illustrate the capability of resonant soft x-ray scattering to determine the chemical character of the valence states that participate in the electronic ordered states of strongly correlated electron systems. Resonant scattering at the Fe L_3 transition edge

has been detected that arises from modulations of the Fe 3d valence states. The periods of the valence state modulations in our 109° domain wall samples is approximately the same as the ferroelectric domain periods measured in our samples with piezoresponse force microscopy, meaning that the resonant scattering is due to the domain structure. The strong Fe 3d character of the valence states probed by resonant scattering suggests that there is a magnetic ordered state associated with the ferroelectric domain structure. Future measurements will be made to ascertain whether this is the case and, if so, how the magnetic ordered moment evolves with the domain structure. The lack of any detectable resonant scattering near the O K transition edge strongly indicates that the O 2p states seem not to be sensitive to the ferroelectric domain structure, suggesting that they do not significantly influence its electronic properties.

Combined with the simple charge density models of the domain structure, developed by examining non-resonant hard x-ray diffraction data from our film samples, it may be possible to associate specific electronic properties with specific parts of the domain structure.

6 References

[1] Y. Tokura and N. Nagaosa, "Orbital Physics in Transition-Metal Oxides", Science **228**, 462-468 (2000)

[2] Sang-Wook Cheong and Maxim Mostovoy, "Multiferroics: a magnetic twist for ferroelectricity", Nature Materials **6**, 13-20 (2007)

[3] Charles Kittel, *Introduction to Solid State Physics, Seventh Edition* (Wiley, New York, 1996)

[4] Gabriel Kolitar and Dieter Vollhardt, "Strongly Correlated Materials: Insights From Dynamical Mean-Field Theory", Physics Today **57**, 53-59 (2004)

[5] K. I. Kugel and D. I. Khomskii, "Crystal structure and magnetic properties of substances with orbital degeneracy", Soviet Physics JETP **64**, 725 (1973); "The Jahn-Teller effect and magnetism: transition metal compounds", Soviet Physics Uspekhi **25**, 231 (1982)

[6] M. v. Zimmermann, C. S. Nelson, Y.-J. Kim, J. P. Hill, Doon Gibbs, H. Nakao, Y. Wakabayashi, Y. Murakami, Y. Tokura, Y. Tomioka, T. Arima, C.-C. Kao, D. Casa, C. Venkataraman, and Th. Gog, "Resonant x-ray-scattering study of octahedral tilt ordering in $LaMnO_3$ and $Pr_{1-x}Ca_xMnO_3$", Physical Review B **64**, 064411

[7] P. M. Woodward, "Octahedral Tilting in Perovskites. II. Structure Stabilizing Forces", Acta Crystallographica **B53**, 44-66 (1997)

[8] R. D. Shannon, "Revised effective ionic radii and systematic studies of interatomic distances in halides and chalcogenides", *Acta Crystallographica* **A32**, 751-767 (1976)

[9] Rob Janes and Elaine Moore, *Metal-Ligand Bonding* (Royal Society of Chemistry, Cambridge, UK, 2004)

[10] John B. Goodenough, *Magnetism and the Chemical Bond*, (Interscience (Wiley), New York, 1963)

[11] P. W. Anderson, in *Magnetism* **1**, edited by G. T. Rado and H. Suhl (Academic Press, New York, 1963)

[12] I. E. Dzyaloshinsky, *J. Phys. Chem. Solids* **4**, 241-255 (1958); T. Moriya, *Phys. Rev.* **120**, 91-98 (1960)

[13] D. Attwood, *Soft X-rays and Extreme Ultraviolet Radiation: Principles and Applications* (Cambridge University Press, 1999)

[14] Joachim Stöhr, *NEXAFS Spectroscopy (Springer Series in Surface Sciences, Vol. 25)*, (Springer-Verlag, Heidelberg, 1992)

[15] J.D. Jackson, *Classical Electrodynamics, Third Edition* (Wiley, 1999)

[16] D.J. Griffiths, *Introduction to Electrodynamics, Third Edition* (Addison Wesley, 1999)

[17] P. S. Pershan, "Magneto-Optical Effects", Journal of Applied Physics **38**, 1483 (1967)

[18] William H. Zachariasen, *Theory of X-ray Diffraction in Crystals* (Dover Publications, New York, 1967)

[19] Frank de Groot and Akio Kotani, *Core Level Spectroscopy of Solids* (CRC Press, 2008)

[20] Jens Als-Nielsen and Des McMorrow, *Elements of modern X-ray physics* (Wiley, 2001)

[21] M. Blume, in *Resonant Anomalous X-ray Scattering: Theory and Applications*, edited by G. Materlik, C. J. Sparks, and K. Fischer (Elsevier, Amsterdam, 1994)

[22] J.J. Sakurai, *Advanced Quantum Mechanics* (Addison-Wesley, Redwood City, 1984)

[23] W. R. Busing and H. A. Levy, "Angle calculations for 3- and 4-circle X-ray and neutron diffractometers", Acta Crystallographica **22**, 457-464 (1967)

[24] C. T. Chen, "Concept and Design Procedure for Cylindrical Element Monochromators for Synchrotron Radiation", Nuclear Instruments and Methods in Physics Research **A256**, 595-604 (1987); C. T. Chen and F. Sette, "Performance of the Dragon soft x-ray beamline", Review of Scientific Instruments **60**, 1616-1621 (1989)

[25] K.J. Randall, W. Eberhardt, J. Feldhaus, W. Erlebach, A.M. Bradshaw, Z. Xu, P.D. Johnson, and Y. Ma,"NSLS X1B - an undulator beamline for high resolution soft X-ray spectroscopy", Nuclear Instruments and Methods in Physics Research **A319**, 101-105 (1992)

[26] B.L. Henke, E.M. Gullikson, and J.C. Davis, "X-ray interactions: photoabsorption, scattering, transmission, and reflection at E=50-30000 eV, Z=1-92", Atomic Data and Nuclear Data Tables **54**, 181-342 (1993)

[27] S. Eisebitt, T. Boske, J.-E. Rubensson, and W. Eberhardt, "Determination of absorption coefficients for concentrated samples by fluorescence detection", Physical Review B **47**, 14103-14109 (1993)

[28] H. Jahn and E. Teller, in *Proceedings of the Royal Society of London A* **161**, 220-235 (1937)

[29] V. Polinger in *The Jahn-Teller Effect: Fundamentals and Implications for Physics and Chemistry, Springer Series in Chemical Physics Vol. 97*, edited by Horst Köppel, David R. Yarkony and Heinz Barentzen (Springer, Berlin, 2009)

[30] J. Kanamori, "Crystal Distortion in Magnetic Compounds", Journal of Applied Physics **31**, S14 (1960)

[31] Atsushi Okazaki and Yasutaka Suemune, "The Crystal Structures of $KCuF_3$, $KCuF_3$, $KCuF_3$, $KCuF_3$ and $KCuF_3$ above and below their Néel Temperatures", *J. Phys. Soc. Jpn.* **16**, 672 (1961)

[32] M. T. Hutchings, E. J. Samuelsen, G. Shirane and K. Hirakawa, "Neutron-Diffraction Determination of the Antiferromagnetic Structure of $KCuF_3$", *Phys. Rev.***188**, 919 (1969)

[33] S. K. Sajita, J. D. Axe, G. Shirane, H. Yoshizawa, K. Hirakawa, "Neutron scattering study of spin waves in one-dimensional antiferromagnet $KCuF_3$", *Phys. Rev.***21**, 2001 (1980)

[34] Masanori Hidaka, Takashi Eguchi and Isao Yamada, "New Superlattice Crystal Structure in $KCuF_3$ Reveald by X-Ray Diffraction Experiments", *J. Phys. Soc. Jpn.* **67**, 2488-2494 (1998)

[35] E. Pavarini, E. Koch, and A. I. Lichtenstein, "Mechanism for Orbital Ordering in $KCuF_3$", *Phys. Rev. Lett.* **101**, 266405 (2008)

[36] L. Paolasini, R. Caciuffo, A. Sollier, P. Ghigna, and M. Altarelli, "Coupling between Spin and Orbital Degrees of Freedom in $KCuF_3$", *Phys. Rev. Lett. 88*, 106403 (2002)

[37] I. Yamada, H. Fujii and M. Hidaka, "Experimental evidence of the Dzyaloshinsky-Moriya antisymmetric exchange interaction in the onedimensional Heisenberg antiferromagnet $KCuF_3$: EPR measurements", *J. Phys.: Condens. Matter* **1**, 3397-3408 (1989)

[38] M.V. Eremin, D.V. Zakharov, H.-A. Krug von Nidda, R. M. Eremina, A. Shuvaev, A. Pimenov, P. Ghigna, J. Deisenhofer, and A. Loidl, "Dynamical Dzyaloshinsky-Moriya Interaction in $KCuF_3$", *Phys. Rev. Lett.* **101**, 147601 (2008)

[39] James C. T. Lee, Shi Yuan, Siddhartha Lal, Young Il Joe, Yu Gan, Serban Smadici, Ken Finkelstein, Yejun Feng, Andrivo Rusydi, Paul M. Goldbart, S. Lance Cooper and Peter Abbamonte, "Two-stage orbital order and dynamical spin frustration in $KCuF_3$", *Nature Physics* **8**, 63-66 (2012)

[40] K. Hirakawa and Y. Kurogi, "One-dimensional antiferromagnetic properties of $KCuF_3$", *Suppl. Prog. Theor. Phys.* **46**, 147-161 (1970)

[41] C. Lin and A. J. Millis, "Theoretical description of pseudocubic manganites", *Phys. Rev.* **B 78**, 174419 (2008)

[42] P. Abbamonte, A. Rusydi, S. Smadici, G. D. Gu, G. A. Sawatzky and D. L. Feng, "Spatially modulated 'Mottness' in $La_{2-x}Ba_xCuO_4$", *Nature Physics* **1**, 155-158 (2005)

[43] D. Alan Tennant, Stephen E. Nagler, Detmar Welz, Gen Shirane and Kazuyoshi Yamada, "Effects of coupling between chains on the magnetic excitation spectrum of $KCuF_3$", *Phys. Rev.* **B 52**, 13381 (1995)

[44] Louis Felix Feiner, Andrzej M. Oleś and Jan Zaanen, "Quantum Melting of Magnetic Order due to Orbital Fluctuations", *Phys. Rev. Lett.* **78**, 2799 (1997)

[45] M.V. Mostovoy and D. I. Khomskii, "Orbital Ordering in Charge Transfer Insulators", *Phys. Rev. Lett.* **92**, 167201 (2004)

[46] P. Phillips, *Advanced Solid State Physics*, (Westview Press, Boulder, CO, 2003)

[47] J. Mannhart and D. G. Schlom, "Oxide Interfaces—An Opportunity for Electronics", Science **327**, 1607-1611 (2010)

[48] A. Ohtomo, D. A. Muller, J. L. Grazul, H. Y. Hwang, "Artificial charge-modulation in atomic-scale perovskite titanate superlattices", Nature **419**, 378 (2002)

[49] S. Okamoto, A. J. Millis, "Electronic reconstruction at an interface between a Mott insulator and a band insulator", Nature **428**, 630 (2004)

[50] , R. Ramesh and Nicola A. Spaldin, "Multiferroics: progress and prospects in thin films", Nature Materials **6**, 21-29 (2007)

[51] Gustau Catalan and James F. Scott, "Physics and Applications of Bismuth Ferrite", Advanced Functional Materials **21**, 2463-2485 (2009)

[52] J. Wang, J. B. Neaton, H. Zheng, V. Nagarajan, S. B. Ogale, B. Liu, D. Viehland, V. Vaithyanathan, D. G. Schlom, U. V. Waghmare, N. A. Spaldin, K. M. Rabe, M. Wuttig, and R. Ramesh, "Epitaxial BiFeO3 Multiferroic Thin Film Heterostructures", Science **299**, 1719 (2003)

[53] J. Seidel, L. W. Martin, Q. He, Q. Zhan, Y.-H. Chu, A. Rother, M. E. Hawkridge, P. Maksymovych, P. Yu, M. Gajek, N. Balke, S. V. Kalinin, S. Gemming, F. Wang, G. Catalan, J. F. Scott, N. A. Spaldin, J. Orenstein and R. Ramesh, "Conduction at domain walls in oxide multiferroics", *Nature Materials* **8**, 229 - 234 (2009)

[54] J. B. Neaton, C. Ederer, U. V. Waghmare, N. A. Spaldin, and K. M. Rabe, "First-principles study of spontaneous polarization in multiferroic $BiFeO_3$", Physical Review B **71**, 014113 (2005)

[55] Donna C. Arnold, Kevin S. Knight, Finlay D. Morrison, and Philip Lightfoot, "Ferroelectric-Paraelectric Transition in $BiFeO_3$: Crystal Structure of the Orthorhombic β Phase", Physical Review Letters **102**, 027602 (2009); Donna C. Arnold, Kevin S. Knight, Gustau Catalan, Simon A. T. Redfern, James F. Scott, Philip Lightfoot, and Finlay D. Morrison, "The β-to-γ Transition in $BiFeO_3$: A Powder Neutron Diffraction Study", Advanced Functional Materials **20**, 21162123 (2010)

[56] Claude Ederer and Nicola A. Spaldin, "Influence of strain and oxygen vacancies on the magnetoelectric properties of multiferroic bismuth ferrite", Physical Review B **71**, 224103 (2005).

[57] S. K. Streiffer, C. B. Parker, A. E. Romanov, M. J. Lefevre, L. Zhao, J. S. Speck, W. Pompe, C. M. Foster and G. R. Bai, "Domain patterns in epitaxial rhombohedral ferroelectric films. I. Geometry and experiments", Journal of Applied Physics **83**, 2742-2753 (1998)

[58] Ying-Hao Chu, Qing He, Chan-Ho Yang, Pu Yu, Lane W. Martin, Padraic Shafer, and R. Ramesh, "Nanoscale Control of Domain Architectures in $BiFeO_3$ Thin Films", Nano Letters **9**, 1726-1730 (2009).

[59] Lane W. Martin, Ying-Hao Chu, Mikel B. Holcomb, Mark Huijben, Pu Yu, Shu-Jen Han, Donkoun Lee, Shan X. Wang, and R. Ramesh, "Nanoscale Control of Exchange Bias with $BiFeO_3$ Thin Films", Nano Letters **8**, 2050-2055 (2008)

[60] Elisabeth Soergel, "Piezoresponse force microscopy (PFM)", Journal of Physics D: Applied Physics **44**, 464003 (2011)

[61] C. M. Folkman, S. H. Baek, H. W. Jang, C. B. Eom, C. T. Nelson, X. Q. Pan, Y. L. Li, L. Q. Chen, A. Kumar, V. Gopalan, and S. K. Streiffer, "Stripe domain structure in epitaxial (001) $BiFeO_3$ thin films on orthorhombic $TbScO_3$ substrate", Applied Physics Letters **94**, 251911 (2009); Chad M. Folkman, Seung-Hyub Baek and Chang-Beom Eom, "Twin wall distortions through structural investigation of epitaxial $BiFeO_3$ thin films", Journal of Materials Research **26**, 2844-2853 (2011)

[62] S. O. Hruszkewycz, C. M. Folkman, M. J. Highland, M. V. Holt, S. H. Baek, S. K. Streiffer, P. Baldo, C. B. Eom, and P. H. Fuoss, "X-ray nanodiffraction of tilted domains in a poled epitaxial $BiFeO_3$ thin film", Applied Physics Letters **99**, 232903 (2011)

[63] C. J. M. Daumont, S. Farokhipoor, A. Ferri, J. C. Wojdeł, Jorge Íñiguez, B. J. Kooi, and B. Noheda, "Tuning the atomic and domain structure of epitaxial films of multiferroic $BiFeO_3$", Physical Review B **81**, 144115 (2010)

[64] G. Rispens, Ph.D. Thesis, University of Groningen, 2010

[65] A. E. Romanov, M. J. Lefevre, J. S. Speck, W. Pompe, S. K. Streiffer, and C. M. Foster, "Domain pattern formation in epitaxial rhombohedral ferroelectric films. II. Interfacial defects and energetics", Journal of Applied Physics **83**, 2754-2765 (1998)

[66] W. T. Lee, E. K. H. Salje, and U. Bismayer, "Domain-wall structure and domain-wall strain", Journal of Applied Physics **93**, 9890-9897 (2003)

[67] H. A. Dürr, E. Dudzik, S. S. Dhesi, J. B. Goedkoop, G. van der Laan1, M. Belakhovsky, C. Mocuta, A. Marty, Y. Samson, "Chiral Magnetic Domain Structures in Ultrathin FePd Films", Science **284**, 2166-2168 (1999)

[68] G. van der Laan, E. Dudzik, S.P. Collins, S.S. Dhesi, H.A. Dürr, M. Belakhovsky, K. Chesnel, A. Marty, Y. Samson, B. Gilles, "Soft X-ray magnetic scattering from striped magnetic domain structures", Physica B **283**, 171-174 (2000)

[69] F. M. F. de Groot, M. Grioni, J. C. Fuggle, J. Ghijsen, G. A. Sawatzky, and H. Petersen, "Oxygen 1s x-ray-absorption edges of transition-metal oxides", Physical Review B **40**, 5715-5723 (1989)

[70] M. Abbate, F. M. F. de Groot, J. C. Fuggle, A. Fujimori, O. Strebel, F. Lopez, M. Domke, G. Kaindl, G. A. Sawatzky, M. Takano, Y. Takeda, H. Eisaki, and S. Uchida, "Controlled-valence properties of $La_{1-x}Sr_xFeO_3$ and $La_{1-x}Sr_xMnO_3$ studied by soft-x-ray absorption spectroscopy", Physical Review B **46**, 4511-4519 (1992)

[71] J. Seidel, P. Maksymovych, Y. Batra, A. Katan, S.-Y. Yang, Q. He, A. P. Baddorf, S.V. Kalinin, C.-H. Yang, J.-C. Yang, Y.-H. Chu, E. K. H. Salje, H. Wormeester, M. Salmeron, and R. Ramesh, "Domain Wall Conductivity in La-Doped $BiFeO_3$", Physical Review Letters **105**, 197603 (2010)